MODELING AND SIMULATION OF MICROFLUIDIC CHIPS FOR ANALYTICAL APPLICATIONS

by

Pablo Alejandro Kler

Dissertation submitted to the Postgraduate Department of the

FACULTAD DE INGENIERÍA Y CIENCIAS HÍDRICAS

of the

UNIVERSIDAD NACIONAL DEL LITORAL

in partial fulfillment of the requirements for the degree of

Doctor en Ingeniería - Mención Mecánica Computacional

2010

Author Legal Declaration

This dissertation have been submitted to the Postgraduate Department of the *Facultad de Ingeniería y Ciencias Hídricas* in partial fulfillment of the requirements the degree of *Doctor en Ingeniería - Mención Mecánica Computacional* of the *Universidad Nacional del Litoral*. A copy of this document will be available at the University Library and it will be subjected to the Library's legal normative.

Some parts of the work presented in this thesis have been (or are going to be) published in the following journals: *Computer Methods in Applied Mechanics and Engineering, Microfluidics and Nanofluidics, Advances in Water Resources, and the 14 μ-TAS Conference Proceedings.*

Pablo Alejandro Kler

MODELING AND SIMULATION OF MICROFLUIDIC CHIPS FOR ANALYTICAL APPLICATIONS

Thesis advisors:

Fabio A. Guarnieri	INTEC (CONICET-UNL)
	Facultad de Ingeniería - UNER
Claudio L.A. Berli	INTEC (CONICET-UNL)
	Facultad de Ingeniería y Ciencias Hídricas - UNL

Evaluation committee members:

Alejandro Allevi	Instituto Tecnológico Buenos Aires
Jorge D'Elía	INTEC (CONICET-UNL)
	Facultad de Ingeniería y Ciencias Hídricas - UNL
Silvia R. Hernández	Facultad de Bioquímica y Ciencias Biológicas - UNL
Hernan Pastoriza	CAB (CNEA - CONICET)
	Instituto Balseiro (CNEA - UNCUYO)
Salvador Ortiz	CAC - CNEA
	Facultad de Ciencias Exactas y Naturales - UBA

FACULTAD DE INGENIERÍA Y CIENCIAS HÍDRICAS

UNIVERSIDAD NACIONAL DEL LITORAL

2010

Acknowledgements

This thesis has received financial support from *Consejo Nacional de Investigaciones Científicas y Técnicas* (CONICET), *Universidad Nacional del Litoral* (UNL), and *Agencia Nacional de Promoción Científica y Tecnológica* (ANPCyT). The research work was carried out at the *Centro Internacional de Métodos Computacionales en Ingeniería* (CIMEC) of the *Instituto de Desarrollo Tecnológico para la Industria Química* (INTEC), dependent of UNL and CONICET.

I would like to thank my advisors Fabio A. Guarnieri and Claudio L. A. Berli for their trust, support and guidance. Special gratitude also goes to Lisandro D. Dalcín, Rodrigo R. Paz and Mario A. Storti for their patience and clarity in sharing with me their knowledge and experience on HPC. I also would like to thank Jorge D'Elía to keep Aquiles *awake and alive*, and to all the beautiful people at CIMEC that make from every working day a meaningful anecdote.

Abstract

Lab-on-a-Chips (LOC) are microdevices that integrate one or several laboratory functions on a single chip of a few square centimeters. LOC provide a platform to conduct chemical and biochemical analysis in a wide variety of scientific areas.

Numerical simulations of LOC are extremely useful at design and optimization stages. They can provide a more complete understanding of the fundamental physical and chemical process that occur in LOC. Also, numerical simulations are useful for the optimization of parameters for geometry and operation, minimizing the risk of wasting time and money in a flawed design.

The main contribution of this thesis is the development and testing of a set of numerical tools that are aimed to improve the design and develop of LOC. The several physicochemical fields involved and the special considerations required due to the high aspect ratios between length scales involved, determine the complexity of modelling and the computational cost. Along this thesis different numerical modelling approaches are presented in order to show different options to deal with these problems.

Several examples of numerical simulation for analytical processes in LOC are presented. Some of them are devoted to validate the mathematical model and the simulation tools developed. Other examples consist in simulations of different experimental analytical process performed in LOC that are aimed to illustrate the proficiency of the numerical model to simulate a wide variety of LOC analytical applications.

Contents

List of Abbreviations

Ab: Antibody.
AC: Alternate current.
ADP: Adenosine diphosphate.
Ag: Antigen.
AgAb: Antigen-antibody complex.
AMG: Algebraic multigrid.
AMR: Adaptive mesh refinement.
ASM: Additive Schwartz method.
ATP: Adenosine triphosphate.
BSA: Bovine serum albumin.
CACO: Cacodylic acid.
CE: Capillary electrophoresis.
CEC: Capillary electrochromathography.
CIMEC: International Center for Numerical Methods in Engineering.
CFD: Computational fluid dynamics.
CRP: C-reactive protein.
CZE: Capillary zone electrophoresis.
E: Enzyme.
EDL: Electric double layer.
ELISA: Enzyme linked immunosorbent assay.
EOF: Electroosmotic flow.
ES: Enzyme-substrate complex.
FCT: Flux corrected transport.
FD: Finite differences.
FEM: Finite element method.

FFE: Free flow electrophoresis.
FFIEF: Free flow isoelectric focusing.
FVM: Finite volume method.
GFP: Green fluorescent protein.
GMRES: Generalized minimal residual method.
G6P: Glucose 6-Phosphate.
G6PDH: Glucose 6-Phosphate dehydrogenase.
HK: Hexokinase.
HPC: High performance computing.
ICEF: Induced charge electroosmotic flow.
IEF: Isoelectric focusing.
IPG: Immobilized pH gradient.
ITP: Isotachophoresis.
LC: Liquid chromatography.
LE: Leading electrolyte.
LOC: Lab-on-a-Chip / s.
MBE: Moving boundary electrophoresis.
MPI: Message passing interface.
NADH: Reduced nicotinamide adenine dinucleotide.
NAD^+ : Nicotinamide adenine dinucleotide.
P: Enzymatic reaction product.
PDE: Partial differential equation.
PDMS: Polydimethyl siloxane.
PEG: Polyethylene glycol.
PET: Polyethylene terephtalate.
PETSc: Portable extensible toolkit for scientific computation.
PG: Protein G.
PMMA: Polymethyl methacrylate.
PR: Photoresist.
PSPG: Pressure stabilized Petrov - Galerkin.
PVC: Polyvinyl chloride.
PVD: Physical vapor deposition.
pH: *"Power of Hydrogen"*.

pI: Isoelectric point.
S: Enzymatic reaction substrate.
SC: Shock capturing.
SNES: Scalable nonlinear equations solvers.
SPD: Symmetric and positive definite.
SPICE: Simulation program with integrated circuits emphasis.
SPRESSO: Stanford's public release electrophoretic separation solver.
SUPG: Streamline upwind Petrov - Galerkin.
TE: Terminating electrolyte.
TRIS: Tris(hydroxymethyl)-aminoetane.
UV: Ultraviolet.
μ-TAS: Miniaturized total chemical analysis system.

List of Symbols

a_p: Molecule main dimension.
C^0: Functional space for continuous real functions.
c^0: Standard molarity of 1 mol l^{-1}.
c_{ATP}: Molar adenosine triphosphate concentration.
c_G: Molar glucose concentration.
c_{G6P}: Molar glucose 6-Phosphate concentration.
c_{G6PDH}: Molar glucose 6-Phosphate dehydrogenase concentration.
c_{HK}: Molar hexokinase concentration.
c_j: Molar concentration of ion j.
c_j^h: Discrete molar concentration of ion j.
c_j^∞: Bulk molar concentration of ion j.
c_{NAD^+}: Molar nicotinamide adenine dinucleotide concentration.
c_{NADH}: Molar reduced nicotinamide adenine dinucleotide concentration.
c^∞: Bulk molar concentration.
$c^h_{\mathrm{ref_j}}$: Reference concentration for the shock capturing coefficient for the specie j.
D_j: Diffusion coefficient of specie j.
$\mathbf{E}$: Electric field.
F: Faraday constant.
$\mathbf{g}$: Gravitational field acceleration.
H^1: Hilbert functional space of order 1.
$h_{\mathrm{shock_j}}$: Equivalent mesh parameter for the shock capturing coefficient for the specie j.
$h_{\mathrm{supg_j}}$: Equivalent mesh parameter for the streamline upwind Petrov - Galerkin coefficient for the specie j.

I_s: Ionic strength.
i: Electric current density.
$J_{i,n}^{\alpha,\beta}$: Jacobian function for the states i and n, at the Gauss points α and β.
K: Element of the topological discretization.
K_a: Acidic dissociation constant.
K_b: Basic dissociation constant.
K_{ilm}: General reaction coefficient of specie i for second order coupled reaction with specie l and m.
K_m: Michaelis constant.
K_s: Surface dissociation constant.
K_w: Water dissociation constant.
k_1: Forward rate constant for the formation of the enzyme-substrate complex.
k_{-1}: Backward rate constants for the formation of the enzyme-substrate complex.
k_{a1}: Acidic dissociation rate.
k_{a2}: Acidic association rate.
k_B: Boltzmann constant.
k_{b1}: Basic dissociation rate.
k_{b2}: Basic association rate.
k_{bn}: Rate constants for antigen-antibody binding.
k_{ij}: General reaction coefficient of specie i for first order coupled reaction with specie j.
k_p: Kinetic constant for conversion of enzyme-substrate complex complex to product.
k_u: Rate constants for antigen-antibody unbinding.
N: total amount of ions present in the electrolyte solution.
nel: Total number of elements of the discretization.
n_s: Number of specific sites of a surface to release or take H^+.
$\mathrm{Pe_j}$: Pèclet number for the specie j.
p: Fluid pressure.
p^1: First order real polynomial functions set.
pK_a: Equilibrium point for the acidic dissociation reaction.
pK_b: Equilibrium point for the basic association reaction.

R: Universal gas constant.
R_i^α: Residual for the specie i at the Gauss point α.
r_{A^-}: reaction term in acid state for generic amphoteric compound mass transport equation.
r_{Ab}: reaction term in antibody mass transport equation.
r_{Ag}: reaction term in antigen mass transport equation.
r_{AgAb}: reaction term in antigen-antibody complex mass transport equation.
r_{AH}: reaction term in neutral state for generic amphoteric compound mass transport equation.
$r_{AH_2^+}$: reaction term in basic state for generic amphoteric compound mass transport equation.
r_{ATP}: reaction term in adenosine triphosphate mass transport equation.
r_G: reaction term in glucose mass transport equation.
r_{G6P}: reaction term in glucose 6-Phosphate mass transport equation.
r_{G6PDH}: reaction term in glucose 6-Phosphate dehydrogenase mass transport equation.
r_{H^+}: reaction term in hydrogen mass transport equation.
r_{HK}: reaction term in hexokinase mass transport equation.
r_j: Reaction term for mass transport equation of specie j.
r_{NAD^+}: reaction term in nicotinamide adenine dinucleotide mass transport equation.
r_{NADH}: reaction term in reduced nicotinamide adenine dinucleotide mass transport equation.
r_P: Enzymatic reaction term for mass transport equation of product.
r_S: Enzymatic reaction term for mass transport equation of substrate.
T: Absolute temperature.
T^h: Topological discretization.
$\mathbf{u}$: Fluid velocity.
$\mathbf{u}^h$: Discrete fluid velocity.
u_j^h: Generic discrete state for the specie j projected at a Gauss point.
$\mathbf{v_{eo}}$: Electroosmotic velocity.
$\mathbf{v_{ep}}$: Electrophoretic velocity.
V_h: Finite element method weight and test functions subspace.

v: Continuous weight function for the finite element method.
v^h: Weight function for the finite element method.
v_h^α: Shape function for the finite element method evaluated at a Gauss point α.
z: Ionic valence..
z_j: Ionic valence of ion j.
α: Generic Gauss point.
α_0: Degree of dissociation for the acid state.
α_2: Degree of dissociation for the basic state.
γ_a: Activity coefficient.
δ_{kn}: Kronecker delta for subscripts k and n.
$\delta_{\text{shock}_\text{j}}$: Shock capturing coefficient for the specie j.
ϵ: Electric permittivity.
ϵ_r: Relative electric permittivity.
ϵ_0: Vacuum electric permittivity.
ζ: Electrokinetic potential.
ζ_m: Molecule electrokinetic potential.
ζ_w: Wall electrokinetic potential.
η: Normal coordinate to the solid boundary.
θ: Crank - Nicholsohn temporal integration parameter.
λ_D: Debye length.
μ: Dynamic viscosity.
$\tilde{\tilde{\mu}}_j$: Electrochemical potential for the ion j.
$\tilde{\mu}_j$: Chemical potential for the ion j.
$\tilde{\mu}_j^0$: Standard chemical potential for the ion j.
ρ: Fluid density.
ρ_e: Volume charge density.
σ: Electrical conductivity of the electrolyte solution.
τ :Tangential coordinate to the solid boundary.
τ_{s1}: Temporal term of streamline upwind Petrov - Galerkin coefficient.
$\tau_{\text{s2}_\text{j}}$: Advective term of streamline upwind Petrov - Galerkin coefficient for the specie j.
$\tau_{\text{s3}_\text{j}}$: Diffusive term of streamline upwind Petrov - Galerkin coefficient for the specie j.

τ_{s4_j}: Compressible term of streamline upwind Petrov - Galerkin coefficient for the specie j.
ϕ: Externally applied electric potential.
ψ: Electric potential due to the surface charge.
ψ_d: Electric potential at the outer Helmholtz plane.
ψ_0: Electric potential at the inner Helmholtz plane.
Γ: Finite element method domain boundary.
Γ_D: Finite element method domain boundary for Dirichlet conditions.
Γ_N: Finite element method domain boundary for Neumann conditions.
Γ_R: Finite element method domain boundary for Robin conditions.
Φ: Total electric potential.
Ω: Electrophoretic mobility.
Ω_j: Electrophoretic mobility of ion j.
Ω^h: Finite element method domain.
[ ]: Concentration in mol m^{-3}

List of Figures

List of Tables

Preface

In the last decade there has been a growing interest in the the so-called Lab-on-a-Chip (LOC) devices. LOC are microdevices that integrate one or several laboratory functions on a single chip of a few square centimeters. LOC provide a platform to conduct chemical and biochemical analysis in a variety of scientific areas, such as genetics, molecular biology, pharmacology and environment monitoring, among others. There are several advantages in the use of LOC in comparison with the classical bench-top equipment: faster analysis time, smaller reagent consumption, and less waste generation. Moreover, it adds the capability of integration with microelectronic, portability, and automation.

The fabrication of LOC is still very complex and often expensive in time and money. Design of LOC has to be done in a clever way in order to obtain efficient prototypes. Numerical simulations of LOC are therefore extremely useful. They can provide not only a more complete understanding of the fundamental physical and chemical process of the entire device, but also optimal parameters for geometry and operation, thus minimizing the risk of wasting time and money in a flawed design.

This thesis reports the development of a useful computational tool to numerical prototype LOC. The path to achieve a reliable software toolkit is described along this manuscript. The first chapter collect different aspects on the past and the present of LOC manufacturing and applications. The second chapter resumes different simulations related to the field of microfluidics, electrophoresis, and other analytical techniques in LOC. Following, third chapter describes the mathematical modelling required to obtain a complete set of equations that describes entire LOC prototypes. Also the implementation of these equations by using the finite element method is described in chapter 4.

Finally, chapter 5 shows several examples of simulation of analytical processes carried out in LOC. The first group of these examples are aimed to provide numerical and experimental validation. Then, complex numerical prototypes for different analytical techniques are explored.

The hope is that LOC become an important part of the efforts to improve global health, particularly through the development of point-of-care diagnostic devices. In situations with few health care resources, infectious diseases, renal or blood pathologies, breast or prostate cancer, among others, that would be treatable in a developed context are often deadly. Early detection of this disorders is crucial to avoid fatal consequences (Yager et al., 2006).

Chapter 1

Introduction

This chapter is an introduction to the general aspects of miniaturized analytical systems, or Lab-on-a-chip (LOC). LOC technology starts due to the main support of microelectronics industry that provides the early fabrication methods. Then, the evolution of LOC involved new materials and manufacturing techniques, and this evolution contributed to develop new analytical techniques covering a wide range of applications. Along this chapter this evolution is discussed: section 1.1 presents a brief description about the origins of LOC, and section 1.2 offers a brief technical background on most used microfabrication techniques for LOC. Finally, section 1.3 summarizes the main analytical techniques implemented in LOC platforms.

1.1 Origins of the Lab-on-a-Chip Technology

The first miniaturized analytical device was a gas chromatograph with thermal conductivity detection manufactured in silicon by Terry et al. (1979) (see Fig. 1.1). This device not only was able to separate a mixture of compounds in a few seconds, but founded a new paradigm in analysis systems: miniaturized analytical systems based on microfabrication techniques. Despite its high performance, the response of the scientific community was virtually none. Only few examples following this new paradigm were published until 1990, when a miniaturized open-tubular liquid chromatograph in a silicon wafer was

presented (Manz et al., 1990b). Simultaneously, the concept of *"miniaturized total chemical analysis system"* or μ-TAS was proposed by Manz et al. (1990a), where sample pretreatment and detection stages were included in the same device.

Initially, the main reason for miniaturization was therefore enhancing the analytical performance of the device rather than reducing its size. However, it was also recognized that small sizes present some extra advantages like smaller consumption of reagents, carrier, and mobile phase, and the integration of the several stages involved in the whole analysis process. The concept of *"Lab-on-a-chip"* was coined later indicating the downscaling of single or multiple lab processes to chip-format (Duffy et al., 1998). Then μ-TAS becomes a broader term dedicated to the integration of the total sequence of laboratory processes to perform chemical analysis.

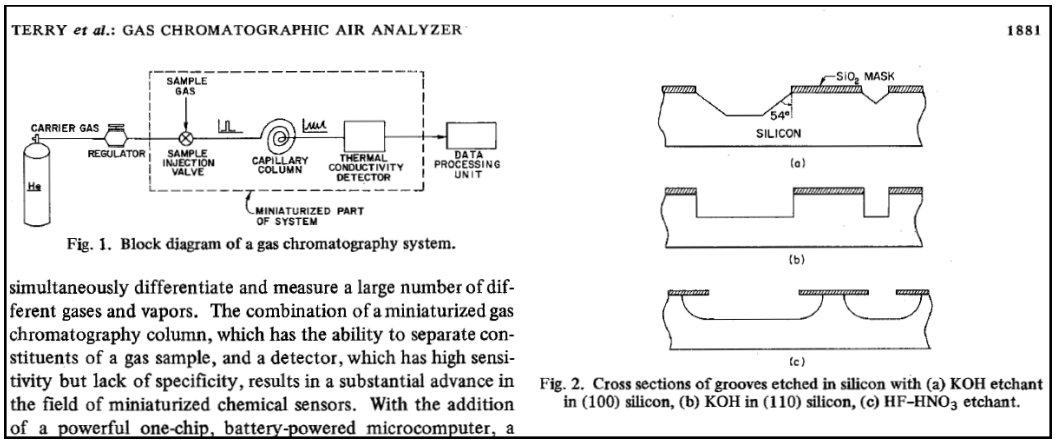

Figure 1.1: Design and fabrication technique for the first microchromatograph (Terry et al., 1979), extracted from the original paper. Reproduced with permission © 1979 IEEE.

The successful path in the development of LOC was marked by the main support of microfluidics and microfabrication. Microfluidics is the science and technology that deals with the behavior, control and manipulation of fluids at small scale (usually 10^{-9} to 10^{-18} litres), in small environments (Whitesides, 2006). Fundamentally, microfluidics treat with the special features of fluid at the microscale, like prevalence of phenomena associated to surface tension, viscous effects and wall properties. Microfluidics involves not only

fluid mechanics, in order to obtain a comprehensive approach to the phenomena implicated at this geometric scale, physics, chemistry and biology must be present.

LOC manufacturing method in the earlier years were developed in the 70's and 80's by the microelectronics industry, specially in the microprocessors development, using silicon and a few metals like aluminium or gold (Madou, 2002). To cover a broader range of applications in bioanalytics, new materials and microfabrication procedures were adapted. In this sense polymers and plastic materials play an essential role. More details on processes and materials for LOC manufacturing are given in next section.

At present, twenty years later, the interest in LOC is continuously growing. This interest is evident from the large number of publications and the appearance of dedicated journals and conferences (Oosterbroek and van den Berg, 2003). Also several companies have lead to a wide range of commercial products in health care, environmental monitoring, pharmaceutical and food industry (Reyes et al., 2002). Most of these applications are based on the analytical techniques modelled in this thesis, which are described in Section 1.3.

1.2 Microfabrication Techniques

The pathway to the LOC concept started with the development of the microfabrication methods by the microelectronics industry. This situation can be inferred by looking at Fig. 1.1. In this foundational work, Terry et al. (1979) manufactured the chromatograph channels by using lithography and wet etching of silicon, such as in the semiconductor industry.

Unlike microprocessors, LOC manufacturing processes lacks of standard libraries, due to the wide range of materials, fabrication techniques, and applications. This situation represents, nowadays, one of the largest barriers to the massive use of LOC (Koch et al., 2000).

In order to achieve a better understanding of LOC behavior, it is mandatory to know their manufacturing processes. This section offers a brief technical background on microfabrication techniques for LOC, aimed to improve the comprehension of later modelling process. For more details on microfabrication

techniques the reader is referred to the specific bibliography (Koch et al., 2000; Madou, 2002; Gad el Hak, 2006).

1.2.1 Silicon and glass manufacturing process

Disregarding their functional features, LOC could be defined as a set of microchannels, reactors, mixers, electrodes, pumps and heaters among other components. There exist two main processes to fabricate these structures: lithography and etching, which were taken from the semiconductor industry, and nowadays are used to define microstructures in non-polymeric materials (Tian and Finehout, 2009).

Lithography

The lithography process consists in transferring certain pattern from a support (mask) to another photosensitive material (photoresist) that is coating the surface of the interest material (substrate). After transferring the pattern, the substrate is processed by additive (doping, metal deposition, etc) or subtractive (etching) methods.

Figure 1.2 presents a scheme of a typical lithographic process. In this process, the mask is the first representation of the pattern that is going to be transferred. Characteristics of the mask are defined by the physicochemical properties of the photoresist (PR). These properties are related to the photosensibility range (wavelength) of the PR, and the reactions that this radiation triggers. If the reaction triggered is a solubilization, the PR is positive, in turn, if the reaction is a polymerization, the PR is negative. Commonly, the radiation is electromagnetic in the range of the near UV, but also, visible light, X-rays, or electrons beams are used (Kler, 2006). Due to this, mask has transparent and opaque regions, where the opaque regions have to reflect or absorb radiation. In the case of visible light and near UV, black ink in a transparent plastic film is enough, in other cases metallic layers in quartz supports are required. Distribution of the transparent and opaque zones are determined by the polarity of the PR, if it is positive, zones to be removed are transparent,

inversely if the PR is negative (Madou, 2002). Finally, after exposing the PR, the regions that are soluble are removed by the developer solution, leaving the substrate with zones exposed to carry out additive or subtractive processes.

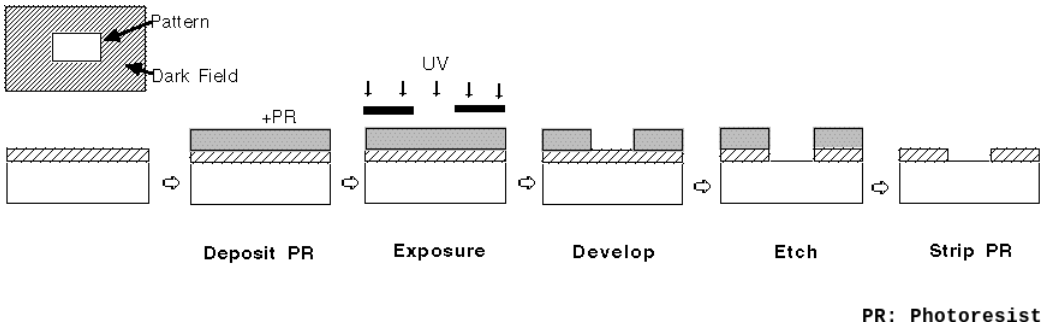

Figure 1.2: Example of a lithographic process for a positive PR, with a subtractive process.

Etching

The most important subtractive process in LOC manufacturing is etching. The etching process enables to define most of the microstructures present in LOC, such as channels, reservoirs and mixers (Korvink and Paul, 2006). After defining the pattern by using a lithographic process, the exposed regions on the substrate are etched by applying the etchant, in solution (wet etching), in a gas carrier (dry etching), or in a particle beam (Kovacs et al., 2002).

The wet etching process is a widespread method for manufacturing microfluidic platforms in silicon or glass. In this process the etchant solution reacts with the exposed surface of the substrate, creating a new compound without chemical affinity for the original structure, releasing from it and going to the solution. Results of this process strongly depend on agitation, etchant concentration, and temperature. Generally, the reaction velocity is the same in all directions, this situation is known as isotropic etching. Both glass and silicon admit isotropic etching with etchant solutions based on hydrofluoric acid, nitric acid or ammonium salts. Metallic layers can be etched with phosphoric acid, nitric acid or iodine solution (Maluf and Williams, 2004).

The main concern about isotropic etching is the poor capability to define vertical wall or structures with high aspect ratio.

Certain alkaline solutions have demonstrated the capability of etching silicon in an anisotropic way, that is, different etching velocities are achieved, for different crystal plane orientations. This requires the silicon to be a monocrystal. By using these anisotropic etchants (commonly solutions of potassium or ammonium hydroxide) vertical walls or high aspect ratio structures can be obtained (Bean, 2005). Figure 1.3 shows a silicon microchannel section, after performing anisotropic etching with KOH in the crystal plane 111.

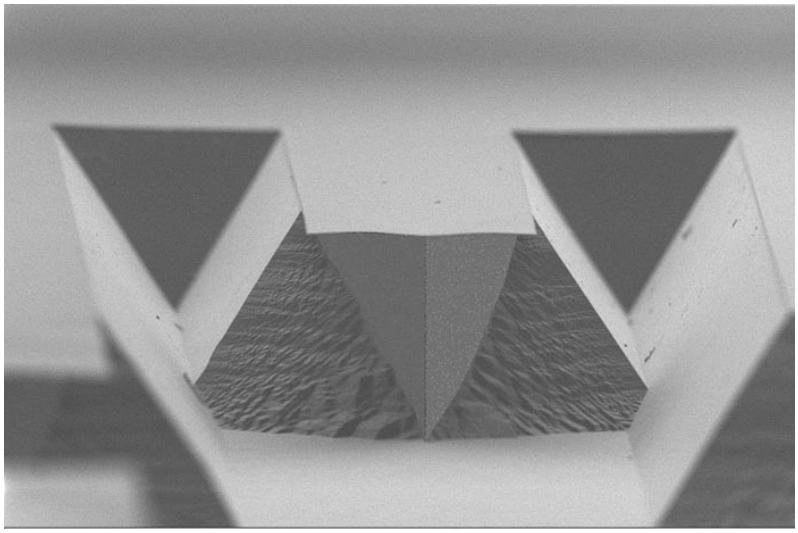

Figure 1.3: Channel section for a microchannel manufactured in silicon by using anisotropic etching in the plane 111.

1.2.2 Polymer manufacturing methods

Since the introduction of LOC, glass has been the preferred material for manufacturing. This is primarily based on the already mentioned fact that manufacturing methods derives from the semiconductor industry, and glass surface properties have been well characterized and developed by the traditional chromatograph and capillary electrophoresis users. However, the high cost of production of glass and silicon systems is driving the LOC community to seek

other materials. These materials are polymers that bring many benefits apart from cost reduction and mass manufacturing processes (Becker and Locascio, 2002). One of these additional advantages is the wide range of materials available, that allows designers to choose an specific polymer for an specific application.

Imprinting and hot embossing

Early methods used hot chromium wires for printing microchannels in polymer substrates. Nowadays, a silicon stamp is most commonly used as a tool for making polymer microfluidic devices. To make the silicon stamp, a silicon wafer with an orientation of the crystals 100 or 111 is etched anisotropically after a photolithographic process and the result is a raised three-dimensional inverted image of the desired microchannel network (Becker and Gärtner, 2000).

The imprinting process can be done at room or at high temperature depending on the nature of the polymer and the pressure exerted. To imprint or emboss microchannels, plastic material is cleaned and dried, and then is placed on top of the silicon stamp. The stamp and the polymer are then placed in a hydraulic press and pressure is applied during a time that is usually less than 10 min. Hot embossing is carried out at temperatures near the softening temperature of the plastic, and lower pressures. Also plastic devices can be printed at room temperature with high pressures. Hot embossing allows exact dimension reproducibility from the stamp. When devices are imprinted at room temperature, microchannel dimensions are much more dependent of various parameters such as the pressure, printing time and the properties of polymer itself. An advantage of the room temperature impression, is that manufacturing time is small compared to hot stamping. Reproducible prints can be done at room temperature in less than 2 minutes (Heckele and Schomburg, 2004).

Many common polymers have been successfully imprinted or hot embossed with excellent reproducibility in LOC manufacturing, these include

polystyrene, polyethylenetetraphthalate (PETG), polymethyl methacrylate (PMMA) polyvinyl chloride (PVC), and polycarbonate.

Soft lithography

A significant development in LOC development was the introduction of molding techniques for elastomers, known as soft lithography. In this technique, an elastomer polymer, mainly polydimethylsiloxane (PDMS), is casted onto a silicon seal, similar to those for hot embossing, and allowed to cure. After curing at room temperature, or a slightly elevated temperature to accelerate the process, the polymer is removed (Effenhauser et al., 1997). Once again, the seal of silicon can be used repeatedly in order to create hundreds of polymer microfluidic devices. In addition, seals can be made from softer materials such as SU-8 photosensitive (Renaud et al., 1998).
A major advantage of this manufacturing technique is that the PDMS can be easily bonded to PDMS, other plastics or glass substrates. The simplicity associated with sealing procedures has made this technology one of the most widely used for prototyping microfluidic systems (Duffy et al., 1998; Hillborg et al., 2000; Efimenko et al., 2002).

Soft lithography enables to fabricate three dimensional microfluidic devices. The fabrication of these devices requires the design of several silicon seals, which are then used to make individual layers of a multi-layer three-dimensional structure. The excellent adhesion between successive layer promotes the extensively use of this method (Anderson et al., 2000).

Laser photoablation

Microfabrication by laser ablation involves pulsed laser energy absorption by the polymer substrate. This absorption results in an electronic transition or in a local temperature rise, which causes the cleavage of chemical bonds between polymer chains. These electronic and thermal transitions also produce a shock wave, resulting in the expulsion of the products of polymer decomposition, leaving a cavity as the ablation product. The radiation sources are commonly excimer lasers of noble gas and the wavelengths are in the UV range. The

depth of the channels is determined by the energy of the pulses and the number of pulses delivered to a particular area. Many commercial polymers such as polystyrene, PMMA, nitrocellulose, polyethylene and polytetrafluoreltylene (Teflon) can be processed by laser ablation (Xu et al., 1998; Rossier et al., 2000). Laser ablation can be performed in direct writing mode or scanning mode. The scanning mode requires the use of masks constructed in quartz to allow transmission of UV radiation and opaque areas with chromium or nickel layers.

X-ray lithography

X-ray lithography has been adapted to fabricate polymer microchannels. The most common substrate material used in this process is PMMA because it exhibits high X-ray absorption (soft X-rays of 0.7-0.8 nm) and is sensitive to the degradation of X-rays. To make structures by X-ray lithography, a quartz-chromium mask is generated for the first time to define the pattern (Ford, 2001). With this pattern a second mask of gold in a Kapton support is created. The thick gold layer absorbs X-rays to protect polymer substrate behind, while the Kapton sections without the gold layer are transparent to X-rays.

For PMMA substrates, X-ray exposure induces a series of reactions, resulting in cleavage of a variety of soluble olygomers. The exposed, degraded polymer, is dissolved by a developer solution that dissolves the reaction products, thus forming a microcavity. This process can yield high aspect ratio structures, with straight and smooth walls, as shown in Figure 1.4. The channel depth depends on the X-ray energy and time of exposure. This process can be used to fabricate microchannels or it can be used to generate stamps (similar to silicone seals) for printing or injection molding (Lee et al., 1998).

Bonding

All manufacturing methods described, besides the channel construction, requires post-fabrication sealing of the microchannel network to form an enclosed structure. Sealing polymer LOC is usually much simpler than for silicon or glass substrates and often can be achieved by using low temperature thermal

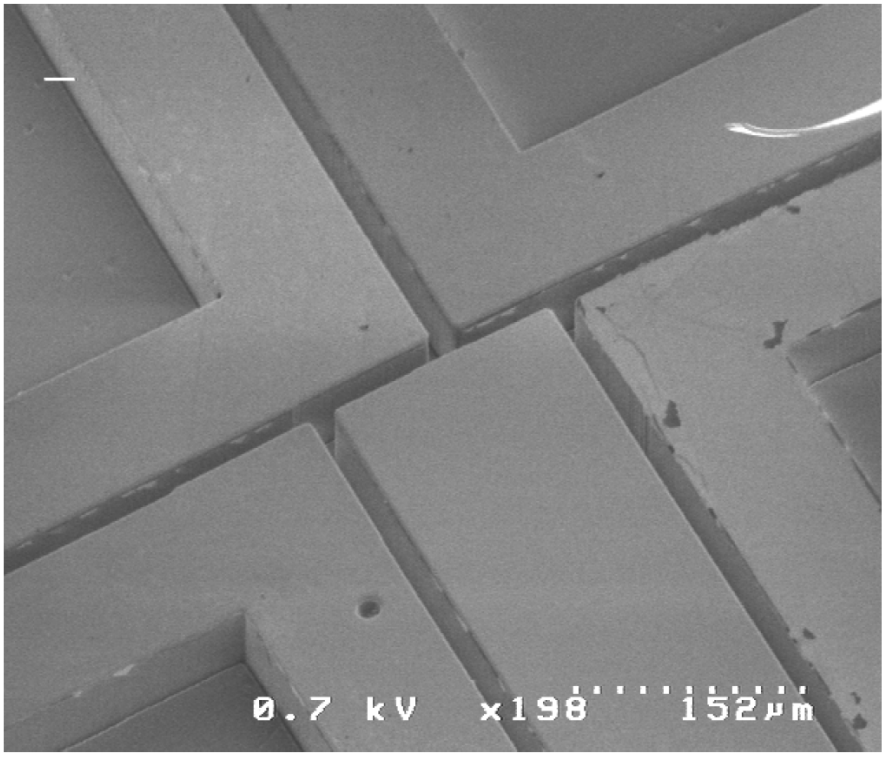

Figure 1.4: Microchannel network manufactured in PMMA by using X-ray lithography (Ford, 2001).

annealing (Roberts et al., 1997). The polymer substrate can be used to form the seal or, alternatively, a polymer with a lower glass transition temperature can be used to avoid deformations on the microchannel during the process. Elastomeric polymers as PDMS have excellent adhesion to a variety of substrate materials and can be used to enclose microchannels with non-permanent stamps (Barbier et al., 2006). To form a permanent seal on PDMS, Duffy et al. (1998) described the plasma oxidation of surfaces for bonding material themselves, or to other substrates such as glass, silicon, silicon oxide, quartz, silicon nitride, polyethylene, polystyrene, and glassy carbon.

1.2.3 Metal deposition methods

Thin film deposition is a classical and widespread technique in different fields of the science and industry. In order to carry out depositions, physical vapor de-

position (PVD) is the most widely used technique. Principal PVD techniques in LOC manufacturing are thermal evaporation and sputtering.

Evaporation

Thermal evaporation is one of the oldest techniques in deposition of thin films. It is based on evaporation or sublimation of a material by heating it immersed in a very low pressure environment. Low pressure levels are important to prevent intermolecular collisions between the atoms of the substance to deposit and the atoms of air, and also, to prevent redeposition of contaminants and unwanted reactions with oxygen molecules. There are many different methods to achieve material evaporation. The most common method found in academic laboratories is the Joule heating of a tub or filament made of a highly refractory metal such as tungsten. The method is simple, but generates a high amount of impurities that deposit on the substrate. For industrial applications, Joule heating has been replaced by radio frequency induction or electron beam heating. For the electron beam heating, the electron emission, with an energy range between 3 and 20 keV, is focused onto the material, which is contained in a structure of water-cooled copper. The flow direction of electrons is magnetically controlled. In order to avoid undesired chemical reactions, the target material is cooled. This method not only produces high quality films but also provides the ability to deposit thick films at high deposition speeds. In some cases, electron beam can be replaced by a high power laser (Madou, 2002).

Sputtering

Sputtering process consist in applying to the target (a disk made of the material to be deposited) an extremely negative electric potential in order to bombard it with argon ions, which are created in a gas plasma. Atoms are released from the target due to the transfer of momentum and are deposited by condensation on the substrate placed at the anode. The target material and the substrate form a capacitor between them, where argon plasma is generated. Argon ions are accelerated toward the target, and neutral atoms removed from the surface migrate straight to the substrate. In the case of metallic substrates,

direct current can be used, but for dielectric substrate materials alternating current is mandatory and it is applied in the range of radio frequencies. In this last case, the target and the substrate are constructed of different sizes, then, the heterogeneous charge concentration determines the required polarity. The direction followed by the detached atoms is not random, which ensures a more efficient deposition than in the evaporation process. Sputtering is preferred in many applications because it serves to deposit a wider range of materials (Koch et al., 2000).

1.3 Analytical Methods in LOC

As mentioned above, the LOC technology lies on microfabrication and microfluidics. One of the main task of microfluidics is to develop models and techniques to drive or pump fluids through channels and the whole LOC network. A major problem for conventional pumps available in the 90's was the high values of pressure necessary to transport fluids in microchannels (Landers, 2007). Under this situation, electroosmotic pumps and voltage actuated systems appeared as attractive and feasible options. Then electroosmotic pumping and electrophoretic separations became the most popular methods applied in LOC. In what follows, electrokinetic phenomena and electrophoresis are briefly introduced in order to understand the basis of the important electrophoretic applications in LOC described in subsequent section. Finally, another important analytical techniques, also developed in LOC, are presented.

1.3.1 Electrokinetic phenomena

Generally, most substances will acquire a surface electric charge when brought into contact with an aqueous (polar) medium. Some of the charging mechanisms include ionization, ion adsorption, and ion dissolution. The effect of any charged surface in an electrolyte solution will be to influence the distribution of nearby ions in the solution. Ions of opposite charge to that the surface (counterions) are attracted towards the surface while ions of like charge (coions) are repelled from the surface.

This attraction and repulsion, when combined with the mixing tendency resulting from the random thermal motions of the ions, leads to the formation of an electric double layer (Probstein, 2003). The electric double layer is a region close to the charged surface in which there is an excess of counterions over coions to neutralize the surface charge, and these ions are spatially distributed in a diffuse manner. Evidently there is no charge neutrality within the double layer because the number of counterions will be large compared with the number of coions. When moving away from the surface, the potential progressively decreases, and then vanishes in the liquid bulk.
When the mobile charges present in the diffuse region and an electric field tangential to the surface interact the electrokinetic phenomena arise. The four electrokinetic phenomena are (Shaw and Williams, 1968):(i) Electroosmosis (movement of liquid relative to a stationary charged surface by an applied electric field), (ii) Electrophoresis (movement of a charged surface plus attached material relative to stationary liquid by an applied electric field.), (iii) Streaming potential (electric field created when liquid is forced to flow along a stationary charged surface),and, (iv) Sedimentation potential (electric field created when charged particles move relatively to a stationary phase). For a more detailed discussion about the electrokinetic phenomena, refer to section 3.1.2.

Electroosmotic flow

Electroosmosis was observed for the first time in 1809 by Reuss (1809), who report that the application of an electric field caused the displacement of water in natural porous materials.

Electroosmotic flow in microchannels ground on the existence of an excess of ions in the fluid near solid walls. When an external electric field is applied in the axial direction of a channel, the electrical forces acting on excess ions drag the surrounding liquid and then electroosmotic flow develops. Figure 1.5 shows an schematic diagram of the electroosmotic flow, and can be inferred from it, the typical velocity profile, that tends to be plane when the channel width is larger than the double layer length.

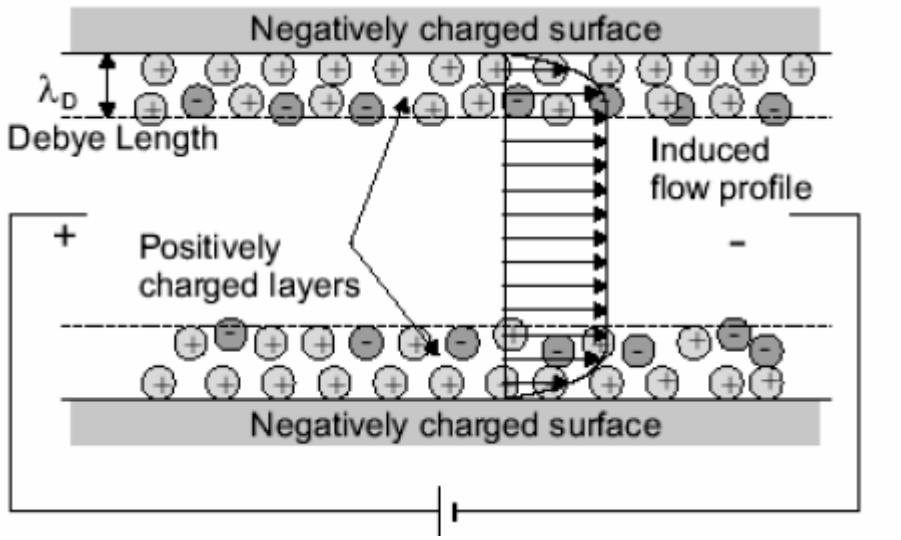

Figure 1.5: Electroosmotic flow fundamentals diagram.

Electrophoresis

Electrophoresis is the relative motion of charged particles to the bulk or surrounding liquid. The magnitude of this relative velocity depends on the so-called electrophoretic mobility. Differences on electrophoretic mobility result from balance between electric forces, and the hydrodynamic friction due to the viscosity of the surrounding solution. Electrophoretic separation techniques are based on these differences on mobility of ions by applying an external electric field. Figure 1.6 shows an schematic diagram about electrophoresis, in which reader can infer the relationship between molecule characteristics (i.e. charge and mass) and electrophoretic mobility.

The most known and widely used theory of electrophoresis were developed by Hermann von Helmholtz (1879) and Marian Smoluchowsky (1903), more details about theory and modelling of electrophoresis in LOC will be given in Chapter 3.

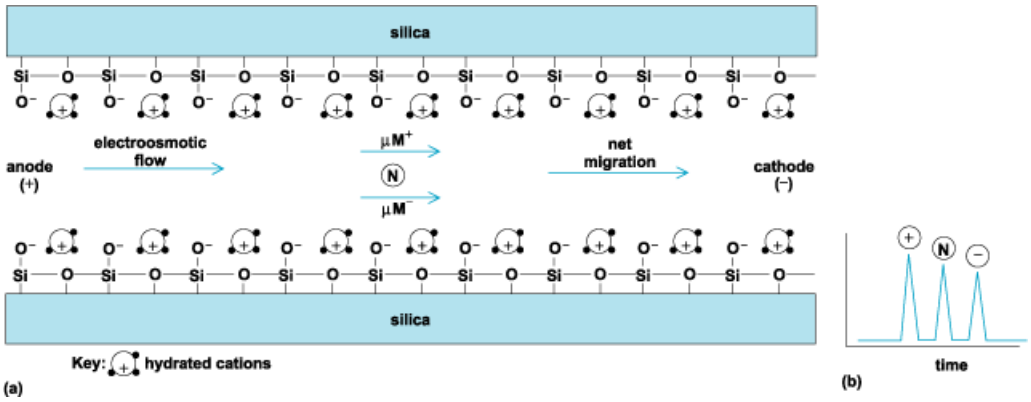

Figure 1.6: Electroosmotic flow and electrophoresis fundamentals diagram.

1.3.2 Electrophoretic separations

Electrophoretic techniques, which are widely used in chemical and biochemical analysis, have been miniaturized in the last 20 years and now represent one of the most important applications of LOC technology (Tian and Finehout, 2008). Electrophoretic separations comprise a group of different techniques such as: capillary zone electrophoresis (CZE), isoelectric focusing (IEF), isotachophoresis (ITP), free flow electrophoresis (FFE), and capillary electrochromatography (CEC) (Peng et al., 2008; Wu et al., 2008).

Capillary zone electrophoresis

Developed in LOC, capillary zone electrophoresis (CZE), consist in a straightforward adaptation of the conventional capillary electrophoresis (CE) proposed by Jorgenson and Lukacs (1981). In an CZE assay, an electric potential difference is applied at the ends of a capillary tube or a microchannel in order to obtain a longitudinal electric field. This electric field exerts forces on the charged molecules in solution resulting in different electrophoretic velocities enabling the separation due to this difference. In most situations, the velocity of migration of an analyte will also depend upon the rate of electroosmotic flow (EOF) of the buffer solution. As a consequence, electrophoresis and EOF are strongly related.

Figure 1.7: Herman von Helmholtz (1821-1894)

Figure 1.8: Marian Smoluchowski (1872-1917)

CZE performed in LOC gathered significant attention because of the potential applications and overall device performance. Although the early developments focused on the field of DNA analysis (Woolley and Mathies, 1994), CZE in LOC has been rapidly and successfully adapted to many biological, environmental, and industry applications (Erickson and Li, 2004). Numerical simulations of these devices are performed in section 5.2.1. Figure 1.9 shows a CZE chip manufactured in glass during the period of realization of this thesis.

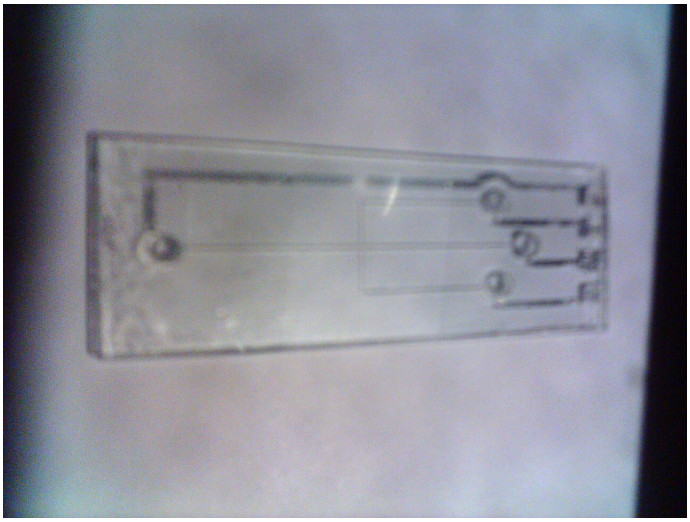

Figure 1.9: CZE chip manufactured in glass by the author of this thesis (2006 Pablo A. Kler).

Isoelectric focusing

Isoelectric focusing (IEF) is a powerful electrophoretic method for characterizing proteins and other biomolecules. IEF separates and focus amphoteric substances around its isoelectric point (pI). At a pH below the pI, a molecule will be positively charged and, if an electric field is applied, it will migrate towards the cathode. While it moves through a gradient of increasing pH (previously established), the overall charge will decrease until it reaches the pH region that corresponds to its pI. Similarly, if the molecule is at a pH above its pI, it will migrate travelling through a gradient of decreasing pH, towards the anode (see Fig. 1.10). At this point it has no net charge and so migration

ceases. As a result, the molecule becomes focused into sharp stationary bands with each specie positioned at a point in the pH gradient corresponding to its pI. This technique is capable of extremely high resolution with proteins differing by a single charge being fractionated into separate bands.

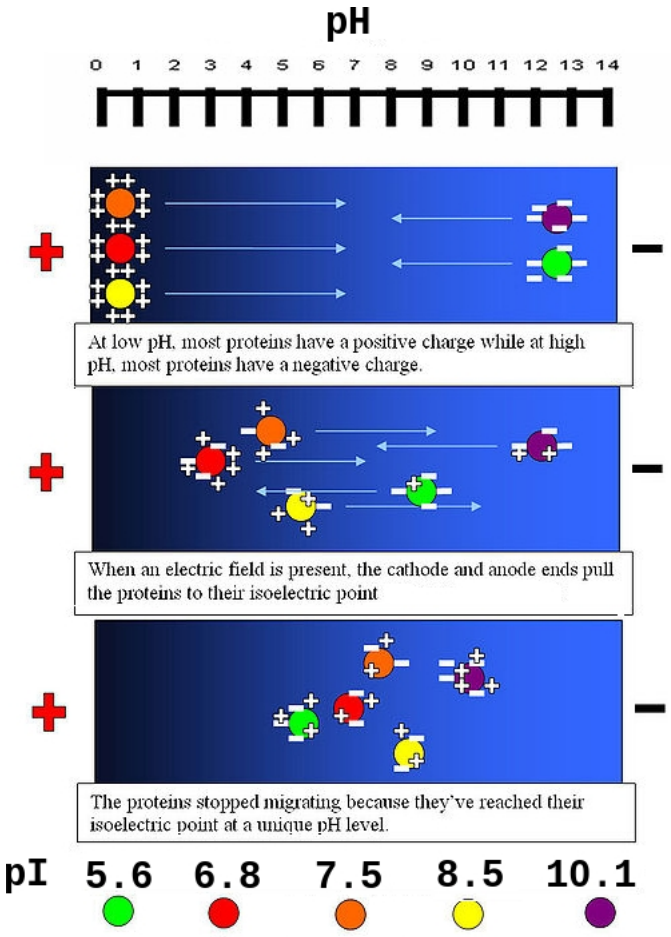

Figure 1.10: Isoelectric focusing schematic operation.

The pH gradient is established by using a solution of small molecules such as polyampholytes with varying pI values. This process can be done in solution (via *carrier ampholytes*) or in a polyacrylamide gel matrix (*immobilines*). LOC have been employed to perform different applications of IEF such as protein studies (Wu et al., 2001) or sub-cellular organelles (Lu et al., 2004). Numerical simulations of these process are performed in sections 5.1.1 and 5.1.2.

Isotachophoresis and stacking

Isotachophoresis (ITP) is used in the separation of a variety of ionic compounds, ranging from small molecules, like metallic ions, to large molecules like proteins. This electrophoretic technique works using a discontinuous electric field to create sharp boundaries between the sample constituents. ITP is also a powerful sample pre-concentration (stacking) technique which is useful in the analysis of low concentration species.

In conventional electrophoresis almost all the electric current is carried by the electrolyte buffer. The sample constituents migrate under the influence of an homogeneous electric field. The buffer determines the pH of the medium as well as the dissociation degree of the sample elements according to their dissociation point (pK) values. In an ITP assay, a heterogeneous media is determined due to the analytes and the leading and terminating electrolytes (LE and TE, respectively). The LE is composed of high mobility ions and, has a mobility higher than the analytes. In turn, the analytes have mobilities higher than the TE components. Moreover, the pH of LE and TE could be different, then analytes pI have to be inside this range. When an electric potential difference is applied, with the anode at the LE side, electrolytes and sample will migrate at different velocities, arranging in discrete bands in order of mobility. This bands generates conductivity gaps in which electric field is higher, then at this band-gaps migration increases focusing samples. Consequently, ITP provides both separation and focusing simultaneously.

ITP is a simple and effective preconcentration and separation method which can be easily integrated on a chip prior to other on-chip operations, especially CZE. Most of the published works on miniaturized ITP were focused on the separation of small organic molecules (Graß et al., 2002) and metal ions (Prest et al., 2005) which were primarily used in the food and beverage industry and for water analysis. ITP stacking and separation of proteins on chips has so far received relatively little interest but it is continuously growing (Cui et al., 2007; Chen et al., 2006). ITP numerical simulations are presented in section 5.2.2.

Free flow electrophoresis

Free flow electrophoresis (FFE) involves a set of continuous techniques for electrophoretic separations. These methods provide bands across the separation chamber and thus a continuous supply of separated components at the exit of the chamber. In FFE, charged particles are injected into a liquid carrier with an electric field applied perpendicular to the flow direction. Particles are deflected from the flow streamlines at an angle arranged by the vector composition of the flow advection and the migration (determined by the sample mobility and the applied electric field strength). Sample compounds with different electrophoretic mobility have different deflections and can be collected separately at the end of the separation area. Since the principle of the FFE was described (Strickler et al., 1966), this technique has found application in chemistry and biochemistry mainly for the separation of proteins (Obermaier et al., 2005), enzymes, membrane particles, organelles, and cells (Turgeon and Bowser, 2009).

The most relevant modes of FFE include free flow zone electrophoresis (FFZE), where the separation of analytes is based on their charge to size ratio (Xu et al., 2005), and free flow isoelectric focusing (FFIEF), where the separation and focusing of analytes takes place according to their pI (Kohlheyer et al., 2007). Figure 1.11 shows a FFIEF microdevice manufactured in glass.

Free flow methods as FFZE or FFIEF allow continuous operation and the possibility of coupling a second electrophoretic method. Thus two-dimensional electrophoretic (2DE) assays are obtained, which are very demanded in proteins studies.

Multidimensional separations

One of the more promising applications of LOC is the possibility to perform robust multidimensional protein separations. Multidimensional separations consist in the coupling of two or more separation methods, which may be done by multiplexing single separations temporal or spatially. If the methods employed are based on different physicochemical properties of the analytes (orthogonality), separation performance is calculated as the product of perfor-

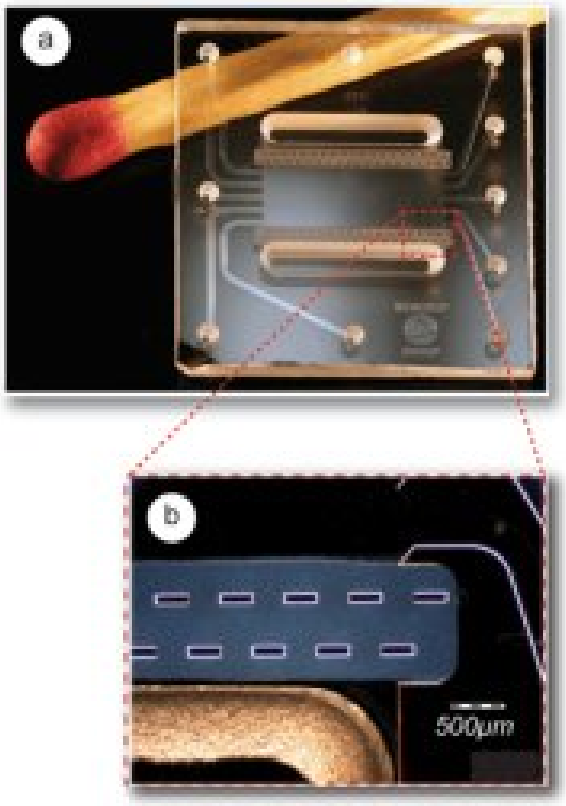

Figure 1.11: FFIEF chip manufactured by the BIOS group, University of Twente, The Netherlands (Kohlheyer et al., 2007). Reproduced with permission © 2007 ACS publications.

mance methods separately (O'Farrell, 1975).

The idea of two dimensional separations comes from the well known SDS-PAGE, a method to carry out IEF and electrophoresis consecutively in a polyacrilamide gel support. Nowadays this assay is the most employed worldwide in proteomic studies, although, it remains expensive and slow. A major challenge faced in proteomic analysis is the high number of proteins present in a typical biological sample, with a high dispersion on relative abundances. Under this situation, LOC technology has to provide reduction of the dynamic range and enhancement of detection sensitivity without substantially sacrificing analytical throughput.

There are many combinations of methods in two, three and even four sepa-

ration dimensions and continuously appear new techniques providing better resolution and thresholds. The main issue in these methods are the coupling strategy between separation stages: problems on sample dispersion and crosstalking are common (Tia and Herr, 2009). Numerical simulation of two dimensional electrophoretic separations are included in sections 5.2.3 and 5.2.4.

Capillary electrochromatography

Microchip based capillary electrochromatography (CEC) consists in a hybrid method from CZE and liquid chromatography (LC), combining the best features of each method. Separation mechanism of CZE is based on differences in molecular mobilities, while LC is based on the difference of partition coefficients between the two phases. CEC is capable to separate both ionic an neutral compounds making use of these two properties. Compounds velocity will result from the combination of electrophoretic properties and affinity with the stationary phase.

EOF velocity profiles reduces dispersion of the analytes, increasing column efficiency, and avoiding the use of high pressure pumps (difficult to construct at the microscale). Additionally to the affinity properties, the stationary phase have to allow EOF pumping (charged surface). The columns could be manufactured by micromachining (fractal distribution of microposts), by *in-situ* polymerization (continuous columns), or by packing classic materials for columns in conventional LC (packed columns) (Pumera, 2005). Despite its well known advantages, CEC is not yet widespread in the LOC community, mainly due to constructive difficulties.

1.3.3 Other analytical methods

The already mentioned electrophoretic or chromatographic methods are based in the spatial separation of the compounds by using its physicochemical properties. There exist another set of methods that are based on biological properties of the analytes, like its antigenic properties or its metabolic affinity, which are used to improve detection or sensing, as complements of separation. These methods have an extremely high sensitivity, but are often expensive due to

the need of specific reagents. The two most popular assays based on these properties are immunoassay and enzymatic based assays.

Immunoassay

Immunoassay presented by Yalow and Berson (1960) in the form of *radioimmunoassay* is still today one of the most powerful and important analytical method used in clinical diagnoses and biochemical studies, due to its extremely high selectivity and sensitivity. The antibody based current methods have two generic classifications: homogeneous and heterogeneous. The first take place in a liquid solution media, and the second implies the immobilization of an immune component (commonly the antibody) to a solid surface. Implementation of both in LOC has been accomplished with success (Vilkner et al., 2004). Most of the homogeneous immunoassay in LOC have been based on CZE (Chiem and Harrison, 1998) reducing considerably assay time.

Heterogeneous assays have been received much attention due to the widely spreading of the enzyme linked immunosorbent assay (ELISA). These kind of conventional immunoassays require a lot of time to perform reaction process due to the slow diffusion process. High area-to-volume ratio, and lower volumes of sample and reagents that offer LOC, speeds up this process. Heterogeneous immunoassays developed in LOC avoid the long assay time, and common human errors in liquid handling.

These facts are promoting immunoassays in LOC as great candidates to develop point-of-care diagnostic applications for cancer and infectious diseases. Numerical simulations of LOC immunoassays are shown in section 5.2.5.

Enzymatic assays

In situations where the analyte of interest is present in a very low concentration or belongs to a very complex matrix, high sensitivity and selectivity, respectively, may required. This cases are common in DNA analysis and food quality control assays. In this cases enzymes are employed to perform analysis with the required performance.

Polymerase is an enzyme related to the synthesis of DNA. Polymerase chain

reaction (PCR) is a classical technique that relies on thermal cycling used to amplify DNA samples in order to sequence them. Microfluidics platforms to preform PCR and CE of DNA samples were introduced during the genome project (Wang et al., 1998).

In food industry, enzymatic analysis are common in detecting pathogens, allergens and genetically modified components (Skurtys and Aguilera, 2008). An enzymatic assay developed in LOC is numerically simulated in section 5.2.6.

Chapter 2

Relevant numerical models in LOC

The main contribution of this thesis is the development and testing of a set of numerical tools that are aimed to improve the designing process of LOC. Numerical modeling and simulations of electrophoretic techniques have been used since the emergence of scientific and personal computers, improving experimental set up and prototype geometries, enhancing buffer and sample composition, and optimizing operational parameters. In this chapter, these works, with its competences and limitations, are reviewed in order to provide the reader with objective elements to better understand the contribution of the present thesis. In section 2.1, classical numerical models in capillary electrophoresis are reviewed, then in section 2.2 milestones numerical simulations in microfluidics are presented, and finally section 2.3 is focused in numerical simulations of analytical processes in entire LOC.

2.1 Numerical modelling in Electrophoresis

At the end of the seventies computers became available for researchers that began to develop simulation models for electrophoresis. These efforts were driven by the interest in exploring the dynamics of the processes of

electrophoresis, including different techniques as CZE, moving boundary electrophoresis (MBE), ITP and IEF. Additionally, the interest was addressed to the identification of the physicochemical processes involved in the separation of charged and uncharged compounds in solution under the influence of an electric field. The models were (and currently they are) based on equations derived from the concept of transport in solution, with some conditions that the user enters, such as concentrations, mobilities, diffusion coefficients, pK values, intensity of electric field or current density, length column and its segmentation. Thus sample profiles along the column as a function of assay time were predicted.

The advantages of the dynamic simulations are: (i) the ability to determine the conditions for separations before the laboratory experiments were carried out, (ii) the possibility to obtain insight into certain combinations of experimental conditions, which provides understanding of the patterns and peaks, (iii) the optimization designs of systems in order to improve detection capacity, and (iv) the use for educational purposes, in order to bring students the possibility to carry out many virtual experiments before facing the bench-top equipment (Thormann et al., 2009). In addition to the dynamic models, there exists other important models such as those for rapid evaluation of buffer systems and analyte separability in CZE (Găs et al., 2001), IEF and ITP simulation models which can predict the steady-state shape and composition of zones but not the evolution in time (Palusinski et al., 1981; Shimao, 1986), and simple training software for electrophoresis (Reijenga et al., 1995).

Dynamic simulations are based on equations that include different transport and reaction phenomena. These equations are partial differential equations in time and space, which can be solved numerically using computers. These models calculate the transport of each component through electrophoretic space as a result of electromigration, diffusion, bulk flow, and reactions such as protolysis and, in some cases, also interaction of solutes with electrolyte additives or column walls.

Many dynamic models of various degrees of complexity have been described in the literature (Bercovici et al., 2009). Moreover, an stochastic simulation model for CE has been reported. Unlike the dynamic models mentioned above, this approach is based on modelling the trajectories of each individual molecule, therefore it requires very powerful computers to calculate the motion of a statistically significant number of molecules (Newman and McGuffin, 2005).

Scientists from the Universities of Prague, Berne and Arizona began to build the first dynamic models for electrophoresis equipment to explore the fundamentals of electrokinetic separations. The first models of the seventies (Moore, 1975; Găs, 1975) for ITP and MBE on free fluids were restricted to strong electrolytes and can considered the first electrophoresis dynamics simulation models. The first dynamic models able to predict the behavior of weak electrolyte systems were developed in the eighties by Bier et al.; Radi and Schumacher; and Roberts et al.. The model of Bier et al. (1983), which led to a unified view of all the basic modes of electrophoresis, was widely used to characterize a large number of configurations of electrophoresis (Mosher et al., 1992). It also simulates the behavior of proteins by using effective and mean square valences that are determined from titration data (Mosher et al., 1993). Radi and Schumacher (1985) model is the pioneer work in using kinetic constants of association and dissociation to describe protolysis. The first model with EOF-based transport electromigration and diffusion was presented by Dose and Guiochon (1991). This approach, in which only strong electrolytes are considered and the constant EOF is treated as plug flow, has been applied to the modeling of CZE and ITP.

With the advent of computers and the growing popularity of CE separations in fused silica capillaries, many of the 1-D dynamic simulators have been improved. Hruška et al. (2006) improved their first model with the addition of weak electrolytes, an approach that resulted in a complete package that can solve systems with any number of mono and multivalent electrolytes

and ampholytes (SIMUL5 5 and Peak Master 5.2, available as freeware at `http://www.web.natur.cuni.cz/~gas/`). Figure 2.1 shows a screen-shot of Peak Master 5.2 after solving an electrophoretic separation of sodium, lithium and potassium.

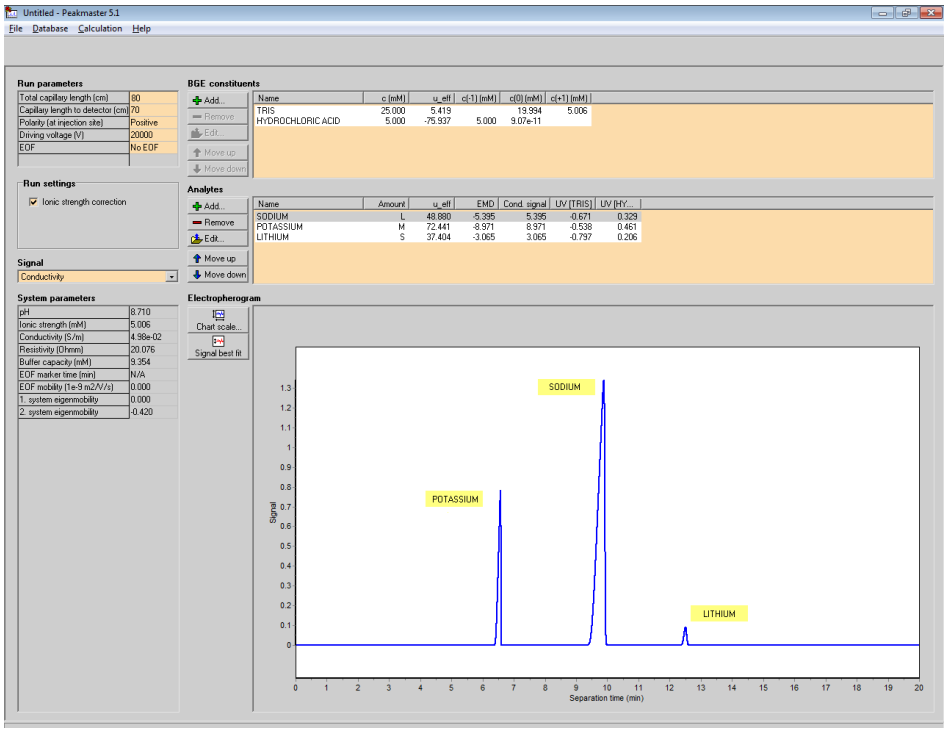

Figure 2.1: Screen-shot of Peak Master 5.2 running for separation of sodium, lithium and potassium, by using a TRIS-HCl buffer.

The model developed by Mosher et al. (GENTRANS), is based on the dynamic simulator from Saville and Palusinski (1986), and was modified for a more realistic treatment of the proteins, application of a plug flow and in situ estimation of EOF using wall titration data as input. It can control strong and weak electrolytes, simple ampholytes univalents, peptides and proteins (currently limited to 150 items total), and runs on voltage gradients are usually employed in experimental work (Thormann et al., 2004). Recent efforts have been done by Yu et al. (2008) and Bercovici et al. (2009) with new integration schemes also for 1-D simulations; the latter

being available as *Stanford's Public Release Electrophoretic Separation Solver (SPRESSO)* in `http://microfluidics.stanford.edu/spresso`. On the other hand, Shim et al. (2007) reported a complete model implemented by the finite volume method (FVM) in 2-D for micro-geometries in which proteins are described as compounds with multiple charge states.

To summarize, it is worth to stress that all these simulation models are aimed to capillary electrophoresis. This situation enables the massive use of 1-D models implemented by using the finite differences method (with the exception of the work of Shim et al. (2007), and the flux corrected method used by Sounart and Baygents (2007)). Non-linear relationships involving electrolyte composition, electric properties of the medium and walls, and samples are taken into account globally (only present in the work of Thormann et al. (2004)), avoiding strong coupling between equations. All these important works have founded the basis for more complex numerical simulations for analytical process in LOC, but they lack of the description of the fluid mechanics. Microfluidic simulations reviewed in the next section are the complement needed to obtain comprehensive LOC numerical models.

2.2 Computer Simulations in Microfluidics

LOC technology has successfully grown up due to the support of different prior disciplines. With the publication of the paper of Manz et al. (1990a), texts containing the foundations of microfluidics appeared, such as the books of Hunter (1989) and Probstein (1989). Since then, the support of microfluidics was essential to the LOC development.

Theoretical background developed by microfluidics provided the differential equations that govern physicochemical phenomena that occur in LOC. However, solving these equations for domains or geometries typically proposed in microfluidic still have some extra complications, even by using numerical approaches.

In microfluidics, there exist different factors that turns the numerical simulation of transport phenomena more complicated, and thus distinguish it from its macro counterpart. These factors can generally be divided into four different groups (Erickson, 2005). The first complication, and often more important from the numerical point of view, is the range of relevant length scales involved, which can vary up to seven orders magnitude: from the double layer thickness in nm, to channel lengths and substrate size in cm. Secondly, the reduction of the size scale significantly increases the relative importance of the surface and interfacial phenomena, notably the electrical double layer, the surface tension and channel wall roughness. Third, the rapid and localized changes on fluid and material physicochemical properties (e.g., viscosity, electrical conductivity, ionic strength) can also occur in many systems. However, the most challenging and interesting issue in computer simulation of transport in LOC is the physical nature of different relevant phenomena: microfluidics, transport, micromechanics, microelectronics, optics, chemical and biological, thermodynamics and reaction kinetics. This section is written assuming certain rudimentary knowledge in traditional pressure-driven flow and electrokinetic phenomena. These concepts and the equations related to them, will be explained in detail in sections 3.1 and 5.1.2.

2.2.1 Flow and species transport

Microfluidic numerical simulations has been historically addressed to the study of fluid flow and transport of species in common channel structures present in LOC that use traditional pressure or electrokinetic phenomena as the main driving force. Many of these simulations have been focused on the application of numerical techniques to the study of such fundamental microfluidic problems as species mixing, sample dispensing and analysis of dispersion for CZE in LOC (Li, 2004). Other simulations were aimed to determine global operating parameters such as electric potentials, pressure drops or net flows. These models allows the designer or the experimentalist to have quick approximations to the device behavior with very low computational

cost (Erickson and Li, 2004).

Simulation of microfluidic networks

In some situations, simulations tend to be very localized by examining in detail a particular region of a microfluidic system. This is usually done in order to concentrate computational resources on the problem instead and losing interest in capturing the flow field or transport phenomena for the entire network. In opposition, development of techniques for global microfluidic network modeling consist is an important tool aimed to conduct LOC prototyping or process optimization. One of the most impressive techniques to carry out such analysis was presented by Kirby et al. (2002) who developed a integrated circuit and microfluidic simulator that allows coupled simulation of flow, structure, thermal and electrical domains using *SPICE* for circuit simulation and their *Nektar* Microfluidics code (Kirby et al., 1999). Qiao and Aluru (2002) also demonstrated a technique based on passive electrical circuit to calculate fundamental parameters on electroosmotic or pressure-driven flow in complex microfluidic networks (see Figure 2.2).

Xuan and Li (2004) described an interesting model for pressure or electroosmotic driven flow in microfluidic networks with phenomenological coefficients from non-equilibrium thermodynamics to describe the effects of channel size and surface properties. Berli (2008) presented a model to predict flow rate ad electric current as a function of applied potentials and pressure gradients in complex microfluidic networks.

Dispensing, dispersion and mixing

As mentioned above, some of the first numerical simulations of flow and species transport were aimed to electrokinetic focusing and sample dispensing techniques. In one of the first of these studies, Patankar and Hu (1998)

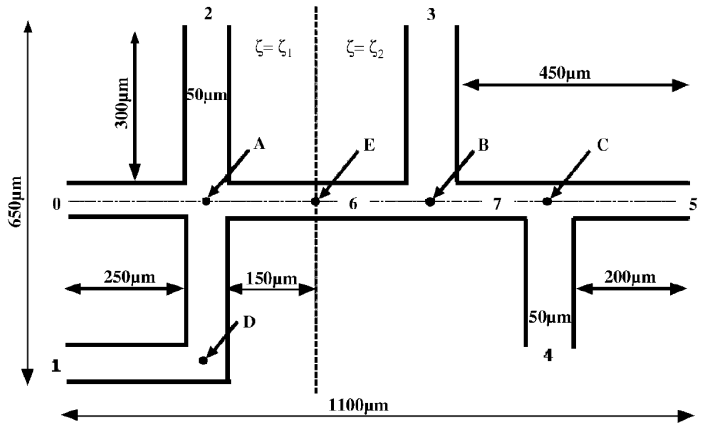

(a) Microchannel network geometry.

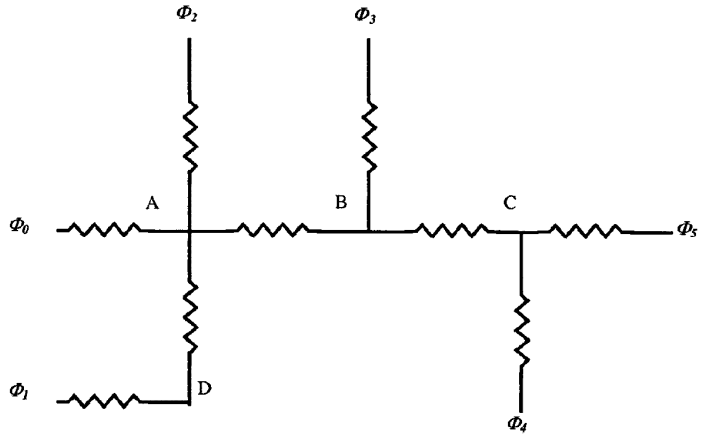

(b) Circuit model to compute electric potential distribution.

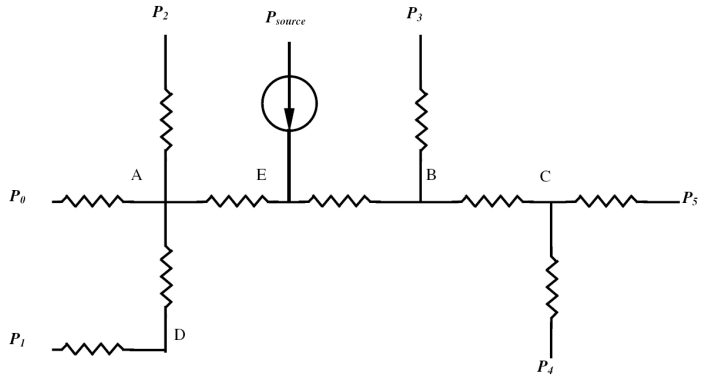

(c) Circuit model to compute pressure distribution.

Figure 2.2: Microchannel network modelling by Qiao and Aluru (2002). Reproduced with permission, © 2002 IOP Publishing.

examine the electrokinetic flow field at the intersection of a cross-shaped network, then, Ermakov et al. (1998) extended that work by analyzing focusing and mixing in those geometries, later dispensing was discussed (Ermakov et al., 2000). Another foundational work by Bianchi et al. (2000) presented simulations of electrokinetic flow in a T-junction by using finite elements method (FEM). Some results of this work are shown in Figure 2.3. Based on these initial studies many works have contributed to develop advanced numerical simulations and used them to improve mixing and dispensing techniques (Li, 2004; Tabeling, 2005; Karniadakis et al., 2005; Luo et al., 2010).

Due to the extensive use of LOC by the scientific community, new problems and limitations arrives, then computational simulations are supporting many optimization process to overcome these situations. One of the first problem detected was the dispersion of sample in turns. In addition to several excellent analytical and experimental research (Culbertson et al., 1998; Griffiths and Nilson, 2000), a series of important studies have examined basic numerical solutions to this problem by focusing on development of novel turn geometries. In a relevant study, Molho et al. (2001) coupled numerical simulations with optimization analysis to develop a general turn geometry for minimizing the dispersions. Also noteworthy is the work of Bharadwaj et al. (2002) who used numerical simulations as part of a broader analysis in the design and optimization CE chips. A particularly unique aspect of this study was the inclusion of fluorescence detector models to better characterize the system. Another interesting work was presented by Yang et al. (2005) in which sample dispersions due to the non-flat EOF velocity profile are analyzed. Non-flatness of the velocity profile arise due to the end-effects at expansions and contractions in connexions between channels and reservoirs. Recently, Zhu and Xuan (2009) performed experiments and numerical simulations to study particle dispersions on electrophoresis performed in curved microchannels.

Systems exhibiting spatial gradients in the electrolyte conductivity consist in an important subclass of electrokinetic flows commonly found in LOC applications such as sample stacking and IEF. The introduction of a non-linearity

in the coupled electric field flow and transport system significantly complicates the modeling process and leads to an interesting class of problems. This problems will be treated extensively in sections 3.2.2 and 5.2.2. Several works have examined this issue including those by Sounart and Baygents (2001; 2007), who studied the transport of a sample plug with significantly higher conductivity than the bulk fluid, and Ren and Li (2004), who numerically studied the effects of conductivity gradients in the process of sample injection. Perhaps, the most interesting works made in this context are recent studies on the electrokinetic stability in the presence of conductivity gradients perpendicular to the direction of movement of bulk liquid by Santiago group at Stanford University. One interesting work is the application of these instabilities to enhance mixing process in microchannels (Oddy et al., 2001). Also, Posner and Santiago (2006) presented a comprehensive analysis on these phenomena by a parametric experimental study of convective electrokinetic instabilities in microchannels. Craven et al. (2008) studied the influence of transverse conductivity gradients on the slip boundary conditions for electroosmotic flow.

In general, flow of liquid-based microfluidic systems tends to be strongly laminar and therefore, lacks of substantial advection nor turbulent components (with the notable exception of the already mentioned electrokinetic instability). Thus, mixing species tends to be diffusion-based and require either a long residence time or long channel length. Numerical simulations on mixing improvement consist in another wide field of applications of numerical simulations (Glasgow et al., 2004). Erickson and Li (2002) demonstrated the use of numeric characterization of heterogeneity of the base surface electrokinetic micromixing by examining the implementation of a series of heterogeneous surface patterns (Figure 2.4). Jen et al. (2003) developed an interesting twisted microchannel geometry to induce advective mixing in T-shaped microfluidic systems simulated using CFD-ACE package (see also Chen and Cho (2008)). Wang et al. (2003) used the MemCFD package of Coventor to model pressure driven mixing in a microfluidic system with patterned grooves. Recently, Miranda et al. (2010) perform numerical simulations by using Fluent to study micromixing in alternating flows and obstacles. Jain and Nandakumar

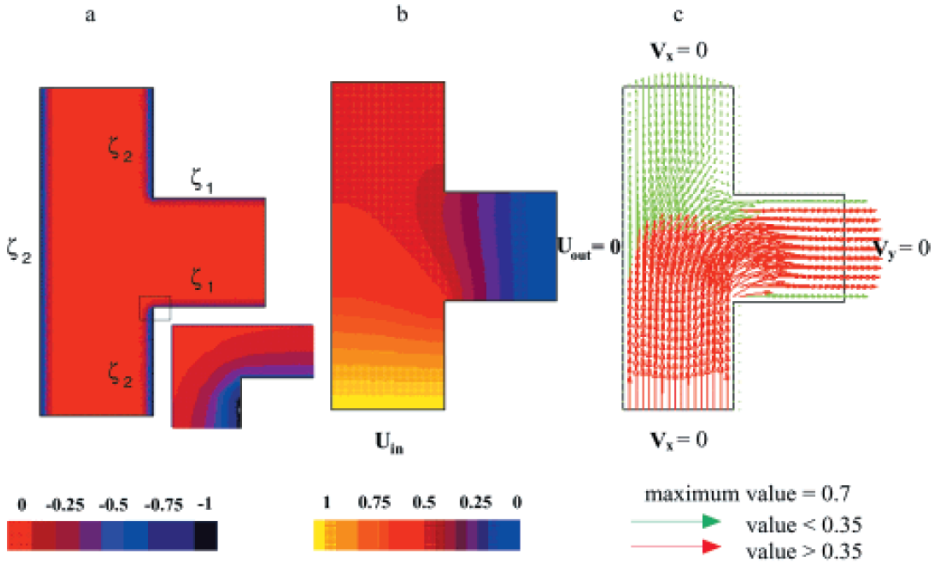

Figure 2.3: Electric potential and velocity profiles in a T-junction from the pioneer work of Bianchi et al. (2000).Reproduced with permission © 2000 ACS publications.

(2010) proposed a novel index for numerical comparative analysis of micromixers. Recently, the use of AC electrokinetics or induced charge electroosmotic flow (ICEF) has given rise to new kind of micromixers (Zhang et al., 2006), for example, the work of Wu and Li (2008) that presents numerical simulations and experiments in micromixing by using ICEF.

2.2.2 On chip reactions

Although fluid mechanics and transport are very important aspects, taking into account what LOC developers are actually requiring to design real LOC, the already mentioned numerical studies are just a part of the whole process. Actually, in order to simulate analytical processes, it is mandatory, to include reactive models, an aspect that has not been extensively explored. These reactive models comprise several kinds of kinetics, such as acid-base reactions, DNA hybridization, enzymatic reactions or immunological reactions, among others. These reactions can be performed in solution (homogeneous) or by immobilizing reactants to microreactor walls (heterogeneous).

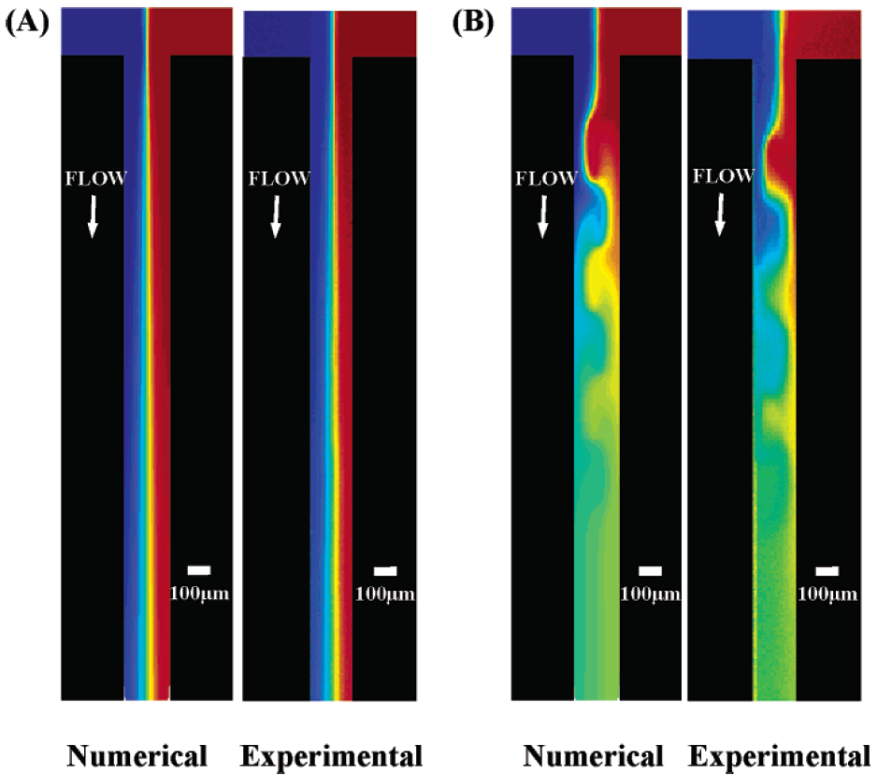

Figure 2.4: Sample concentration distribution for homogeneous (left) and heterogeneous (right) ζ-potential distribution from the work of Erickson and Li (2002). Reproduced with permission, © 2000 ACS publications.

Homogeneous reactions that occur in the bulk fluid are the most common encountered in LOC. In order to carry out efficient homogeneous reactions some parameters have to be precisely controlled, such as the residence time or the reagent injection velocity. Arnaud et al. (2002) presented a detailed dynamic reaction model for acid-base reactions on chip gel-buffering electrophoresis. Debusschere et al. (2003) developed a strong coupled model in 2-D for species transport and reactions. The model includes buffer electrochemistry and variable surface ζ-potential based on empirical data. Simulations demonstrated the reaction of protein labeling. Baroud et al. (2003) presented a numerical solution for the binding of Ca^{2+} with Ca-green marker in a T-channel, including an experimental validation. MacInnes (2002)

simulates the electrokinetic flow and pressure driven flow in a T-junction and applies its results to model reactivity between two streams. The flow model used was described in a later article (MacInnes et al., 2003). Hatch et al. (2001) used a numerical model to predict the performance for diffusion immunoassay based on a T-sensor. Atalay et al. (2009) present the modelling and optimization of a multienzyme reaction scheme on a chip for simultaneous detection of sugars.

Heterogeneous reactions comprise those reactions that occur in the presence of a surface or interface. Such reactions are widely exploited in LOC through either surface or bead-based being the most popular DNA hybridization or antigen antibody binding reactions. Erickson et al. (2003) presented a theoretical and computational model of heterogeneous DNA hybridization kinetics of thermally resolved biochips, which combined two hybridization mechanisms. Hu et al. (2007) performed modelling and simulation of antigen-antibody binding kinetics in a microfluidic chip for electroosmotic and pressure-driven flow, and different conditions on surface concentrations.

2.3 Computer Simulations of entire devices

Numerical simulations of analytical processes carried out on LOC represent a challenging problem from the computational point of view due to the reasons listed in section 2.2. In addition to the aforementioned, when calculation domains are entire chips, and the number of substances significantly involved in reactions (buffer and sample components) increases, the computational cost magnifies. In order to face this magnification, parallel platforms are really suitable to perform calculations employing computation times that are compatible with designing process.

Also, multiple nonlinear problems due to the complex multiphysics nature of the problem, and ill-conditioned global matrices due to the high aspect ratios and high local gradients in different fields, determines another kind of challenges that need to be solved with advanced preconditioning techniques

such as multigrid algorithms or domain decomposition techniques.

All modelling and simulations techniques listed above allowed certain groups to develop comprehensive models for simulate entire LOC. These simulations gather several aspects addressed by reviewed works, including fluid flow computations, electric potential calculations, transport and reactions. Chatterjee (2003) developed a 3D finite volume model to study several applications in microfluidics. This work include thermal calculations, but lack of more general reaction schemes. Cui et al. (2007) presented a complete 2-D model to simulate isotachophoresis in networked microfluidic chip. Barz (2009) developed a fully-coupled model for electrokinetic flow and migration in microfluidic devices employing 2D FEM. In this thesis simulations of CZE by considering entire LOC geometry, even the reservoirs were performed and are shown in section 5.2.1.

Due to the high computational cost that requires simulations of entire chips, parallel computation for these applications is mandatory. With a few exceptions, available commercial software still lacks on distributed memory parallel platforms or suitable preconditioners to carry out these tasks. Due to this situation, parallel computations in simulations of electrokinetic flow and transport in LOC have not been extensively explored. Tsai et al. (2005) presented a 2D parallel finite volume scheme to solve EOF in L-shaped microchannels. 3D simulations of electrophoretic processes employing parallel calculations were performed by Chau et al. (2008) for FFE using finite difference method.

These simulations are carried out without considering weak electrolytes, and in consequence, no reaction processes are simulated. Finally, during this thesis, parallel simulations of LOC, performing complex electrophoretic separations were developed. For these simulations weak electrolytes, coupling between wall electrical properties and bulk chemical composition and a generalized reaction scheme were taken into account. Results of these original contributions are presented in chapter 5.

Chapter 3

Mathematical Modelling

As it was discussed in previous chapters, modelling and simulation of phenomena that occur in LOC are not trivial issues due to their multiphysics and multiscale characteristics. The several physicochemical fields involved and the special considerations required due to the high aspect ratios between length scales involved, determine the complexity on modelling and the related computational cost. The aim of this chapter is to describe how these difficulties were faced, in order to achieve a set of partial differential equations that models analytical processes in LOC.

Most bioanalytical process carried out in LOC are usually performed in liquid phase. When electrolyte solutions get into contact with solid surface, the electric double layer (EDL) takes place, and its effects are quite significant at the microscale. Due to this situation, this chapter begins with the theoretical background about the EDL and the electrokinetic phenomena. Then, section 5.1.2 describes the mathematical modelling of the phenomena involved in electrophoretic separations carried out in LOC. These phenomena include electric, flow, and concentration fields and reaction kinetics for different assays.

3.1 Theory of electric double layer and electrokinetic phenomena

Due the high surface to volume ratio of microchannels, phenomena related to surface charge on the walls in contact with electrolyte solutions are of great importance. Surface charge is caused by the dissociation of surface groups and by non-specific adsorption of ions presents in the solution (Hunter, 2001). Depending on the physicochemical properties (pH, ionic strength) of the solution, the solid wall will have either a positive or a negative surface charge density. A typical value of high charge density and fully ionized surfaces is approximately 0.3 Cm^2, which corresponds to around two elemental charges per square nanometer.

3.1.1 The electric double layer

Due to the electrostatic force, and in order to maintain the electroneutrality of the interface, an oppositely charged region of ions (counterions) develops in the surrounding liquid in order to balance the fixed surface charge at the solid interface. This screening region is denoted as the Electric Double Layer (EDL) because ideally it consists of counterions, some of which are fixed while others are mobile. The EDL was initially represented by a simple capacitor model, which is traditionally attributed to Helmholtz (1879). Gouy and Chapman proposed one layer of charge spread uniformly over a planar surface immersed in an electrolyte solution (Overbeek, 1952).

The assumptions that the electrolyte ions could be regarded as point charges, and the solvent could be treated as a structureless continuum dielectric of constant permittivity, were questioned by Stern (1924). He introduced the concept of a layer between the inner and outer Helmholtz planes, in which the electric charge and potential distributions are assumed to be linear (the so-called Stern layer), and a diffuse layer further away from the wall, where the Gouy-Chapman theory is applied. This model is presented in Figure 3.1, which is separated into three layers (Hunter, 2001; Schoch et al., 2008). The

first layer is at the inner Helmholtz plane and fits the electric potential ψ_0, where co-ions and counterions are not hydrated and are specifically adsorbed to the surface. The second layer is defined by the outer Helmholtz plane with potential ψ_d, that consists in a layer of bound, hydrated, and partially hydrated counterions. Finally, the outermost and third layer is the diffuse layer, composed of mobile co-ions and counterions, in which resides the slip plane bearing the ζ-potential (described hereafter). In most cases, the outer Helmholtz plane and the slip plane are situated close to each other, allowing the approximation of ψ_d with the ζ-potential for practical purposes.

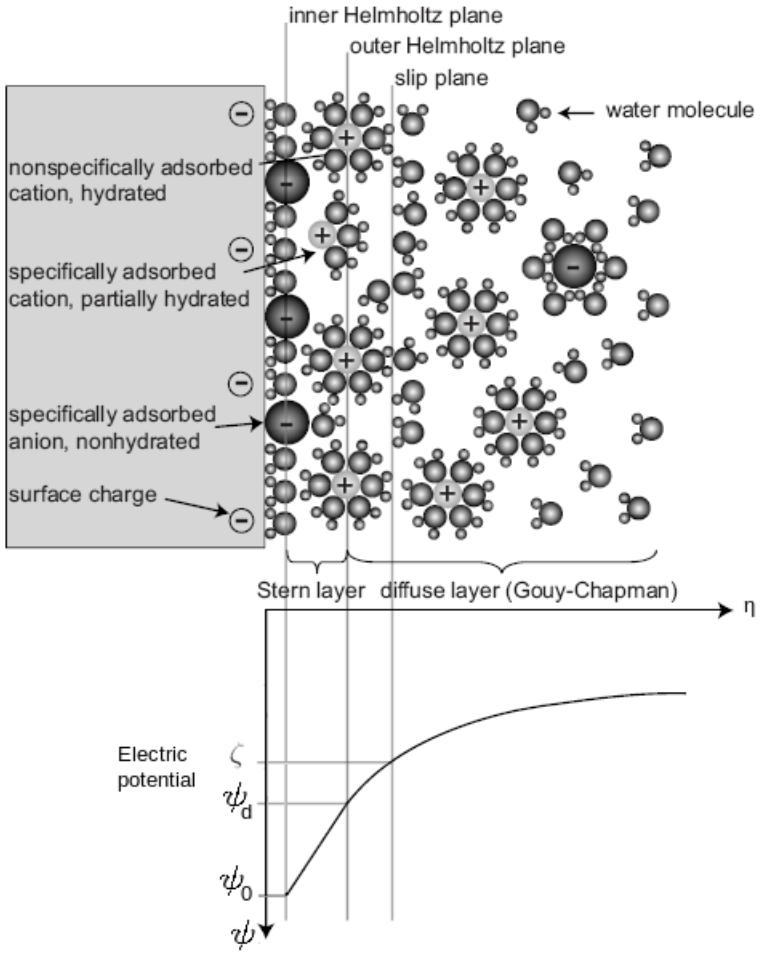

Figure 3.1: The Diffuse Double Layer and the Debye Length.

The slip plane, or shear surface, is an imaginary plane separating ions that are immobile near the surface, from those that are mobile in solution. The ζ-potential at this plane can be experimentally determined, and is therefore an important parameter in LOC for describing fluid flow. The ζ-potential is dependent on the pH and ionic strength of the solution, showing a slight increase in its absolute value for a decreasing number of ions in solution. More details about the ζ-potential dependence will be given in section 3.2.3.

Electric potential distribution at the EDL

In order to calculate the ion distributions at the EDL, the electrochemical potential $\tilde{\tilde{\mu}}_j$ of ion j, in a liquid phase at constant pressure and temperature could be considered as a start point (Probstein, 2003),

$$\tilde{\tilde{\mu}}_j = \tilde{\mu}_j + z_j F\psi = \tilde{\mu}_j^0 + RT\ln(\gamma_a c_j/c^0) + z_j F\psi \tag{3.1}$$

where $\tilde{\mu}_j$ is the chemical potential, z_j is the valence of ion, F is the Faraday constant, ψ is the electric potential due to the surface charge, $\tilde{\mu}_j^0$ is the standard chemical potential of ion j at constant pressure and temperature, R is the universal gas constant, T is the temperature, γ_a is the activity coefficient, c_j is the molar concentration of ion j , and c^0 is the standard molarity of 1 mol m^{-3}. At equilibrium, the electrochemical potential of the ions must be the same in the whole domain, and the electrical and diffusional forces on the ion j must be balanced. Expressing this balance as an equation, and also using Eq. 3.1, the following expression is obtained

$$\nabla\tilde{\mu}_j = -z_j F\nabla\psi = \nabla(\tilde{\mu}_j^0 + RT\ln(\gamma_a c_j/c^0)). \tag{3.2}$$

Integrating the RHS of Eq. 3.2 from a point in the bulk solution where $\psi = 0$ and the local concentration is equal to the bulk concentration ($c_j = c_j^\infty$), leads to the Boltzmann equation, giving the local concentration of each j type

ion in the diffuse layer (Probstein, 2003),

$$c_j = c_j^{\infty}\ e^{-z_j F\psi/(RT)}. \tag{3.3}$$

The volume charge density ρ_e for all ions present in the neighborhood of the surface is given by

$$\rho_e = F\sum_{j=1}^{N} c_j z_j. \tag{3.4}$$

In addition, the Poisson equation relates the charge density and the electric potential as follows

$$\nabla^2\psi = -\frac{\rho_e}{\epsilon_0\epsilon_r} \tag{3.5}$$

where ϵ_0 and ϵ_r are the vacuum and relative permittivity, respectively. By combining Eqs. 3.3, 3.4 and 3.5, the complete Poisson-Boltzmann equation is obtained. This equation describes how the electric potential due to a surface charge interacting with an electrolyte solution varies in space,

$$\nabla^2\psi = -\frac{F}{\epsilon_0\epsilon_r}\sum_{j=1}^{N} c_j^{\infty} z_j e^{-z_j F\psi/(RT)}\ . \tag{3.6}$$

For symmetrical and monovalent electrolytes, Eq. 3.6 can be written in a more custom form as,

$$\nabla^2\psi = \frac{2F\ c^{\infty}}{\epsilon_0\epsilon_r}\sinh\left(\frac{F\psi}{RT}\right). \tag{3.7}$$

The Debye-Hückel approximation

The Poisson-Boltzmann equation (Eq. 3.6 or 3.7) is a non-linear second-order elliptic partial differential equation, and can be solved in simple domains analytically, under the assumption that the surface potential is small ($z_j F\psi \ll RT$, regarding that $RT/F = 25.7\ mV$ at 25 $^\circ C$). In this way, in order to solve Poisson-Boltzmann equation, a linearization of the exponential term is required, this is achieved by using the relationship $e^{-\alpha} \approx 1 - \alpha$, for small α, which leads to the Debye-Hückel approximation

$$\nabla^2\psi = \frac{\psi}{{\lambda_D}^2} \tag{3.8}$$

were λ_D is the Debye length and represents the distance from the wall for normal decay ($1/e$) in the electric potential, and is determined as,

$$\lambda_D = \left(\frac{\epsilon_0 \epsilon_r\ RT}{F^2 \sum_{i=1}^{N} c_j^{\infty} {z_j}^2} \right)^{\frac{1}{2}} . \tag{3.9}$$

For a symmetrical electrolyte at 25 $^\circ C$, the value of the Debye length can be written as

$$\lambda_D = \frac{9.61 \times 10^{-9}}{{I_s}^{\frac{1}{2}}} \tag{3.10}$$

where the value of λ_D is in m, and I_s is the ionic strength defined as,

$$I_s = \frac{1}{2} \sum_{j=1}^{N} c_j {z_j}^2 \ . \tag{3.11}$$

This equations provides a quick estimation of λ_D, for example, for a solution with a molar concentration of 10^{-4} mol m^{-3} the Debye length is about 1 nm. Based on the approximation of $z_j\psi_s < 25.7\ mV$, the solution of the Debye-Hückel approximation is

$$\psi(x) = \psi_0 e^{(-\frac{\eta}{\lambda_D})}. \tag{3.12}$$

where η is the normal coordinate relative to the wall surface.

3.1.2 The electrokinetic phenomena

The topics discussed above are crucial to understand the electrokinetic phenomena. These phenomena arises when the mobile portion of the diffuse region of the EDL and an electric field interact in the viscous shear plane (Probstein, 2003). Due to the aforementioned net charge present in the EDL, the electric field will exert a force on these charges. In the diffuse layer, these charges, as a part of the electrolyte solution, will migrate carrying solvent molecules with them and causing fluid flow. Conversely, an electric field will be created if the charged surface and the diffuse region of the EDL are forced to move relatively each other in the tangential direction. Then, the four electrokinetic phenomena following the description of Shaw and Williams (1968) are:

- Electroosmosis: is the movement of liquid relative to a stationary charged surface by an applied electric field in the tangential direction.
- Electrophoresis: is the movement of a charged surface relative to stationary liquid by an applied electric field.
- Streaming potential: is the difference on electric potential created when liquid is forced to flow along a stationary charged surface (the opposite to electroosmosis).
- Sedimentation potential: is the difference on electric potential created when charged particles move relatively to a stationary phase (the opposite to electrophoresis).

Both electroosmosis and streaming potential are related to the motion of electrolyte solutions including non-charged solvent molecules. Electrophoresis and sedimentation potential are specially devoted to charged molecules present in the solution.

Electroosmosis

Electroosmosis or electroosmotic flow (EOF) was observed for the first time by Reuss (1809), who report that the application of an electric field caused the displacement of water through a porous clay diaphragm toward the cathode. If the surface is negatively charged, the net excess of positive ions in the EDL will draw the liquid along because of viscous interactions, which results in a net fluid flow toward the cathode. At the Stern plane, the liquid velocity is zero and it increases to a maximum value, $\mathbf{u}_{eo}$, towards the center of the channel. At some distance from the wall, velocity remains constant depending on the ratio between the Debye length and the transverse dimension of the channel. This plug-like flow was first described by Smoluchowski (1918), and the value of the electroosmotic velocity is

$$\mathbf{u}_{eo} = -\frac{\epsilon_0 \epsilon_r \zeta_w \mathbf{E}}{\mu} \tag{3.13}$$

where $\mathbf{E}$ is the externally applied electric field, ζ_w is the electrokinetic potential of the channel wall, and μ is the dynamic (shear) viscosity of the fluid.

Electroosmotic flow has been used in LOC for a wide range of applications (Reyes et al., 2002) due to the several advantages that presents in comparison to pressure driven flow. These advantages include the absence of mechanical moving parts, which increases lifetime and portability, and minimization of sample dispersion due to the plug flow among others. Last advantage can be observed in Fig. 3.2, where the dispersion of a fluorescent marker is shown, and it is clearly lower for the case of EOF pumping than for pressure driven (Whitesides and Stroock, 2001). Several applications of electroosmotic flow will be shown in chapter 5.

Electrophoresis

Electrophoresis is used as a common technique to move or separate ions and molecules in microfluidic and nanofluidic channels. As it was defined above,

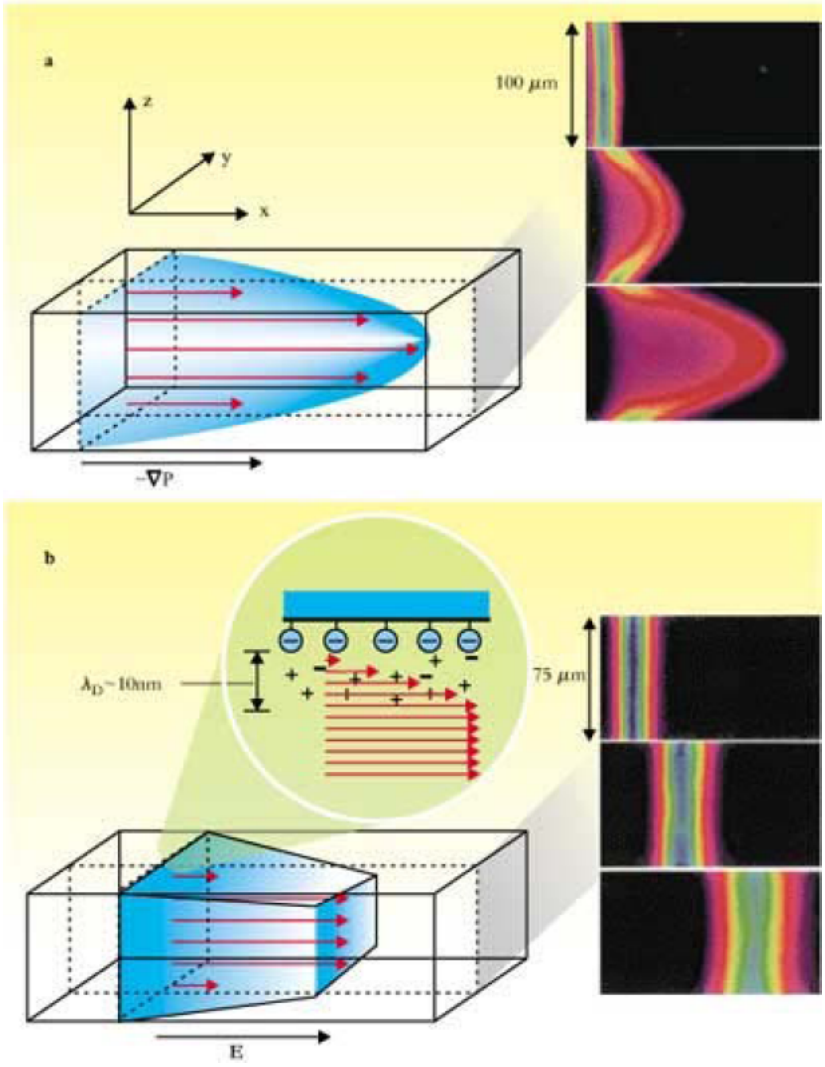

Figure 3.2: Flow profiles and fluorescent marker dispersion in microchannels. In **a)** the flow is driven by pressure, and in **b)** is driven by EOF. Reproduced with permission from Whitesides and Stroock (2001) © 2001 AIP.

electrophoresis is the movement of charged particles (in general, molecules in solution) relative to stationary liquid phase by an applied electric field. When a molecule is placed in an aqueous medium, the EDL surrounding the molecule screens its charges. Applying an electric field results in the movement of the molecule because ions in the EDL are not fixed to the surface. Therefore, the electrophoretic mobility is dependent on the thickness of the electrical double layer and can be divided into two categories depending on the ratio between the molecule main dimension a_p and the Debye length λ_D.

Thin electrical double layer

When $a_p/\lambda_D \gg 1$, the EDL is thin compared to the molecular radius, electrophoresis is the converse of electroosmosis and the effects are similar to those described above in Eq. 3.13. Here, the electrophoretic mobility Ω, is defined as the ratio between the magnitudes of electrophoretic velocity $\mathbf{v_{ep}}$ and the applied electric field. In this case, the surface moves relative to the stationary fluid, and Ω is given by the Helmholtz-Smoluchowski limit

$$\Omega = \frac{\epsilon_0 \epsilon_r \zeta_m}{\mu}. \tag{3.14}$$

where ζ_m is the electrokinetic potential of the molecule.

Thick electrical double layer

When $a_p/\lambda_D \ll 1$, the molecule has a thick EDL, and the force acting over it, is the difference between the drag and Coulomb forces (qE_x). The drag force is given by Stokes law, equating the forces lead to

$$qE_x = 6\pi\mu v_{ep} a_p \tag{3.15}$$

where q is the net charge, and is defined by (Probstein, 2003)

$$q = 4\pi a_p \epsilon_0 \epsilon_r \zeta_m (1 + a_p/\lambda_D) \tag{3.16}$$

where the ζ_m potential can be identified with the potential of the spherical charged surface. Finally, the combination of Eqs. 3.15 and 3.16, and the previous definition of electrophoretic mobility, leads to the Hückel-Onsager limit,

$$\Omega = \frac{2\epsilon_0\epsilon_r\zeta_m}{3\mu}(1 + a_p/\lambda_D). \tag{3.17}$$

The real situation is more complex than that described above, as co-ions around the molecule move ahead and counterions move in the direction opposite to the molecule. This results in a polarization field, which can increase or decrease the electrophoretic mobility. A second issue, which has not been considered, is the distortion of the field induced by movement of the molecule, known as the relaxation effect (Probstein, 2003).

3.2 Modelling

This section describes the mathematical model for electrophoretic separations in LOC. The model includes the fluid dynamics, electric field, mass transport, chemical reactions, and the coupling between all of these fields. First the fluid mechanics modelling is discussed, then different approaches for the electric field calculations are presented, and the influence of physicochemical properties of the solution on channels wall is included. After that, mass transport equation and different reactions kinetics are discussed.

Isothermal conditions are assumed throughout this work. It is known that an important effect associated with electric current in microchannels is temperature rising due to internal heat generation, namely Joule effect (Li, 2004). Nevertheless, if the applied electric field is relatively low, and the microfluidic chip is able to reject the heat to the environment, the fluid temperature does not change appreciably (MacInnes et al., 2003; Berli, 2008).

3.2.1 Flow field

In the framework of continuum fluid mechanics, fluid velocity u and pressure p are governed by the following equations (Probstein, 2003; Li, 2004):

$$-\nabla \cdot \mathbf{u} = 0, \tag{3.18}$$

$$\rho\left(\frac{\partial \mathbf{u}}{\partial t} + \mathbf{u}\cdot\nabla\mathbf{u}\right) = \nabla\cdot(-p\mathbf{I} + \mu(\nabla\mathbf{u} + \nabla\mathbf{u}^T)) + \rho\mathbf{g} + \rho_e\mathbf{E}\ . \tag{3.19}$$

Equation 3.18 expresses the conservation of mass for incompressible fluids. Equation 3.19 expresses the conservation of momentum for Newtonian fluids of density ρ, viscosity μ, subjected to gravitational field of acceleration $\mathbf{g}$ and electric field strength $\mathbf{E}$. The last term on the right hand side of Eq. 3.19 represents the contribution of electrical forces to the momentum balance, where $\rho_e = F\sum_j z_j c_j$ is the electric charge density of the electrolyte solution, obtained as the summation over all type-j ions, with valence z_j and concentration c_j, and F is the Faraday constant.

Due to the low values of the Reynolds number that flows present in microchannels (usually less than 50), the inertial terms present in the Navier - Stokes equations can be neglected where flow is fully developed (Santiago, 2001). However, in certain situations, the inertial effects have to be taken into account in order to obtain correct simulation results. These situations include: end effects (Yang et al., 2005), sudden expansions or section changes (Tsai et al., 2007), changes on velocity direction (Yang et al., 2001; Craven et al., 2008), high conductivity gradients on the solution (Posner and Santiago, 2006) and non-uniform wall ζ-potential (Herr et al., 2000). It is important to consider all these situations in order to obtain a generalized model of flow in microchannels, due to this, the inertial terms were included in the model.

3.2.2 Electric field

The relationship between electric field and charge distributions in the fluid of permittivity ϵ is given by

$$\epsilon\nabla\cdot\mathbf{E} = \rho_e. \tag{3.20}$$

Modelling electrophoresis problems demands special considerations on the electric field, since it involves different contributions in the flow domain, and is strongly affected by the presence of non-uniform electrolyte concentrations. Here we describe the computation of the electric field, as well the hypothesis included to simplify numerical calculations. For this purpose, a (η, τ) wall-fitted coordinate system is used, where η and τ are, respectively, the coordinates normal and tangent to the solid boundaries.

The first contribution to the electric field comes from the presence of electrostatic charges at solid-liquid interfaces. The interfacial charge has associated an electric potential ψ that decreases steeply in η-direction due to the screening produced by counterions and other electrolyte ions in solution, as was discussed in the previous section. The value of ψ at the plane of shear is the electrokinetic potential ζ. Also in this modelling, ζ is allowed to vary smoothly along the τ-direction (see below Section 3.2.3) on a length scale L around 1 cm. Nevertheless, since $\zeta/\lambda_D >> \zeta/L$, the variation of ψ with τ is disregarded and ψ is assumed to vary with η only.

There is also a potential ϕ in the flow domain, which comes from the potential difference $\Delta\phi$ externally applied to drive electrophoresis and/or induce EOF. As the channel walls are supposed perfectly isolating, there are no components of the applied field normal to the wall, and ϕ varies in τ-direction only. Therefore the total electric potential may be written as

$$\Phi(\eta, \tau) = \psi(\eta) + \phi(\tau). \tag{3.21}$$

This superposition is valid if the EDL retains its equilibrium charge distribution when the electrolyte solution flows. The approximation is part of the standard electrokinetic model (Hunter, 2001) and holds if the applied electric field ($\sim \Delta\phi/L$) is small in comparison with the EDL electric field ($\sim \zeta/\lambda_D$), which is normally the case encountered in practice. Introducing the electric field $\mathbf{E} = -\nabla\Phi$ into Eq. 3.20 leads to the following expression,

$$\frac{\partial^2\psi}{\partial\eta^2} + \frac{\partial^2\phi}{\partial\tau^2} = -\frac{\rho_e}{\epsilon}. \tag{3.22}$$

The second term on the left hand side of Eq. 3.22 is non-null in electrophoresis problems because the presence of concentration gradients in the fluid induces a variation of $\frac{\partial \phi}{\partial \tau}$ along the channel. However, $\frac{\partial^2 \phi}{\partial \tau^2}$ is several orders of magnitude lower than $\frac{\partial^2 \psi}{\partial \eta^2}$ (see also MacInnes (2002); Sounart and Baygents (2007); Craven et al. (2008); Barz (2009)), which allows one to split the computation of the electric field in two parts, as explained below.

Electric double layer

According to the previous analysis, the EDL potential is governed by

$$\frac{\partial^2 \psi}{\partial \eta^2} = -\frac{\rho_e}{\epsilon}. \tag{3.23}$$

Introducing the ion concentrations c_j in the form of Boltzmann-type distributions yields Poisson-Boltzmann model of the diffuse layer, which enables the calculation of $\psi(\eta)$. This solution is useful to compute the EOF in nanochannels, or in microchannels with complicated geometries, such as sharp corners (for example, see section 5.3). This equations is not suitable for numerical resolution for the same reasons that were discussed for Eq. 3.6, and ρ_e can be calculated as

$$\rho_e = 2F\ c^{\infty} \sinh\left(\frac{F\psi}{RT}\right). \tag{3.24}$$

This last equation were taken into account for some particular cases and was also numerically implemented in the present thesis. Its application is presented in section 5.3.

Nevertheless, computational requirements are very large when a whole chip is modelled. In this sense, and considering that the present work focuses on electrophoretic processes on LOC, here we simplify the calculation of the EOF by introducing the so-called thin EDL approximation (Brunet and Adjari, 2004; Berli, 2008): electro-osmosis is regarded as an electrically induced slip velocity in the direction of the applied electric field, the magnitude of which is given by Helmholtz-Smoluchowski equation (Eq. 3.13).

This approximation also implies that $\rho_e \approx 0$ in the fluid outside the EDL, meaning that the last term on the right-hand side of Eq. 3.19 is negligible. Thus the electro-osmotic velocity enters the hydrodynamic field as a boundary condition, which significantly reduces computational demands. The simplification is appropriate taking into account that $\lambda_D \approx 1 - 10\ nm$, while cross-sectional channel dimensions are $10 - 100\ \mu m$.

Bulk fluid

Given the considerations made above, the electric potential $\phi(\tau)$ has to be calculated from the charge conservation equation in steady state (Probstein, 2003):

$$\nabla \cdot \left(-\sigma \nabla \phi - F \sum_{j=1}^{N} z_j D_j \nabla c_j + \rho_e \mathbf{u} \right) = 0 \tag{3.25}$$

where D_j is the diffusion coefficient, and σ is the electrical conductivity of the electrolyte solution, given by:

$$\sigma = F \sum_{j=1}^{N} {z_j}^2 \Omega_j c_j \tag{3.26}$$

where Ω_j is the ionic mobility. In fact, the terms between brackets in Eq. 3.25 constitute the electric current density i, which accounts for the ion fluxes due to fluid convection, electrical forces, and Brownian diffusion. Finally one may note that Eq. 3.25 reduces to $\frac{\partial^2 \phi}{\partial \tau^2} = 0$ (Laplace equation for the applied potential) only if electrolyte concentrations and mobilities are perfectly uniform and stagnant.

3.2.3 Electrokinetic potential

In a typical IEF or ITP assay the pH changes several units along the channel, which induces a parallel variation of ζ, provided the interfacial charge has not been fully suppressed. In order to account for the influence of this variation

on the EOF, here we include a model of ζ in terms of the pH and the ionic strength.

The electrokinetic potential at the solid-fluid interface depends on the charge generation mechanism of the surface (Hunter, 2001). In principle, it may be thought that solid walls expose toward the fluid a certain number of specific sites (n_S) able to release or take H^+ ions, with a dissociation constant K_S. In equilibrium with an aqueous electrolyte solution, the surface becomes electrically charged. For the case of interfaces containing weak acid groups, such as silanol in fused silica capillaries and carboxyl in synthetic polymer materials, the following relationship is appropriate for symmetric monovalent electrolytes (Berli et al., 2003):

$$\sqrt{8\epsilon RTI}\sinh\left(\frac{zF\zeta}{2RT}\right) = \frac{-en_s}{1+10^{(pK_S-pH)}e^{-F\zeta/(RT)}}. \tag{3.27}$$

Therefore, if the parameters that characterize the interface are known (n_S, K_S), the ζ-potential can be readily predicted for different values of pH and I (Fig. 3.3). Then the electro-osmotic velocity is directly coupled to the electrolyte composition. Empirical formulae of $\zeta(pH, I)$ were also reported in order to simplify calculations (Kirby and Hasselbrink, 2004).

3.2.4 Mass transport and chemistry

The mass transport of weakly concentrated sample molecules and buffer electrolyte constituents can be modelled by a linear superposition of migrative, convective and diffusive transport mechanisms, plus a source term due to chemical reactions. In a non-stationary mode, the concentration of each j-type species, is governed by (Probstein, 2003):

$$\frac{\partial c_j}{\partial t} + \nabla\cdot(-z_j\Omega_j\nabla\phi c_j + \mathbf{u}c_j - D_j\nabla c_j) - r_j = 0 \tag{3.28}$$

were r_j is the reaction term. Different electrolytes (acids, bases and ampholytes), analytes, and particularly the hydrogen ion have to be considered.

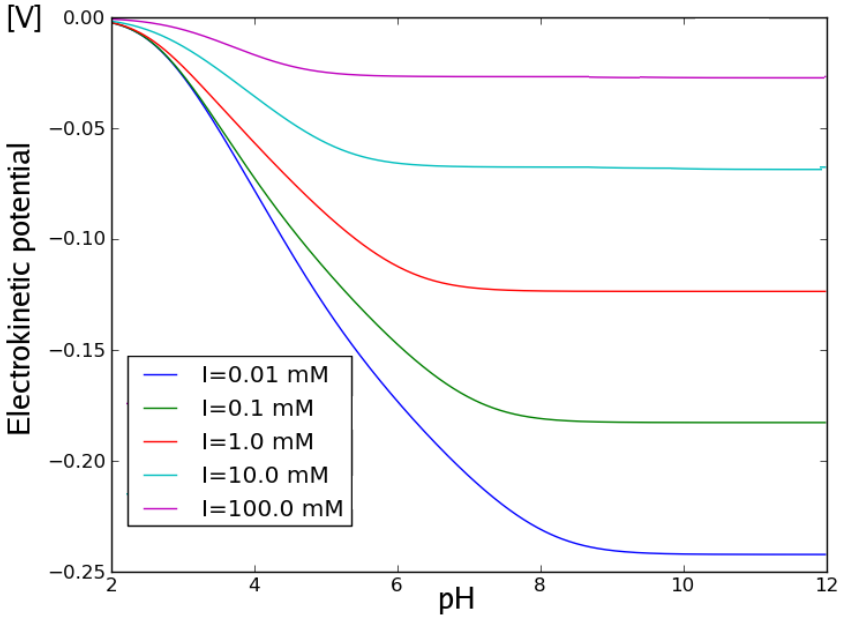

Figure 3.3: Electrokinetic potential (ζ-potential) as a function of pH for different ionic strength. Characteristics parameters for the surface were taken from Berli et al. (2003) for vitreous capillaries ($pK_s = 3.51$ and $ns = 1.27 \times 10^{17}$ m^{-2}).

In electrolyte chemistry the processes of association and dissociation are much faster than the transport electrokinetic processes, hence, it is a good approximation to adopt chemical equilibrium constants to model the reactions of weak electrolytes (Arnaud et al., 2002), while strong electrolytes are considered as completely dissociated.

Acid-base reactions

For the general case, reactions associated to an ampholyte AH are

$$\mathrm{AH} \underset{k_{a2}}{\overset{k_{a1}}{\rightleftharpoons}} \mathrm{A^-} + \mathrm{H^+} \tag{3.29}$$

$$\mathrm{AH_2^+} \underset{k_{b2}}{\overset{k_{b1}}{\rightleftharpoons}} \mathrm{AH} + \mathrm{H^+} \tag{3.30}$$

where k_{a1}, k_{b1} are the dissociation rates, and k_{a2}, k_{b2} are the association rates for the acidic and basic reactions respectively. Then the equilibrium state is characterized by,

$$\frac{k_{a2}}{k_{a1}} = \frac{[\mathrm{A}^-][\mathrm{H}^+]}{[\mathrm{AH}]} = K_a \tag{3.31}$$

$$\frac{k_{b2}}{k_{b1}} = \frac{[\mathrm{AH}][\mathrm{H}^+]}{[\mathrm{AH}_2^+]} = K_b \tag{3.32}$$

where K_a and K_b are the equilibrium constants, for the acidic and basic reactions respectively, and the square brackets represent concentration in mol m^{-3}, of the given specie. The corresponding expressions of r_j are obtained as follows,

$$r_{\mathrm{A}^-} = -k_{a1}[\mathrm{A}^-][\mathrm{H}^+] + k_{a2}[\mathrm{AH}] \tag{3.33}$$

$$r_{\mathrm{AH}} = k_{a1}[\mathrm{A}^-][\mathrm{H}^+] - k_{a2}[\mathrm{AH}] - k_{b1}[\mathrm{AH}][\mathrm{H}^+] + k_{b2}[\mathrm{AH}_2^+] \tag{3.34}$$

$$r_{\mathrm{AH}_2^+} = k_{b1}[\mathrm{AH}][\mathrm{H}^+] - k_{b2}[\mathrm{AH}_2^+] \tag{3.35}$$

$$r_{\mathrm{H}^+} = -k_{a1}[\mathrm{A}^-][\mathrm{H}^+] + k_{a2}[\mathrm{AH}] - k_{b1}[\mathrm{AH}][\mathrm{H}^+] + k_{b2}[\mathrm{AH}_2^+]. \tag{3.36}$$

In Eq. 3.36 the water dissociation term is not included due to the fact that this reaction is several orders of magnitude faster than reactions 3.29 and 3.30 (Arnaud et al., 2002), then $[OH^-]$ can be calculated directly as

$$[OH^-] = \frac{K_w}{[\mathrm{H}^+]} \tag{3.37}$$

were $K_w = 10^{-14}$ $\mathrm{mol}^2\mathrm{m}^{-6}$, is the dissociation constant for pure water at 25°C.

Effective charge and mobility of analytes

When the concentration of analytes is much lower than that of buffer constituents, its effect on the pH is negligible. In these cases, considering all ionic species represents a high computational cost. However the influence of pH on the analytes must be taking into account. Thus the transport equation of

these analytes includes $r_j = 0$, and the product $z_j\Omega_j$ as a function of pH. For example, if the specie is an ampholyte that obeys a reaction scheme like the one shown in Eqs. 3.29 and 3.30, $z_j\Omega_j$ is included in Eq. 3.28 as an effective charge-mobility product ($z_{eff(j)}\Omega_{eff(j)}$; Chatterjee (2003)). This product is calculated as $(\alpha_0 - \alpha_2)\Omega_j$, where α_0 and α_2 are the degrees of dissociation of anions and cations, respectively, which are written in terms of $[H^+]$ as,

$$\alpha_0 = \frac{\frac{K_a K_b}{[\mathrm{H}^+]^2}}{1 + \frac{K_b}{[\mathrm{H}^+]} + \frac{K_a K_b}{[\mathrm{H}^+]^2}} \tag{3.38}$$

$$\alpha_2 = \frac{1}{1 + \frac{K_b}{[\mathrm{H}^+]} + \frac{K_a K_b}{[\mathrm{H}^+]^2}} \tag{3.39}$$

Therefore the governing equation for concentration of the $j-$specie in the sample plug results,

$$\frac{\partial c_j}{\partial t} + \nabla \cdot [-(\alpha_0 - \alpha_2)\Omega_j \nabla\phi c_j + \mathbf{u}c_j - D_j \nabla c_j] = 0 \tag{3.40}$$

where it is observed that the physical motion of analytes is coupled to the degree of dissociation at a given pH.

Previous works (Chatterjee, 2003; Shim et al., 2007) calculate the pH by using a nonlinear equation based on global electroneutrality, to avoid the inclusion of reactive terms in Eq. 3.28 for hydrogen ion. This equation is

$$[\mathrm{H}^+] - \frac{K_w}{[\mathrm{H}^+]} + \sum_{j=1}^{N} (z_{eff})_j c_j = 0 \tag{3.41}$$

were N is the total amount of ions that can affect the pH condition of the solution.

In parallel computing, solving monolithically two different nonlinear systems is discouraged due to its mathematical complexity (Storti et al., 2009) and computational inefficiency (Cai and Keyes, 2002). Then, in some cases, where

numerical convergence is not critical, the Eq. 3.41 is used to calculate pH. In other cases, the reactive scheme (Eqs. 3.28 to 3.36) is used to solve species that change pH conditions, and the effective mobility scheme ($r_j = 0$ and Eqs. 3.38 to 3.40) for those that cannot affect considerably the pH conditions. This scheme provides better convergence and stability, and does not affect parallel calculations performance. Additionally the reactive scheme allows to treat different kind of assays simulations, as enzymatic process or antigen-antibody systems (described below).

Immunological reactions

In analysis involving immunological reactions (immunoassay), the antigen (Ag) links to the binding sites of the antibody (Ab) to form an antigen-antibody complex (AgAb). The dynamics of this reactions are described in the simplest way, by using a Langmuir reaction scheme and could be limited both by Ag or Ab (Wild, 2005). The reactions are described as

$$Ag + Ab \underset{k_u}{\overset{k_b}{\rightleftharpoons}} AgAb \tag{3.42}$$

where k_b and k_u are the rate constants for binding and unbinding respectively. The reactions terms associated with these phenomena are:

$$r_{Ag} = r_{Ab} = -k_b[Ag][Ab] + k_u[AgAb] \tag{3.43}$$

$$r_{AgAb} = k_b([Ag] - [AgAb])([Ab] - [AgAb]) - k_u[AgAb] \tag{3.44}$$

and it it used both for homogeneous and heterogeneous assays.

Enzymatic reactions

Enzymatic reactions are also commonly used in LOC analysis. The mechanism of enzyme-catalyzed reactions, involving the enzyme (E), substrate (S), and the product (P), can often be described by using the Michaelis - Menten kinetics (Marangoni, 2003). Following this model, the reaction can be described

as

$$E + S \underset{k_{-1}}{\overset{k_1}{\rightleftarrows}} ES \xrightarrow{k_p} P + E \tag{3.45}$$

where ES is the enzyme-substrate complex, k_1 and k_{-1} are the forward and backward rate constants for the formation of the complex ES, and k_p is the kinetic constant for conversion of the ES complex to the product. When the substrate concentration far exceeds that of the enzyme, the rate of product formation can be described by this kinetics. Hatch et al. (2001) show that for microfluidic assays that involve nonuniform analyte concentrations, reactive source terms for substrate and product can be written as

$$r_S = -r_P = -\frac{k_p[E][S]}{K_m + [S]} \tag{3.46}$$

where K_m is the Michaelis constant and is calculated as

$$K_m = \frac{k_{-1} + k_p}{k_1} \tag{3.47}$$

In many cases, several substrates and the products are considered. In these cases, the reaction kinetics is more complex, but could be simplified as (Atalay et al., 2009)

$$\sum_{i=1}^{N_s} S_i \xrightarrow{E} \sum_{j=1}^{N_p} P_j \tag{3.48}$$

where N_s is the number of substrates, N_p the number of products, and the reaction terms for all substrates or products can be computed as follows

$$r_S = -\frac{k_p[E]\prod_i[S_i]}{\prod_i K_{mi} + \sum_i K_{mi}[S_i] + \prod_i[S_i]} \tag{3.49}$$

$$r_P = \frac{k_p[E]\prod_i[S_i]}{\prod_i K_{mi} + \sum_i K_{mi}[S_i] + \prod_i[S_i]} \tag{3.50}$$

where the particular Micaelis constants K_{mi} can be calculated as

$$K_{mi} = \frac{k_{-1i} + k_p}{k_{1i}} \tag{3.51}$$

Chapter 4

Numerical modelling and simulation

The path to obtain useful numerical solutions from the PDEs presented in previous chapter has several stages. This path starts with the selection of the numerical method to discretize equations, the solution of the non-linear and linear equation systems that the discretization generates, and the suitable handling of the obtained data in order to have a suitable presentation of results.

When using numerical methods, different problems arise related to the stability and convergence of the processes involved in obtaining solutions. These problems are related to the order and type of the derivatives that define the PDEs, the physical conditions of the problem (quantified through non-dimensional numbers), and the numerical method itself.

This chapter summarizes the different steps carried out in order to obtain numerical simulations of analytical processes in LOCs, starting from the PDEs listed in previous chapter. Also, special considerations taken into account in order to surmount particular problems related to convergence and stability are presented.

First the methodological core of numerical tools employed, the finite element method, is presented. Also, discrete formulations for the main equations with their stabilization terms are summarized. Then, software tools involved in the programing stage are described. Finally, a simplified guide to reproduce

simulations, simulate new designs or expand the models already developed, is presented.

4.1 The finite element method

The finite element method (FEM) is a numerical technique for finding approximate solutions of partial differential equations (PDE). As many numerical methods, FEM is based on the approximation to the solution of the PDE as a discrete function. Particularly, FEM is based on three basic principles (Zienkiewicz and Morgan, 1983):

- The subdivision of the domain in non-overlapping parts (elements), that could be segments, polygons or polyhedrons depending on the spatial dimensions of the domain Ω, where the unknowns are located primarily at the vertexes of these elements.

- Trial functions used to approximate the solution are locally supported; it means that one particular function is non-zero only inside one particular element

- The equations are solved by minimizing the integral weighted residual, by using as weighting function the same set used for the trial function (Galerkin method).

The finite element method is a suitable tool for solving partial differential equations when geometry domain is complicated or changes during the simulation, when the desired precision varies over the entire domain, or when the solution lacks of smoothness (Johnson, 1987). In chapter 2 were mentioned other numerical methods such as finite differences (FD), finite volume method (FVM) and flux corrected transport (FCT). All simulations in this thesis were performed by using FEM. The choice of FEM is due to the possibility of solving problems in complex domains (as the LOC are) which is not possible by using FD. On the other hand, it is well known that FVM and FCT are more suitable to solve advective dominant problems, whereas FEM is more effective in solving

Figure 4.1: Boris Galerkin (1871-1945).

problems where diffusion prevails (Idelsohn and Oñate, 1994). Problems related with analytical process in LOC, depending on the situation, are advective or diffusive dominant in different levels. However, there are several works including well tested techniques, with consistent mathematical support, devoted to improve FEM performance in advective dominant problems (Donea and Huerta, 2003). Taking into account all these facts, the pre-existence of a parallel high performance computing (HPC) FEM platform as PETSc (Portable Extensible Toolkit for Scientific calculations)-FEM, and the extensive experience in using FEM at the *International Center for Numerical Methods in Engineering* (CIMEC, `http://www.cimec.org.ar/`), FEM was chosen as the appropriate numerical method to develop the proposed simulation tools.

4.1.1 Finite element formulations

In this section, FEM formulations for the more significant equations that have been implemented during this thesis are presented. As it was shown in chapter 3, there are three main components in the modelling and simulation processes, the electric field, the flow field and the mass transport.

Electric potential

During this thesis, four different equations have been employed to calculate the electric potential:

- Poisson equation (Eq. 3.5): this equation is not suitable for numerical implementation in solving problems in 2D or 3D domains (Schoch et al., 2008), due to this, its use was limited to 1D simple test during development and validation stage .
- Poisson - Boltzmann equation (Eq. 3.7): this equation was used for solving problems in the special cases mentioned in section 3.2.2. Solving this equation implies some special numerical considerations near the walls (see Section 5.3).
- Charge conservation equation (Eq. 3.25): this equation was employed in the most of the cases due to its wide range of applications, and its good numerical properties.
- Laplace equation: this equation was used in several cases as a consequence of employing charge conservation equation when conductivity fields are uniform and stagnant.

For the sake of simplicity, only the formulations for Poisson - Boltzmann and charge conservation equations are presented. Formulations for other two equations can be easily inferred from these due to the algebraic similarity.

Poisson - Boltzmann equation

Beginning from the Eq. 3.5, the first step in order to obtain a FEM formulation is to develop the weighted residual form for the equation as follows

$$\begin{aligned} \int_{\Omega^h} (\nabla^2 \psi) v \; d\Omega^h = \int_{\Omega^h} \left(\frac{2F \; c^\infty}{\epsilon_0 \epsilon_r} \sinh\left(\frac{F\psi}{RT}\right)\right) v \; d\Omega^h \text{ in } \Omega^h \\ \psi = \psi_\Gamma \text{ at } \Gamma_D \\ \frac{\partial \psi}{\partial n} = 0 \text{ at } \Gamma_N \end{aligned} \tag{4.1}$$

where v is the weight function and Ω^h is the mathematical domain for the problem with boundary Γ such as, $\Gamma = \Gamma_D \cup \Gamma_N$ and $\Gamma_D \cap \Gamma_N = \emptyset$. Γ_D is the boundary portion where Dirichlet conditions are applied, and, Γ_N where Neumann conditions are imposed. Then, a function space for functions v has to be define. As it is known, for this kind of FEM problem a subspace V_h can be chosen such that

$$v_h \in V_h \subset H^1$$

where, H^1 is the Hilbert functional space such that

$$H^1(\Omega^h) = \{v : \int_{\Omega^h} \| \nabla v \|^2 \ d\Omega^h \ < \infty\},$$

in this thesis, linear elements will be consider and the definition of v_h can be completed as

$$\begin{aligned} v_h \in V_h = \{v_h : \ & v_h \in C^0 \text{ in } \Omega^h, \\ & v_h|_K \in p^1 \ \forall K \in T^h, \\ & v_h = 0 \text{ in } \Gamma\} \end{aligned}$$

where p^1 is the set of first order polynomial functions with real coefficients, and K are the elements of the topological discretization T^h of Ω^h. Then, for this equation the Galerkin method is proposed, and the solution to find also is a function in the space V_h. Finally, we can present the FEM problem as:

find ψ_h, such as $\psi_h, v_h \in V_h$ and

$$\begin{aligned} -\int_{\Omega^h} \nabla\psi_h \cdot \nabla v_h \ d\Omega^h = & \frac{2F \ c^\infty}{\epsilon_0 \epsilon_r} \int_{\Omega^h} \sinh\left(\frac{F\psi_h}{RT}\right) v_h \ d\Omega^h \quad \text{in } \Omega^h \\ \psi_h = & \psi_\Gamma \text{ at } \Gamma_D \\ \frac{\partial \psi_h}{\partial n} = & 0 \text{ at } \Gamma_N. \end{aligned} \tag{4.2}$$

where the Green formula and the natural boundary conditions were applied as follows

$$\int_{\Omega^h} (\nabla^2 \psi_h) v_h \; d\Omega^h + \int_{\Omega^h} \nabla \psi_h \cdot \nabla v_h \; d\Omega^h = \int_{\Gamma} v_h (\nabla \psi \cdot \mathbf{n}) \; dS = 0 \tag{4.3}$$

where $\mathbf{n}$ is the outward pointing unit normal of boundary element dS.

Due to its right hand side, the Eq. 4.2 is nonlinear. In order to solve this kind of systems Newton-like methods are required. These are methods for solving systems of nonlinear equations of the form

$$\boldsymbol{F}(\psi) = 0,$$

where $\boldsymbol{F} : \Re^n \rightarrow \Re^n$. Newton-like methods provide the core of the package, including both line search and trust region techniques to ensure global convergence to the solution. The general form of the n-dimensional Newton's method is

$$\psi_{k+1} = \psi_k - [\boldsymbol{F}'(\psi_k)]^{-1} \boldsymbol{F}(\psi_k), \quad k = 0, 1, \ldots,$$

where ψ_0 is an initial approximation to the solution and $\boldsymbol{F}'(\psi_k)$, the Jacobian, is non-singular at each iteration. In particular, the function sinh has a well defined derivative function and the corresponding Jacobian function can be analytically implemented enhancing the convergence and performance of the method. The final expressions for elemental residual and Jacobian at the α Gauss point level, are:

$$\boldsymbol{F}(\psi_h^\alpha) = \nabla \psi_h^\alpha \cdot \nabla v_h^\alpha + v_h^\alpha \frac{2F \; c^\infty}{\epsilon_0 \epsilon_r} \sinh\left(\frac{F \psi_h^\alpha}{RT}\right) \tag{4.4}$$

$$\boldsymbol{F}'(\psi_h^\alpha) = \nabla v_h^\alpha \cdot \nabla v_h^\alpha + v_h^\alpha \frac{2F^2 \; c^\infty}{RT \epsilon_0 \epsilon_r} \cosh\left(\frac{F \psi_h^\alpha}{RT}\right). \tag{4.5}$$

Charge conservation equation

Using the same functional space, the FEM formulation for the Eq. 3.25 can be given as:

find ϕ_h, such as $\phi_h, v_h \; in \; V_h$ and

$$\begin{aligned} \int_{\Omega^h} \nabla v_h \cdot \left(-\sigma \nabla \phi_h - F \sum_{j=1}^{N} z_j D_j \nabla c_j^h + \rho_e \mathbf{u}_h \right) \, d\Omega^h = 0 \quad \text{in } \Omega^h \\ \phi_h = \phi_\Gamma \text{ at } \Gamma_D \\ \frac{\partial \phi_h}{\partial n} = 0 \text{ at } \Gamma_N. \end{aligned} \tag{4.6}$$

where c_j^h and $\mathbf{u}_h$) are the discretization for the concentration of the j-specie and the velocity fields, respectively. Also, a corollary of the divergence theorem has been applied as follows

$$\int_{\Omega^h} v_h \nabla \cdot \mathbf{i}_h \, d\Omega^h + \int_{\Omega^h} \nabla v_h \cdot \mathbf{i}_h \, d\Omega^h = \int_{\Gamma} (v_h \mathbf{i}_h) \cdot \, d\mathbf{S} = 0 \tag{4.7}$$

where

$$\mathbf{i}_h = -\sigma \nabla \phi_h - F \sum_{j=1}^{N} z_j D_j \nabla c_j^h + \rho_e \mathbf{u}_h \tag{4.8}$$

is the electric current.

Finally, Eq. 4.6 can be simplified as:

$$\begin{aligned} -\int_{\Omega^h} \nabla v_h \cdot (-\sigma \nabla \phi_h) \, d\Omega^h = \int_{\Omega^h} f \, d\Omega^h \quad \text{in } \Omega^h \\ \phi_h = \phi_\Gamma \text{ at } \Gamma_D \\ \frac{\partial \phi_h}{\partial n} = 0 \text{ at } \Gamma_N, \end{aligned} \tag{4.9}$$

where f is a source term calculated as:

$$f = F \sum_{j=1}^{N} z_j D_j \nabla c_j^h - \rho_e \mathbf{u}_h \tag{4.10}$$

All equations used to compute electric potential are elliptical, and through its FEM formulation, symmetric and positive definite (SPD) matrices are obtained. Due tho this, there are not problems with convergence nor stability,

then stabilization terms are not required.

Flow field

In order to compute velocity and pressure fields, Eqs. 3.18 and 3.19 have been used. FEM formulation for these equations, including *Streamline Upwind Petrov Galerkin* (SUPG) and *Pressure Stabilized Petrov Galerkin* (PSPG) were previously implemented in PETScFEM. More details on this implementation can be obtained from the bibliography (Tezduyar et al., 1992; Tezduyar and Osawa, 2000) or from the PETScFEM documentation (Storti et al., 2010).

Mass transport

In order to solve the mass transport problem, Eq. 3.28 was used. The FEM formulation for this equation, by using the Galerkin method, integration by parts, and the aforementioned function space V_h, is:

find c_j^h, such as $c_j^h, v_h \ \in V_h$ and

$$\int_{\Omega^h} v_h \frac{\partial c_j^h}{\partial t} + v_h \nabla \cdot (-z_j \Omega_j^h c_j^h \nabla \phi_h + c_j^h \mathbf{u}_h) - v_h r_j + \nabla v_h \cdot D_j \nabla c_j^h \; d\Omega^h = 0 \text{ in } \Omega^h$$

$$\begin{aligned} c_j^h &= c_{j\Gamma} \text{ at } \Gamma_D \\ \frac{\partial c_j^h}{\partial n} &= 0 \text{ at } \Gamma_N \\ \frac{\partial c_j^h}{\partial n} &= \Phi_j \text{ at } \Gamma_R \end{aligned} \tag{4.11}$$

for $j = 1, 2, 3, ..., N$, where $\Gamma = \Gamma_D \cup \Gamma_N \cup \Gamma_R$, $\Gamma_D \cap \Gamma_N \cap \Gamma_R = \emptyset$, and Γ_R is the boundary portion where Robin boundary conditions are imposed. When this equation is implemented numerically, several problems on stability due to the high value of the Pèclet number arises (Donea and Huerta, 2003), for this

equation this dimensionless number can be written, for the specie j, as

$$\mathrm{Pe_j} = \frac{\mathrm{L} \parallel (-\mathrm{z_j}\Omega_\mathrm{j}^\mathrm{h}\nabla\phi_\mathrm{h} + \mathbf{u}_\mathrm{h}) \parallel}{\mathrm{D_j}} \tag{4.12}$$

where L is a characteristic length. In order to avoid these instabilities, SUPG and *Shock capturing* (SC) were implemented following previous works of Tezduyar and Osawa (2000) and Tezduyar and Senga (2004), respectively. The final FEM equation implemented for the mass transport equation is

$$\begin{aligned}
&\int_{\Omega^h} v_h c^h_{j,t} - v_h \nabla\cdot(z_j\Omega^h_j\nabla\phi_h c^h_j - \mathbf{u}_h c^h_j) - v_h r_j \; d\Omega^h + \int_{\Omega^h} \nabla v_h \cdot D_j \nabla c^h_j \; d\Omega^h - \\
&\sum_{e=1}^{nel} \int_{K^e} \tau_{\mathrm{supg_j}} (z_j\Omega^h_j\nabla\phi_h - \mathbf{u}_h)\cdot\nabla v_h (c^h_{j,t} - r_j - \nabla\cdot(z_j\Omega_j\nabla\phi_h c^h_j - \mathbf{u}_h c^h_j)) \; d\Omega^h \\
+&\sum_{e=1}^{nel} \int_{K^e} \delta_{\mathrm{shock_j}} \nabla v_h \nabla c^h_j \; d\Omega^h = 0
\end{aligned} \tag{4.13}$$

for $j = 1, 2, 3, ..., N$, where nel is the number of elements of T_h, and $c^h_{j,t}$ corresponds to the discrete temporal derivative, following a general Crank-Nicholsohn scheme with real parameter θ, such as $0 \leq \theta \leq 1$. Diffusion term in the *SUPG* integral vanishes for lineal elements, and τ_{supg} calculate for each specie j as follows

$$\tau_{s1} = \frac{\Delta t}{2\theta} \tag{4.14}$$

$$\tau_{s2_j} = \frac{h_{\mathrm{supg_j}}}{2 \parallel (-z_j\Omega^h_j\nabla\phi_h + \mathbf{u}_h) \parallel} \tag{4.15}$$

$$\tau_{s3_j} = \frac{{h_{\mathrm{supg_j}}}^2}{12 D_j} \tag{4.16}$$

$$\tau_{s4_j} = \frac{1}{\nabla\cdot \parallel (-z_j\Omega^h_j\nabla\phi_h + \mathbf{u}_h) \parallel} \tag{4.17}$$

where

$$h_{\mathrm{supg_j}} = \nabla v_h \cdot \left(\frac{(-z_j \Omega_j^h \nabla \phi_h + \mathbf{u}_h)}{\parallel (-z_j \Omega_j^h \nabla \phi_h + \mathbf{u}_h) \parallel} \right) \tag{4.18}$$

finally, if $\parallel (-z_j \Omega_j^h \nabla \phi_h + \mathbf{u}_h) \parallel > \ tol_{\mathrm{supg}}$:

$$\tau_{\mathrm{supg_j}} = \left(\frac{1}{{\tau_{s1}}^2 + {\tau_{s2_j}}^2 + {\tau_{s3_j}}^2 + {\tau_{s4_j}}^2} \right)^{\frac{1}{2}} \tag{4.19}$$

and, if $\parallel (-z_j \Omega_j^h \nabla \phi_h + \mathbf{u}_h) \parallel \leq \ tol_{\mathrm{supg}}$:

$$\tau_{\mathrm{supg_j}} = 0 \tag{4.20}$$

where tol_{supg} is a predefined tolerance depending on the smallest scales of time and longitude involved in the problem.

Also δ_{shock} calculate for each specie j as: if $\parallel \nabla c_j^h \parallel > \ tol_{\mathrm{shock}}$,

$$\delta_{\mathrm{shock_j}} = \frac{h_{\mathrm{shock_j}}}{2} \parallel (-z_j \Omega_j^h \nabla \phi_h + \mathbf{u}_h) \parallel \left(\frac{\parallel \nabla c_j^h \parallel h_{\mathrm{shock_j}}}{c^h_{\mathrm{ref_j}}} \right)^2, \tag{4.21}$$

and, if $\parallel \nabla c_j^h \parallel \leq \ tol_{\mathrm{shock}}$:

$$\delta_{\mathrm{shock_j}} = 0 \tag{4.22}$$

where, $c^h_{\mathrm{ref_j}}$ is a reference value for the concentration of the specie j, and

$$h_{\mathrm{shock_j}} = \nabla v_h \cdot \left(\frac{\nabla c_j^h}{\parallel \nabla c_j^h \parallel} \right) \tag{4.23}$$

where tol_{shock} is a predefined tolerance depending on the smallest scales of concentration and longitude involved in the problem.

4.2 PETSC-FEM for Python

FEM formulations presented were numerically solved within a Python programming environment built upon *MPI (Message Passing Interface) for Python* (Dalcín et al., 2008; Dalcín, 2008), *PETSc for Python* (Dalcín, 2010; Dalcín, 2008), and *PETSc-FEM* (Storti et al., 2010; Sonzogni et al., 2002). PETSc-FEM is a parallel multiphysics code primarily targeted to 2D and 3D finite elements computations on general unstructured grids. PETSc-FEM is based on MPI and PETSc (Balay et al., 2010b), and it is being developed since 1999 at CIMEC. PETSc-FEM provides a core library that manage parallel data distribution and assembly of residual and Jacobian matrices, as well as facilities for general tensor algebra computations at the level of problem-specific finite element routines. Additionally, PETSc-FEM provides a suite of specialized application programs built on top of the core library and targeted to a variety of problems (e.g., compressible/incompressible Navier-Stokes and compressible Euler equations, general advective-diffusive systems, weak/strong fluid-structure interaction, electrokinetic phenomena) that can be easily extended to others applications. In particular numerical calculations presented in this thesis were developed and carried out within the Navier–Stokes module available in *PETSc-FEM*. This module provides the required capabilities for simulating mass transport and incompressible fluid flow through a monolithic *SUPG/PSPG* stabilized formulation for linear finite elements. Accessing PETSc-FEM from a Python programing environment is known in short as PETSc-FEM4Py.

In what follows, the core components of PETSc-FEM4Py are briefly described: PETSc, MPI, and Python. Then a special library extensively used during this thesis, *NumPy*, is also presented.

4.2.1 PETSc

PETSc (Balay et al., 2010b,a), the *Portable Extensible Toolkit for Scientific Computation*, is a suite of algorithms and data structures for the solution of problems arising in scientific and engineering applications, specially those modeled by partial differential equations, of large-scale nature, and targeted

to parallel HPC environments (Balay et al., 1997).

PETSc is written in C (thus making it usable from C++); a Fortran interface (very similar to the C one) is also available. PETSc complete functionality is only exercised by parallel applications, but serial applications are fully supported.

PETSc employs the MPI standard for inter-process communication, thus it is based on the message-passing model for parallel computing. Despite that, PETSc provides high-level interfaces with *collective* semantics so that typical users rarely have to make message-passing calls themselves.

PETSc is designed with an object-oriented style. Almost all user-visible types are abstract interfaces with implementations that may be chosen at runtime. Those objects are managed through handles to opaque data structures which are created, accessed and destroyed by calling appropriate library routines.

PETSc consists of a variety of components. Each component manipulates a particular family of objects and the operations one would like to perform on the objects. Some of the PETSc modules deal with:

- Index sets, including permutations, indexing into vectors, renumbering, etc.
- Vectors.
- Matrices (generally sparse).
- Distributed arrays for parallelizing regular grid-based problems.
- Krylov subspace methods.
- Preconditioners, including multigrid and sparse direct solvers.
- Nonlinear solvers.
- Time-steppers for solving time-dependent, nonlinear partial differential equations.

PETSc provides a rich environment for modeling scientific applications, as well as for rapid algorithm design and prototyping. The libraries enable easy customization and extension of both algorithms and implementations. This approach promotes code reuse and flexibility. PETSc is designed to be highly modular, enabling the interoperability with several specialized parallel libraries like *Hypre* (Falgout et al., 2006), *Trilinos/ML* (Heroux et al., 2003), *MUMPS* (Amestoy et al., 2001), and others through an unified interface.

Finally, in order to avoid accessing through low level programing languages, PETSc for Python was developed (Dalcín, 2010; Dalcín, 2008). This enables the access to all functionalities of PETSc through Python and the integration of PETSc with all the huge amount of programs available in this popular programming environment.

4.2.2 MPI

MPI, the *Message Passing Interface*, is a standardized, portable message-passing system designed to function on a wide variety of parallel computers. The standard defines the syntax and semantics of library routines (MPI is not a programming language extension) and allows users to write portable programs in the main scientific programming languages (Fortran, C, and C++).

The paradigm of message-passing is specially suited for (but not limited to) distributed memory architectures and is used in today's most demanding scientific and engineering applications related to modeling, simulation, design, and signal processing.

MPI defines a high-level abstraction for fast and portable inter-process communication (Snir et al., 1998; Gropp et al., 1998). Applications can run in clusters of workstations (possibly heterogeneous) or dedicated compute nodes, multiprocessors machines, or even a mixture of both. MPI hides all the low-level details, like networking or shared memory management, simplifying development and maintaining portability, without sacrificing performance.

The MPI specifications is nowadays the leading standard for message-passing libraries in the world of parallel computers. Implementations are available from, vendors of high-performance computers to well known open

source projects like MPICH (MPICH2 Team, 2010; Gropp et al., 1996) and Open MPI (Open MPI Team, 2010; Gabriel et al., 2004). Also MPI functionalities can be easily accessed in a Python environment through MPI for Python (Dalcín et al., 2008), as it was performed during this thesis.

4.2.3 Python

Python (van Rossum, 2010a,b) is a modern, powerful programming language. It has efficient high-level data structures and a simple, but effective, approach to object-oriented programming, is easy to learn and highly extensible. It supports modules and packages, which encourages program modularity and code reuse.

The Python programming language has attracted the attention of many users and developers around the world in the scientific community. Python's elegant syntax, together with its interpreted nature, make it an excellent language for scripting and rapid application development. Sophisticated but easy to use and well integrated solutions are available for interactive command-line work, efficient multi-dimensional array processing, linear algebra, 2D and 3D visualization, and other scientific computing tasks.

Python is easily extended with new functions and data structures implemented in compiled languages. This feature allows skilled users to build their own computing environment, tailored to their specific needs and based on their favorite high-performance Fortran, C, or C++ codes.

4.2.4 NumPy

NumPy (Oliphant, 2010) is an open source project providing a fundamental library needed for serious scientific computing with Python.

NumPy provides a powerful multi-dimensional array object with advanced and efficient general-purpose array operations. Additionally, *NumPy* contains three sub-libraries with numerical routines providing basic linear algebra operations, basic Fourier transforms and sophisticated capabilities for random number generation. It also provides facilities in order to support interoperability with compiled languages as C, C++ and Fortran,

Besides its obvious scientific uses, *NumPy* can also be used as an efficient multi-dimensional container of generic data. Arbitrary data-types can be defined. This allows *NumPy* to seamlessly and speedily integrate with a wide variety of database formats.

4.3 Simulation procedure

In what follows the different steps required to build FEM solutions for equations that model analytical process in LOC are presented. These steps are described to carry out simulations of the PDEs already presented or to model new problems.

4.3.1 Implementation of differential equations in PETSc-FEM: *Adaptor*

Once obtained the FEM formulations for the PDE equations, as it was described in section 4.1.1, the corresponding discrete equation system has to be assembled. In PETSc-FEM, this non linear system is assembled through the definition of the residual an Jacobian matrices that enables solving such system through the Newton methods implemented in the *SNES* object from PETSc.

In order to obtain such matrices different contributions of all elements to the different unknowns at nodes (degrees of freedom) have to be computed. This task is easily accomplished by using the *Adaptor* class. Particularly, *Adaptor-pg* enables programing the element contributions to residual and Jacobian matrices. These contributions results from the local (element level) numerical integration which are computed at level of Gauss points. Also *Adaptor-pg* assembles the residual and Jacobian global matrices.

To illustrate the process of implementing a FEM formulation by using the *Adaptor-pg*, the implementation of a particular term of the Eq. 4.13 is shown. In this case, the reaction term is considered due to its relatively complexity, the other terms of the equation, and other equations, can be implemented easily following the same process. Consider the following generic

reaction term for the i-specie in a system with a total amount of Nf species:

$$r_i = \sum_{j=1}^{N} k_{ij} c_j + \sum_{l,m=1}^{N} K_{ilm} c_l c_m \tag{4.24}$$

then, the corresponding weighted integral is

$$\int_\Omega v_h r_i d\Omega = \sum_{j=1}^{N} \int_\Omega v_h k_{ij} c_j^h d\Omega + \sum_{l,m=1}^{N} \int_\Omega v_h K_{ilm} c_l^h c_m^h d\Omega. \tag{4.25}$$

By using the Einstein notation, the residual at a generic Gauss point α, for the specie i is:

$$R_i^\alpha = v_h^\alpha k_{ij} u_j^h + v_h^\alpha K_{ilm} u_l^h u_m^h \tag{4.26}$$

where u_j^h is the state for the j-specie projected at the Gauss point as $u_k^h = v_h^\alpha c_{k(\alpha)}^h$. The corresponding Jacobian term is calculated as the partial derivative of the residual with respect the state for all the species, at a generic Gauss point β,

$$J_{i,n}^{\alpha,\beta} = \frac{\partial R_i^\alpha}{\partial c_{n(\beta)}} = v_h^\alpha k_{ij} \left(\frac{\partial u_k^h}{\partial c_{n(\beta)}} \right) + v_h^\alpha K_{ilm} \left(\frac{\partial u_l^h}{\partial c_{n(\beta)}} u_m^h + \frac{\partial u_m^h}{\partial c_{n(\beta)}} u_l^h \right) \tag{4.27}$$

taking into account that

$$\frac{\partial u_k^h}{\partial c_{n(\beta)}} = \frac{\partial (v_h^\beta c_{k(\beta)}^h)}{\partial c_{n(\beta)}} = v_h^\beta \delta_{kn} \tag{4.28}$$

where δ_{kn} is the *Kronecker* delta. Finally, for the the common case, where K is symmetric, the expression results

$$J_{i,n}^{\alpha,\beta} = v_h^\alpha k_{in} v_h^\beta + 2 v_h^\alpha K_{iln} v_h^\beta u_l^h \tag{4.29}$$

Then, Eq. 4.26 and 4.29 have to be implemented by using the *Adaptor-pg*

class as follows

$$\begin{aligned}
&\mathbf{tmpr.prod}(\mathbf{u},\mathbf{k},-\mathbf{1},\mathbf{1},-\mathbf{1});\rightarrow\ u_j^h k_{ij}\\
&\mathbf{tmpr1.prod}(\mathbf{u},\mathbf{u},\mathbf{1},\mathbf{2});\rightarrow\ u_l^h u_m^h\\
&\mathbf{tmpr2.prod}(\mathbf{K},\mathbf{tmpr1},\mathbf{1},-\mathbf{1},-\mathbf{2},-\mathbf{1},-\mathbf{2})\rightarrow\ K_{ilm}u_l^h u_m^h\\
&\qquad\mathbf{.add}(\mathbf{tmpr});\qquad\qquad\qquad\qquad\rightarrow\ +u_j^h k_{ij}\\
&\mathbf{tmpr3.prod}(\mathbf{shape}(),\mathbf{tmpr2},\mathbf{1},\mathbf{2});\rightarrow\ v_h^\alpha(K_{ilm}u_l^h u_m^h + u_j^h k_{ij})\\
&\mathbf{res_pg.set}(\mathbf{tmpr3});\rightarrow\ R_i^\alpha = v_h^\alpha(K_{ilm}u_l^h u_m^h + u_j^h k_{ij})\qquad (Eq.\ 4.26)
\end{aligned}$$

$$\begin{aligned}
&\mathbf{tmpj.prod}(\mathbf{shape}(),\mathbf{shape}(),\mathbf{1},\mathbf{2});\rightarrow\ v_h^\alpha v_h^\beta\\
&\mathbf{tmpj1.prod}(\mathbf{K},\mathbf{u},\mathbf{1},-\mathbf{1},\mathbf{2},-\mathbf{1}).\mathbf{scale}(\mathbf{2.0}).\mathbf{add}(\mathbf{k});\rightarrow\ 2K_{iln}u_l^h + k_{in}\\
&\mathbf{tmpj3.prod}(\mathbf{tmpj},\mathbf{tmpj1},\mathbf{1},\mathbf{3},\mathbf{2},\mathbf{4});\rightarrow\ v_h^\alpha v_h^\beta(2K_{iln}u_l^h + k_{in})\\
&\mathbf{mat.set}(\mathbf{tmpj3});\rightarrow\ J_{i,n}^{\alpha,\beta} = v_h^\alpha v_h^\beta(2K_{iln}u_l^h + k_{in})\qquad (Eq.\ 4.29)
\end{aligned}$$

where all data structures used are tensors from the class *FastMat2*, and function **prod**() is a generic tensorial product that contracts negative index and order the resulting tensor as the positive numbers indicate. For example, the product

$$C_{ij} = A_{ik}B_{kj} = \sum_k a_{ik}b_{kj}$$

is implemented as

$$\mathbf{C.prod}(\mathbf{A},\mathbf{B},\mathbf{1},-\mathbf{1},-\mathbf{1},\mathbf{2}).$$

Other functions available for *FastMat2* may be consulted from the source code, or from Paz et al. (2010).

4.3.2 Accessing PETSc-FEM elements

After programing the desired PDE as a FEM problem by using the *Adaptor-pg*, the resulting FEM problem become a PETSc-FEM *elemset* class. This

elemset provides the solution to a particular PDE, but the PDE itself is not a physical problem. In order to define a physical problem, it is mandatory to have a geometric domain, boundary conditions, constants, interacting fields, etc. Then the elemset (PDE) have to be instanced inside a PETSc-FEM *domain* (physical problem) in order to set all the information that the problem requires. Setting all this information and finally solving the problem is achieved through PETSc-FEM4Py.

Figure 4.2 shows a block diagram of the file structure used for simulation processes during this thesis. There are seven blocks that represents files or *Python* scripts that perform several task, such as accessing the information that defines the problem, exchanging information with the core of PETSc-FEM4Py to set up the problem, calling the solver to get the solution, and finally storing the results in a suitable format. In what follows, a description of each one of this blocks is presented.

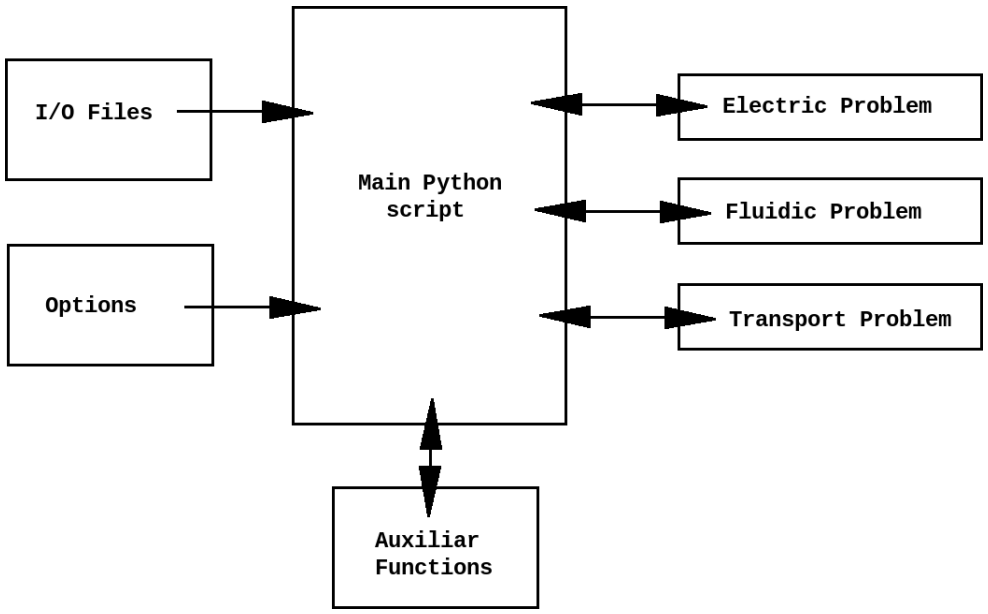

Figure 4.2: Block diagram of the file structure for the simulations.

4.3.3 The main Python script

The main Python script manage all the calls that have to be done to solve the entire problem, with the three subsidiary fields (electric potential, fluid flow and mass transport). It has, basically, three fundamental parts: pre-processing, solving, and post-processing.

The pre-processing involves the collection of all the data that defines the problem, that is:

- Mesh data: node coordinates, connectivity, element geometry, boundary nodes/elements.
- Boundary conditions: for the three associated problems including Dirichlet and Neumann conditions.
- Constants: physicochemical constants that defines the problems (density, mobilities, valences, etc.).
- Initial conditions.

After collecting all this information, the main Python script manages the calls to *setDomain()*, and *solve()* functions for the different domains, and manages the coupling between them by processing partial results in the time stepping scheme. This process is depicted in Fig. 4.3. Starting from an initial or previous state ($\phi^n,\ \mathbf{u}^n,\ p^n,\ c_j^n$), several fields related to the ion concentration, as the conductivity (Eq. 3.26), electric charge density (Eq. 3.4), electrokinetic potential (Eq. 3.27), effective mobility (Eqs. 3.38, and 3.39), and variable reaction coefficients (Eqs. 3.46 - 3.50).

After calculating these fields, the first unknown field to be updated is the electric potential ($\phi^n \rightarrow \phi^{n+1}$). By using the updated electric potential ϕ^{n+1}, the new velocity and pressure fields are calculated ($\mathbf{u}^n,\ p^n \rightarrow \mathbf{u}^{n+1},\ p^{n+1}$). Finally, by using the updated electric and fluid fields, the concentration field is updated ($c_j^n \rightarrow c_j^{n+1}$) for all the specie simultaneously. For the proposed temporal scheme, the electric and fluid fields are treated as quasi-steady due to the fact that time constants for advective and diffusive phenomena are much larger than the reaction coefficients in the mass transport equation (Eq. 3.28).

In consequence, there exist two time steps that govern the solution of the complete problem. The longer time step (Δt_1) corresponds to the actualization of electric and fluid field, and it its determined in order to assert correct Courant numbers (usually in the order of 1):

$$Cou = max \left\{ \frac{\parallel (-z_j \Omega_j^h \nabla \phi_h + \mathbf{u}_h) \parallel \times \Delta t_1}{h_{\mathrm{supg_j}}} \right\} \tag{4.30}$$

The shorter time step (Δt_2) is used in order to update the concentration fields without updating neither the electric nor fluid fields. This time step is determined by the reaction coefficients that model the faster reactions.

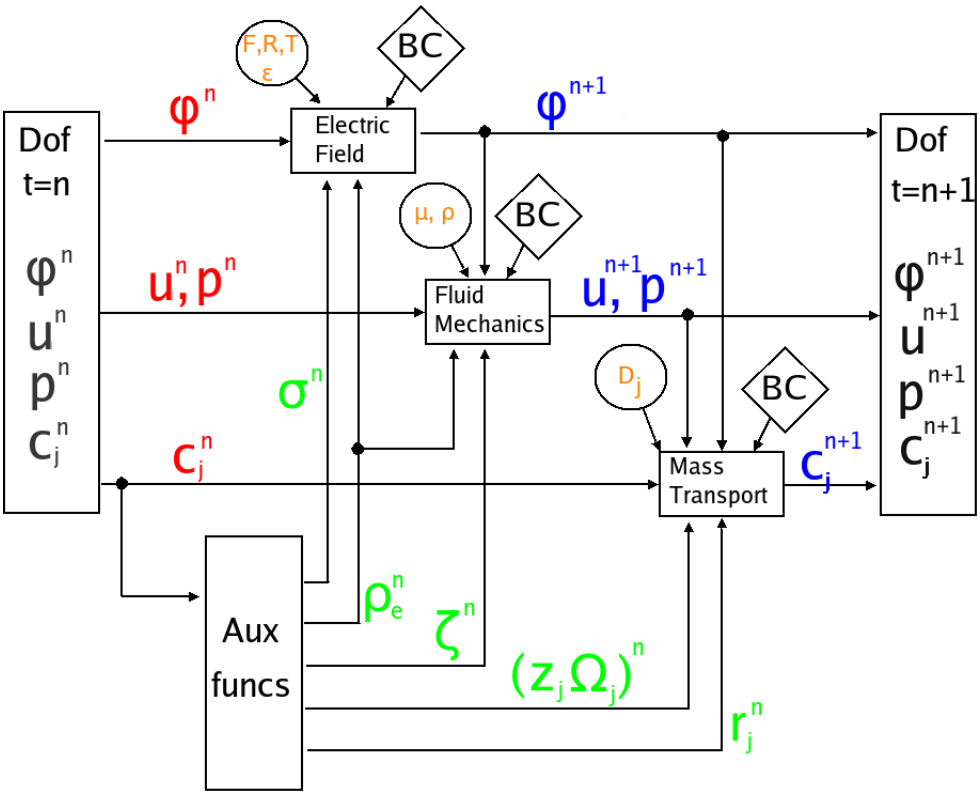

Figure 4.3: Block diagram of the temporal scheme of solution procedure.

Finally, the post-processing involves the storing of the solution in a suitable form to be used in future calculations as initial conditions (binary files) or for

visualization (vtk files).

4.3.4 The PETSc-FEM4Py domains

In PETSc-FEM4Py, the class *domain* has several methods that enable to define a problem in a complete way; some of the more commonly used are

- *setNodedata()*: allow to set the mesh for the problem.
- *addElemset()*: allow to associate a PDE to the problem.
- *setField()*: allow to set different fields that are involved in the problem.
- *setFixation()*: allow to set different Dirichlet boundary conditions for the problem.
- *setConstraint()*: allow to set lineal constraints between different degrees of freedom at certain nodes.
- *setUp()*: sets up the entire problem transforming it into a discrete equation system.

Once the problem is defined and set up, it is ready to be solved. In order to achieve this task, an object of the *solver* class (also a class of PETSc-FEM4Py) has to be instanced, and the argument for this call is the previously set up domain. After this instantiation, many options for the solver could be set following the PETSc standards already mentioned. Finally, the call to the *Solve()* function, with the initial condition as argument, starts the numeric solving process, giving as result the solution field.

All this features are packed in Python objects that supports calls to *setDomain()* and *Solve()* functions from the main script.

4.3.5 In/Out routines

The main script reads the I/O file that contains the names of different files with data related to the constitution of the problem. As was described in the main script pre-processing stage, these file names are, mesh, initial conditions,

the prefix for the name of output files, and the name of the file where the corresponding auxiliary functions are implemented.

Mesh file is read through a Python translator, programed ad-hoc for each mesh generator, such as *NetGen*, *TetGen* or *Gambit* among others. Boundary conditions and constants are defined in text files easy to write and modify by the user, and accessible from particular *setDomain()* functions.

Solutions are stored in two processes. The first process consist in storing binary files in order to use them later as initial conditions in new problems. This process is achieved easily with the *shelve* Python class (van Rossum, 2010a).

The second process is the generation of files that can be opened by the post-processing or visualization programs. There exists many formats to carry out this task, for the sake of simplicity the chosen were the binary *vtk* (visualization toolkit) files. After getting the solution as a Numpy array, a home-made vtk-writer called *PyVtk2*, transform the arrays of the solution fields in a standard vtk file. Finally these vtk files can be opened by Paraview (Sandia and CSim-Soft, 2010) or Mayavi (Ramachandran, 2010), among others post-processing programs.

4.3.6 Options

The options file is also read by the main Python script, through the PETSc options object, and it contains several options for solving problems as follows:

- Time-stepping: it sets the initial and final times, the time-step, and particular times to store.
- Mesh options: the program that generated the mesh, and the geometry of element.
- Problems: it selects the fields to be solved.
- Models: it selects the particular PDE for each problem (i.e. for the electric field: Laplace equation, Poisson equation, Poisson-Boltzmann or charge conservation).

- Refinement options: it sets different parameters related to the adaptive refinement as level refinement or time-steps between refinements among others.

- Solver options: it sets the different parameters for each solver, as preconditioners or tolerances, among others.

4.3.7 The auxiliary functions

The auxiliary file contains a complete set of functions implemented in Python that enables different kind of calculations that are mandatory to solve different problems. These calculations include nonlinear equations to calculate pH (Eq. 3.41) or ζ-potential (Eq. 3.27), equations to calculate conductivity, σ (Eq. 3.26), effective mobility (Eqs. 3.38, 3.39), or reaction coefficients (Eqs. 3.33 - 3.36, 3.43, 3.44, 3.46 - 3.50), among others. Also, the interfacing with the mesh refinement algorithms is performed at this level.

Chapter 5

Application Examples

This chapter presents several examples of numerical simulation for analytical processes in LOC. The first section is devoted to validate the mathematical model and simulation tools developed during this thesis. These examples were taken from the literature and consist in numerical or analytical calculations widely used to validate electrophoretic separation models.

In the second section, different experimental setups for analytical processes in labs taken from the literature, are simulated. Finally, last section presents some numerical tests performed to evaluate domain decomposition technique as preconditioner in solving equation systems from LOC numerical models.

Simulations were carried out by using a 64-bit Beowulf cluster, *Aquiles* (Storti, 2010). The hardware consists of 82 disk-less single processor computing nodes with Intel Pentium 4 Prescott 3.0GHz 2MB cache processors, Intel Desktop Board D915PGN motherboards, Kingston Value RAM 2GB DDR2 400MHz memory, and 3Com 2000ct Gigabit LAN network cards, interconnected with two 3Com SuperStack 3 Switch 3870 48-ports Gigabit Ethernet. The server is a processor dual quad core Intel Xeon E5335 of 2 GHz and 16 GB of RAM (400 MHz DDR), Gigabit Lan on board. The hard disk storage has 2 TBytes.

5.1 Validation examples

In this section two numerical examples taken from the literature are simulated. The first example is a simulation of an an IEF assay based on immobilized pH gradient (IPG) presented by Palusinski et al. (1986). In this foundational work, an analytical solution was presented and it has become a benchmark for modelling electrophoretic separations. As a complement, the effects of undesired electroosmotic velocity in this system are shown. The second example is based in previous numerical simulations presented by Shim et al. (2007), by using the software *GENTRANS* for an ampholyte based IEF. This software, previously mentioned in chapter 2, represent one of the most recognized simulation tools for electrophoretic separations.

5.1.1 Isoelectric focusing by immobilized pH gradient

Stagnant fluid

Histidine IEF by IPG reported in the literature (Palusinski et al., 1986; Chatterjee, 2003) is reproduced here. The aminoacid histidine is focused in a straight channel (0.1 x 1.0 cm^2). IPG is achieved by immobilizing cacodylic acid (CACO) and tris(hydroxymethyl)-aminoetane (TRIS). Physicochemical parameters are summarized in Table 5.1.

A constant current density $i = 0.2$ Am^{-2} is imposed, this condition is attained by applying an appropriate potential difference $\Delta\phi$, which is instantaneously corrected with the actual value of σ. The anode is located at the left side ($x = 0.0$ cm) of the channel, and cathode at the right side ($x = 1.0$ cm). The concentrations of CACO and TRIS are fixed in a linear way to obtain the pH profile shown in Fig. 5.1, histidine flux through the up and bottom walls is set to zero.

After the IPG is established, a sample of 1 mM histidine is injected into the whole channel. Then, a constant current density has to be imposed. Concentration of histidine and conductivity profiles at different times at the center of the channel are shown in Figs. 5.2a and 5.2b, respectively. The conductivity profile clearly shows the effect of the histidine concentration. During the

Component	pK_a	pK_b	pI	**Mobility** (m^2/Vs)	**Diffusivity** (m^2/s)
histidine	6.04	9.17	7.50	$2.02\ 10^{-8}$	$5.22\ 10^{-10}$
CACO	6.21	–	–	0.0	0.0
TRIS	–	8.30	–	0.0	0.0

Table 5.1: Physicochemical properties of buffer constituents and analyte (Palusinski et al., 1986; Chatterjee, 2003).

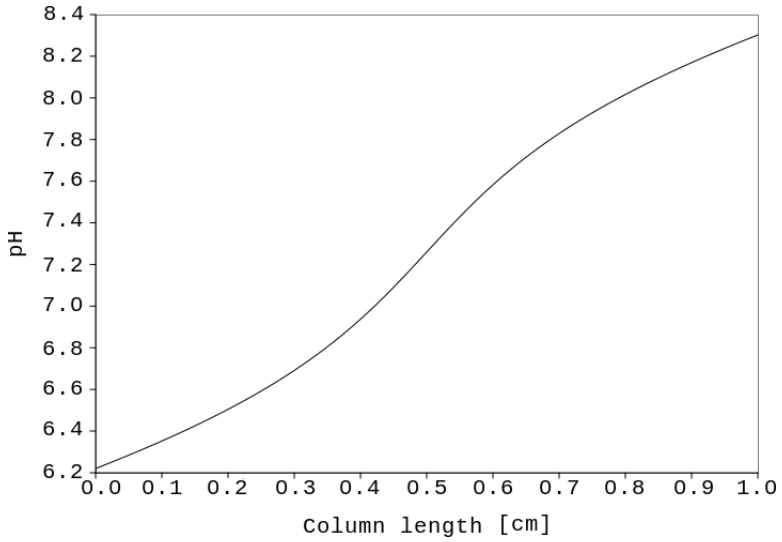

Figure 5.1: Calculated pH profile along the channel for concentration of CACO and TRIS reported in Palusinski et al. (1986).

focusing process conductivity follows the histidine concentration, decreasing considerably at channel ends. As a consequence, the electric field (which is directly coupled to conductivity by Eq. 3.25) raise at this regions, further increasing the focusing process. Results reasonably agree with those previously reported. Histidine concentration for the complete channel at different times are shown in Fig. 5.3.

Electroosmotic flow effects

The previous example involved no bulk flow. In practice, this situation is hard to reach because the ζ-potential cannot be reduced to zero, and the resulting EOF has strong effects in focusing performance. Several attempts to quantify

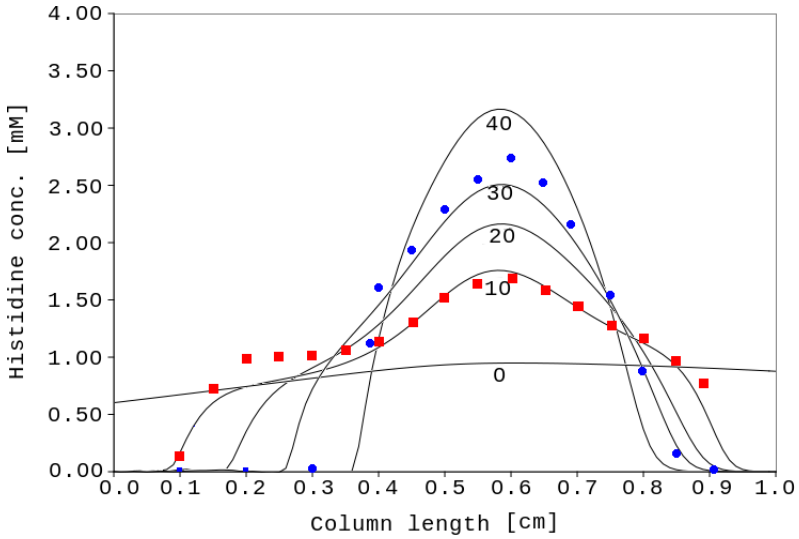

(a) Histidine concentration.

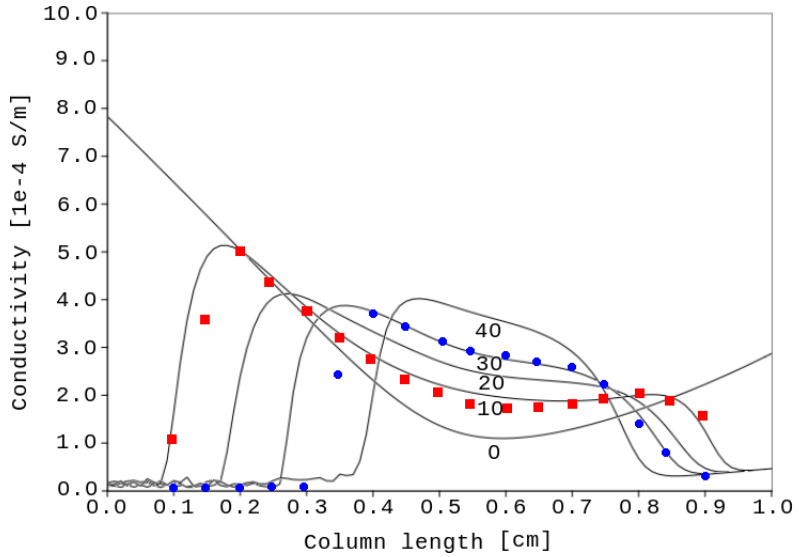

(b) Conductivity.

Figure 5.2: Concentration and conductivity profiles along the channel at 0, 10, 20, 30 and 40 minutes. Full lines are the results of present work. Symbols corresponds to the values obtained by Palusinski et al. (1986); squares for 10 minutes and circles for 30 minutes.

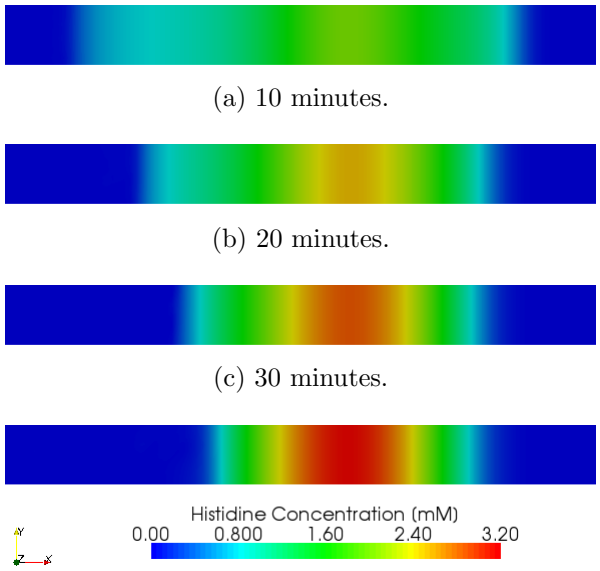

(a) 10 minutes.

(b) 20 minutes.

(c) 30 minutes.

(d) 40 minutes.

Figure 5.3: Histidine concentration profiles at 10, 20, 30 and 40 minutes.

this effect were reported in the literature (Herr et al., 2000; Thormann et al., 2007). Here we simulate the histidine focusing problem with bulk flow due to the presence of EOF. The magnitude of the flow is related to the local electric field, wall electric properties and buffer solution composition, as described in Section 5.1.2. Calculations were carried out by using numerical values of the previous example (Table 5.1).

Additionally to the conditions used in the previous example, here pressure is set to 0 Pa at the cathode, tangent velocity is set to 0 m/s at the anode and the cathode. As the calculation domain is 2D ($x-y$ plane, see Fig. 5.5), the simulation implicitly assumes that the channel is considerably larger in the z direction that in the y direction. Therefore, EOF slip velocity (Eq. 3.13) is included as the boundary condition at planes $y = 0.0$ cm and $y = 0.1$ cm only.

In this case, due to the variation of pH along the channel, the wall ζ-potential was modelled with Eq. 3.27. Parameters for this equation are: $pK_s = 7.0$ and $n_s = 1.22\ 10^{16} + 7.3\ 10^{16} c_0$, where c_0 is the local ion concentration (Berli et al., 2003). ζ-potential distribution at lateral walls as a function of the channel length is shown in Fig. 5.4.

Figure 5.5 shows 2D plots of conductivity, electric field, pressure and fluid

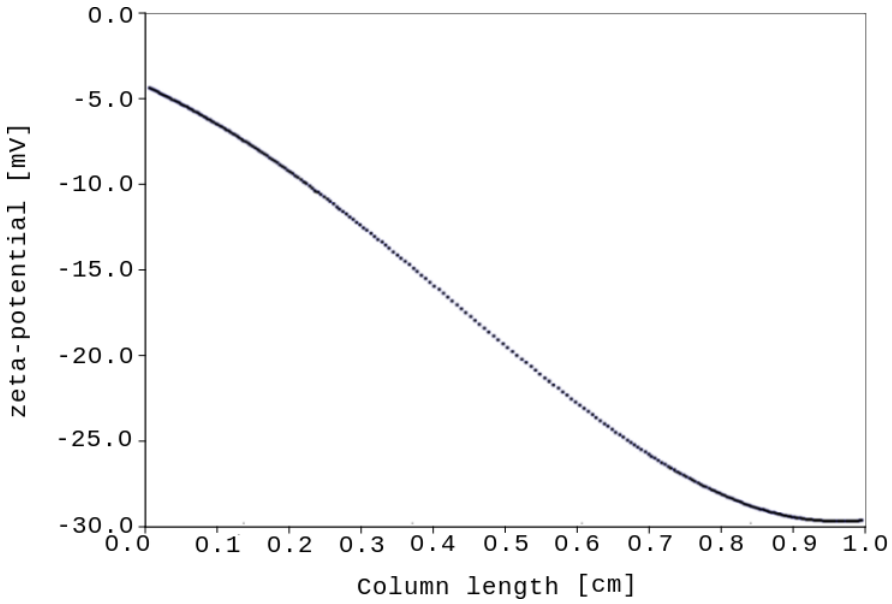

Figure 5.4: $\zeta - potential$ distribution along the channel.

velocity, 2 minutes after the external potential is applied. A strong coupling between these fields is observed. In fact, the fluid velocity is determined by both (i) ζ, which depends on pH and I, and (ii) E which in turn depends on σ (Figs. 5.5a and 5.5b). The superposition of these effects generates a non-uniform fluid velocity field along the channel (Fig. 5.5c) and the consequent pressure gradients (Fig. 5.5d). These non-uniformities are well known from ITP where electric field spatial variations due to conductivity gradients are important (Thormann et al., 2007). Here non-uniform ζ-potential effects are simulated without approximations. It is worth noting that previous works (Thormann et al., 2007) use an spatially averaged electro-osmotic velocity. Finally, under the conditions of this example, the influence of $E(\sigma)$ prevails. Results shown in Fig. 5.5 are in agreement with experiments (Herr et al., 2003) and simulations (Thormann et al., 2007) reported in the literature. Focusing efficiency decreases due to the sample dispersion (non uniform transverse velocity profile) and the reduction of the sample residence time in the channel. This situation can be inferred from Fig. 5.6.

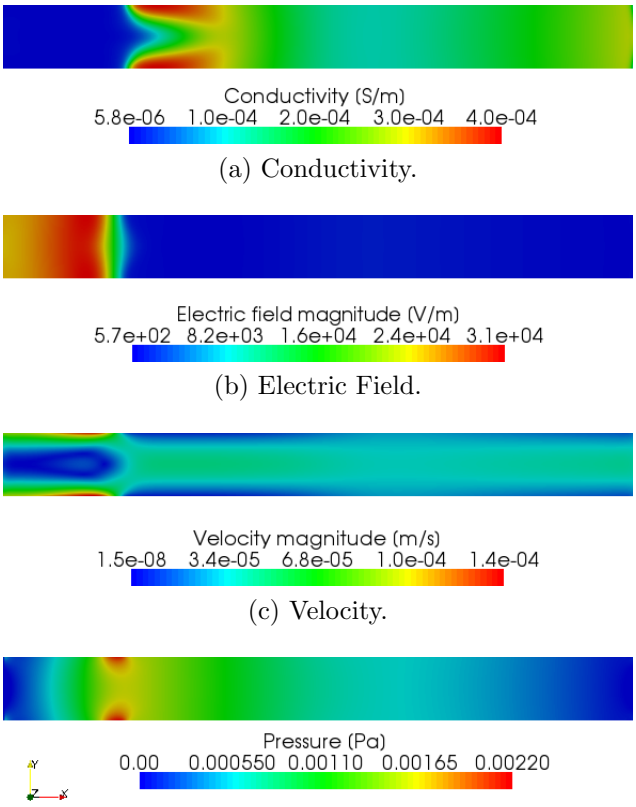

(a) Conductivity.

(b) Electric Field.

(c) Velocity.

(d) Pressure.

Figure 5.5: Important magnitudes for the fully coupled simulation of IEF with EOF at $t = 2$ minutes.

5.1.2 Isoelectric focusing by ampholyte-based pH gradient

Another way to implement IEF consists in using a mixture of carrier ampholytes, which naturally generates a pH gradient under the influence of an electric field. Here we simulate an IEF assay where the pH gradient is generated by ten ampholytes in solution. A 2D microchannel is modelled by a rectangle (0.01 x 1.0 cm^2). Physicochemical properties of the ampholytes (Table 5.2) were taken from the literature (Shim et al., 2007). Also in these calculations, mobility, $\Omega = 3\ 10^{-8}$ m^2/Vs, and diffusivity, $D = 7.75\ 10^{-10}$ m^2/s, are used for all ampholytes. Initially ampholytes are uniformly distributed in the channel.

Potentials applied are 0 V at the cathode ($x = 0.0$ cm) and 100 V at the

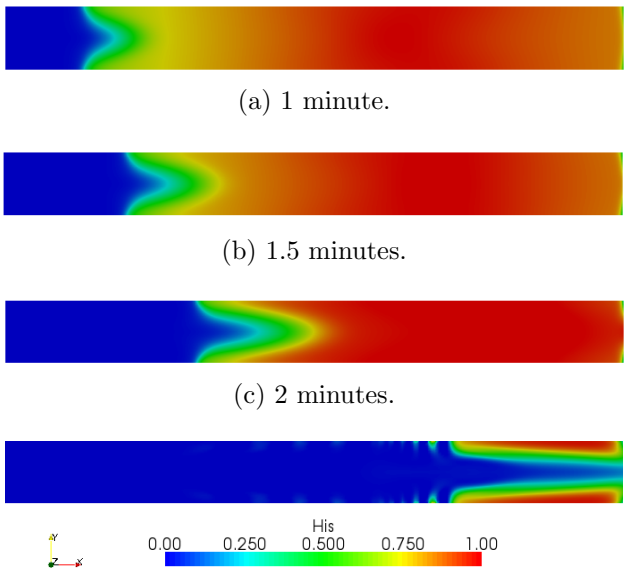

(a) 1 minute.

(b) 1.5 minutes.

(c) 2 minutes.

(d) 2.5 minutes.

Figure 5.6: Histidine concentration profiles at 1, 1.5, 2 and 2.5 minutes.

Ampholyte	pK_a	pK_b	pI
1	6.01	6.41	6.21
2	6.25	6.65	6.45
3	6.47	6.87	6.67
4	6.71	7.11	6.91
5	6.94	7.34	7.14
6	7.17	7.57	7.37
7	7.51	7.91	7.71
8	7.64	8.04	7.84
9	7.87	8.50	8.30
10	8.10	8.50	8.30
Protein	7.00	7.60	7.30

Table 5.2: Physicochemical properties of buffer constituents and analyte.

anode ($x = 1.0$ cm). Compounds fluxes through the walls is set to zero, except for H^+ and OH^- ions at the interfaces of anolyte and catholyte.

Figure 5.7a shows the pH gradient at different times, after applying the potential difference. Predictions of the model presented in this thesis are compared to previous results (Fig. 5.7b). Unlike the IPG, ampholyte-based pH gradient has a strong transient behavior that can be inferred from Fig. 5.8.

After 80 s under the effect of the electric field, ampholytes are focused around its pI, which yield different pH steps along the channel. The step-like shape is a consequence of the reduced number of ampholytes (Svensson, 1961).

It is worth noting that in the original work of Shim et al. (2007) there are no comments on Joule heating effects. By supposing a square section for the capillary tube, and no heat dissipation to the ambient, the internal temperature will increase hundreds of °C after 80 seconds of applying electric potential. This situation does not match the hypothesis of isothermal conditions stated at the beginning of section . In order to not lose formalism on the modelling nor the simulation the assumption that the system has a heat exchanging system, efficient enough to enable the dissipation of the generated heat, has to be done.

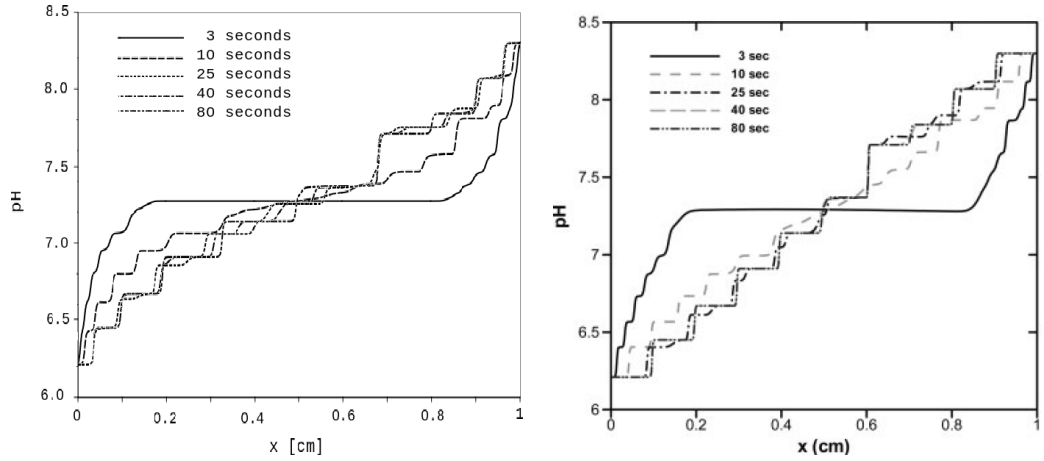

(a) (b)

Figure 5.7: pH along the center of the channel for 3, 10, 25, 40 and 80 seconds. (a) Present work. (b) Shim et al. (2007). © Wiley-VCH Verlag GmbH and Co. KGaA. Reproduced with permission.

Figure 5.9a shows the protein concentration as a function of channel length, for different times. During the transient state, protein exhibits twins peaks at both sides of its pI. These peaks move symmetrically towards the pI until focusing is achieved.

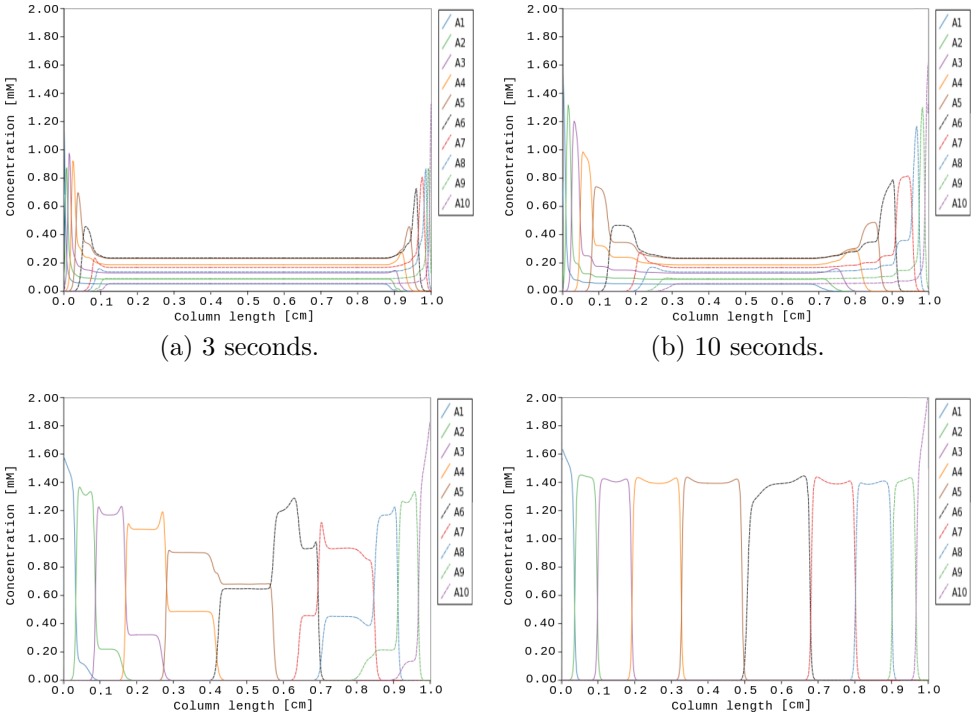

(a) 3 seconds.

(b) 10 seconds.

(c) 40 seconds.

(d) 80 seconds.

Figure 5.8: Ampholyte concentration along the center of the channel at 3, 10, 40 and 80 seconds.

5.2 Simulations of analytical processes in LOC

In this section simulations of different analytical techniques in LOC are presented. Most of the simulations are based in processes carried out experimentally in real devices reported in the specific literature. The aim of the section is to show the capabilities of the tools developed to simulate LOC that are currently in use by the scientific community. The examples presented include CZE, ITP, two dimensional electrophoresis, immunoassay and enzymatic based assays. Capabilities of the method are not only related with the HPC resources employed, that enables to solve large scale problems, but also with the general treatment of the modelling that enables such a wide range of applications.

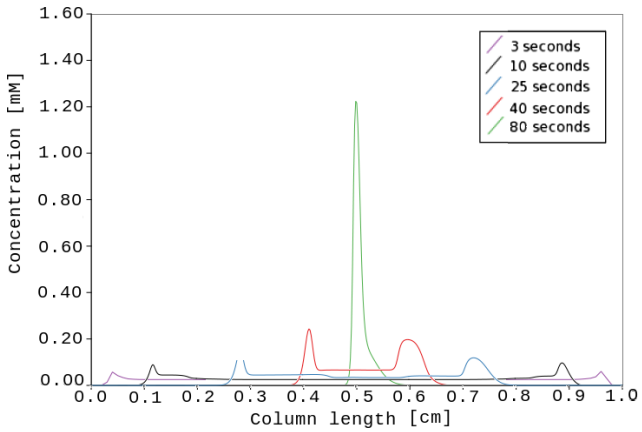

(a) Protein distribution along the center of the channel for 3, 10, 25, 40 and 80 seconds.

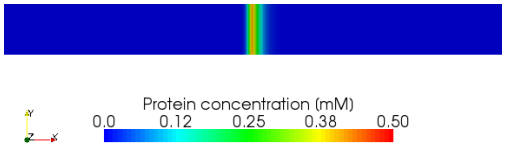

(b) Protein distribution after 80 seconds. Vertical axis is scaled by 10 for better visualization.

Figure 5.9: Protein distribution in example 5.1.2

5.2.1 Capillary Zone Electrophoresis

Previous works related to numerical simulation of electroosmotic flow and electrophoresis have restricted the problem domain to the microchannels by supposing appropriate conditions for the electric potential, velocity field, and concentrations at inlet and outlet regions (Erickson, 2005; Barz and Ehrhard, 2007). In this example, results from numerical simulations of CZE of strong electrolytes performed on a whole microfluidic system domain are presented.

The simulation domain is a a cross-shaped microchannel network with cylindrical reservoirs at the ends, with vertical wire electrodes. The channel sections are trapezoidal, with shape and dimensions shown in figure 5.10. The aim of the example is to show the capability of the numerical method for simulate 3D high aspects ratio geometries, simulating a common situation in practical microfluidics. A more complete analysis of the effects of reservoirs in microfluidics networks can be found in the work of Yang et al. (2005).

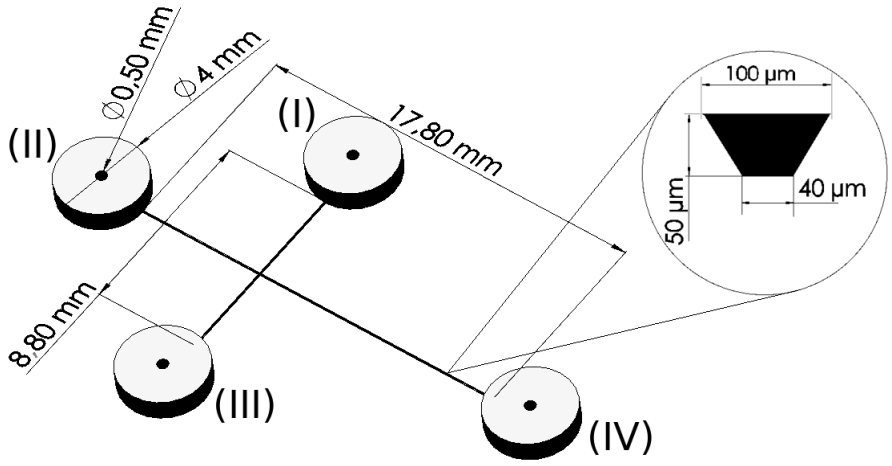

Figure 5.10: Geometry of the microchannel network.

Electrophoretic injection and separation processes are simulated in order to determine potassium and sodium ion concentrations. During the injection stage, potentials at the electrodes are selected in such a way that the intersection region is filled with a precise sample volume to be analyzed. In the separation stage, potentials at the electrodes are appropriately selected in order to achieve different relative velocities for each specie, avoiding leakages at the injection channels.

In order to solve this example some assumptions were made. We have considered strong electrolytes for buffer and sample components, buffer ions concentration is constant in the whole domain, and the sample concentration is adequately low in order to not affect the electric properties of electrolyte solution nor the electric double layer characteristics.Physicochemical properties of analytes are listed in Table 5.3. Also we have considered that the relation between the channel width and the Debye length is large enough to use the Helmholtz-Smoluchowsky slip velocity approximation.

It is worth noting that, even when reservoirs are open to the atmosphere, pressure differences between channel ends may take place due to unequal fluid heights (hydrostatic pressure), or due to differential meniscus curvatures in the reservoirs (Laplace pressure). For the purposes of this example, it is assumed that there are no Laplace pressure differences between them. This assump-

tion results reasonably taken into account that all reservoirs present the same internal radius, and are filled with the same liquid (same surface tension coefficient).

Component	**Mobility** (m^2/Vs)	**Diffusivity** (m^2/s)	**Initial concentration**
sodium	$4.88 \cdot 10^{-8}$	$1.34 \cdot 10^{-9}$	1.0 mM
potassium	$7.24 \cdot 10^{-8}$	$1.96 \cdot 10^{-9}$	1.0 mM

Table 5.3: Analyte properties used in example 5.2.1.

A tetrahedral mesh with 941056 elements was generated in order to solve the problem, the channel flow section contains approximately 60 elements. The electric field are obtained through solving Eq. 3.25, and employing Dirichlet boundary conditions at electrodes and homogeneous Neumann boundary conditions at channels and reservoirs walls. Applied potentials for different processes are shown in Table 5.4. The influence of the applied potentials over the EDL distribution is neglected. The validity of this assumption is evaluated measuring the magnitude of the two different electric fields. Then, the electric field applied is approximately 39 KV/m and the EDL associated electric field is in the order of 4000 KV/m. For this and for all examples presented in this section, Eq. 3.25 was solved by using conjugate gradient method as iterative solver, and HYPRE BoomerAMG (Falgout et al., 2006) was chosen as preconditioner.

Process	**Electric Potential [V]**			
	Φ_I	Φ_{II}	Φ_{III}	Φ_{IV}
Injection	500.0	250.0	0.0	250.0
Separation	530.0	750.0	530.0	0.0

Table 5.4: Applied potential for different processes in CZE.

Fluid velocity was obtained by solving Eqs. 3.18 and 3.19. At the top of the reservoirs, Dirichlet boundary conditions with a reference value of zero were imposed for pressure, and the velocity direction was constrained to be parallel to the reservoir axis. At the channel walls, the slip velocity approximation (equation 3.13) was employed as Dirichlet boundary condition. In this example

the fact that external pressure gradients were set to zero and ζ-potential has a uniform value at channel's surfaces, causes that driving force reduces only to its electroosmotic component. Then the velocity profile is merely plane an its average magnitude equal to the slip velocity calculated by equation 3.13, i.e., 1.1 mm/s.

Finally, transport equation 3.28 was solved for the concentrations of Na^+ and K^+ ions by employing the electric field and fluid velocity previously obtained. Initial concentrations (at $t = 0$ s) were set to zero everywhere except at the reservoir III.

In solving equations 3.19 and 3.28 for this problem, and also for the other examples presented in this section, additive Schwartz method was used as a left preconditioner, with one layer of overlapping between subdomains, with a maximum size of 2000 unknowns in each subdomain. GMRES was employed as iterative solver, and LU factorization was used in each subdomain.

Figure 5.11 shows sample distribution in the central region of the cross network, previous to the separation process, and mesh details in the region near the electrode. Figure 5.12 shows concentration distributions of Na^+ and K^+ ions at some moment ($t = 5$ s) during the separation stage.

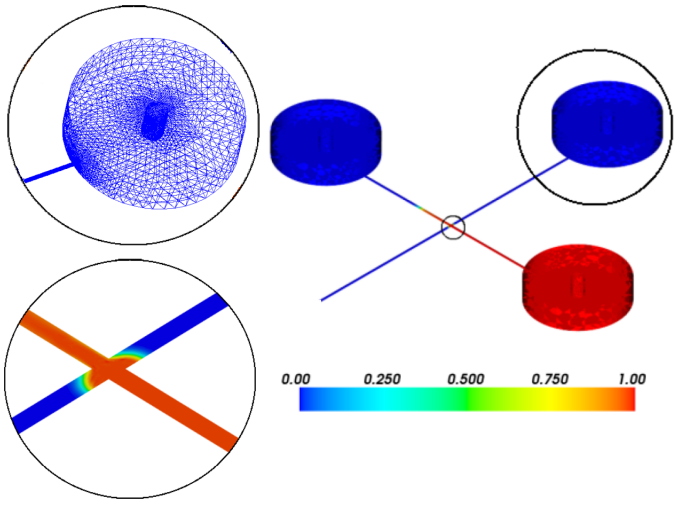

Figure 5.11: Sample concentration (mol/m^3) after the injection stage and mesh detail in electrode zone.

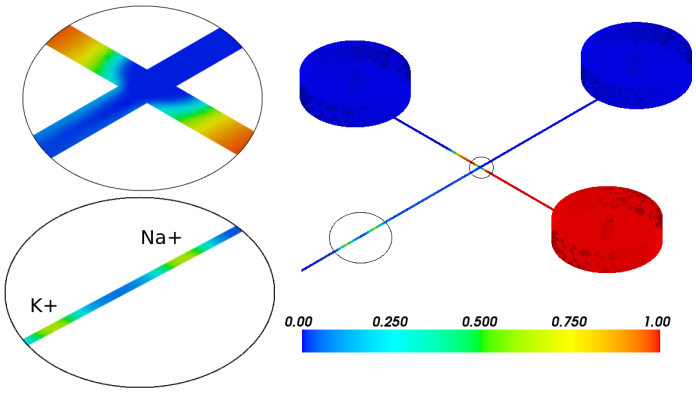

Figure 5.12: Na^+ and K^+ ions concentrations (mol/m^3) after separation stage.

5.2.2 Capillary isotachophoresis

In this example a capillary ITP is simulated. The particularity of this assay is the implementation of label free technique developed by Khurana and Santiago (2008). The method consist in the indirect detection of non-fluorescent specie by using fluorescent mobility markers. These fluorescent markers and the analytes are initially mixed homogeneously and ITP is initiated. The dynamics of ITP cause the analyte and fluorescent marker mixture to segregate into respective zones between the leading electrolyte (LE) and the terminating electrolyte (TE) following the stacking process described in section 1.3.2. Unlabeled analytes are detected as gaps (regions with local minimums in intensity) in the fluorescent signals of mobility markers. The assay is carried out in a single microchannel after a suitable injection process has been accomplished.

Computational domain consist in a rectangular microchannel (0.1 x 6.0 mm^2) in which acetic acid and 3-phenylpropionic acid are separated. Also three fluorescent markers are added in order to develop the detection technique already described. Physicochemical properties and initial concentrations of buffer constituents and analytes are listed in Table 5.5.

The LE is composed of TRIS-HCl and the TE is composed of Tris-Tetraphenylborate. TRIS concentration is determined to achieve an initial pH of 9.2 in the region between LE and TE. Potentials are applied to obtain a current density of 300 A/m^2 approximately. Initial conditions for the problem are shown in Fig. 5.13.

Component	pK_a	pK_b	**Mobility** (m^2/Vs)	**Diffusivity** (m^2/s)	**Initial concentration**
Hydrochloric acid	-2.0	–	$7.91\ 10^{-8}$	$2.03\ 10^{-9}$	$5\ mM$
Tetraphenylborate	5.0	–	$1.8\ 10^{-8}$	$4.6\ 10^{-10}$	$5\ mM$
TRIS	–	8.08	$2.95\ 10^{-8}$	$7.6\ 10^{-10}$	$75\ mM$
Acetic acid	4.76	–	$4.2\ 10^{-8}$	$1.08\ 10^{-9}$	$380\ \mu M$
3-Phenylprop. ac.	4.66	–	$2.65\ 10^{-8}$	$6.8\ 10^{-10}$	$190\ \mu M$
O. G. carboxilic ac.	4.7	–	$4.3\ 10^{-8}$	$1.10\ 10^{-9}$	$1.9\ \mu M$
Fluorescein	6.7	–	$3.3\ 10^{-8}$	$4.2\ 10^{-10}$	$1.9\ \mu M$
Bodipy	5.0	–	$2.0\ 10^{-8}$	$5.1\ 10^{-10}$	$1.9\ \mu M$

Table 5.5: Physicochemical properties of buffer constituents and analytes from Bercovici et al. (2009).

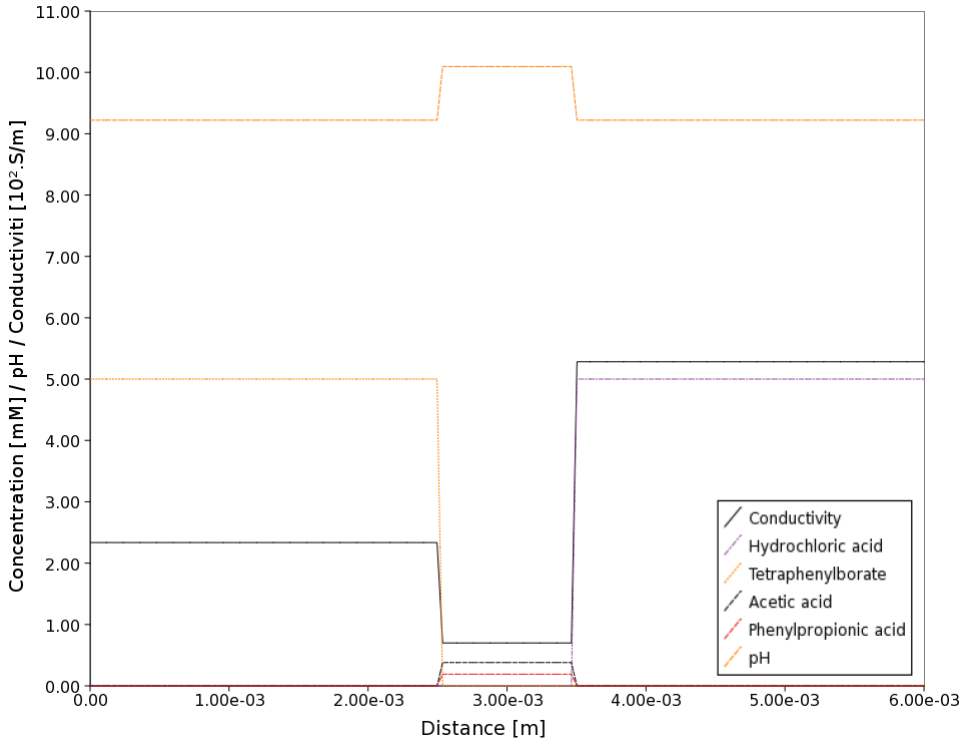

Figure 5.13: Initial conditions for pH, conductivity, sample, and buffer constituents.

In this example, and in the next one, adaptive mesh refinement (AMR) was employed. The need to use AMR in ITP simulations is due to the sharp variations of electric field between the leading electrolyte and sample, between

sample and the terminating electrolyte, and also, between sample components, due to the difference in conductivities. These sharpnesses in the electric field generate high local values for the migration of charged molecules, and in consequence, high values of the local Pèclet number (Eq. 4.12) with the consequent numerical instabilities (Donea and Huerta, 2003).

Adaptive mesh refinement has well known benefits when different length scales, great magnitude advective terms or discontinuities are present in the solution field, as it is the case. Among the different mesh adaptation techniques, region subdivisions (h-adaptation), has shown to be the most widely accepted in the scientific community when solving unsteady problems (Löhner and Baum, 1992; Berzins and Speares, 1997; Alauzet et al., 2007). Adaptive mesh refinement helps to reduce the numerical instabilities near high gradient regions and better define the aforementioned discontinuities without increasing significantly the computational costs. Adaptive mesh refinement tool used in this work was previously presented in solving compressible flow problems (Ríos Rodriguez et al., 2009).

The regions of the base mesh that need to be refined are selected based on the gradient's magnitude of the electrical conductivity field σ. All the elements whose gradient magnitude times its size is equal to or greater than a percentage of the maximum corresponding value for all the elements in the mesh are marked to be refined:

$$\gamma \leq \frac{\parallel \nabla_i \sigma \parallel \cdot h_i}{\max_{i=1,\ldots,Nel}(\parallel \nabla_i \sigma \parallel \cdot h_i)} \tag{5.1}$$

where γ is a constant set beforehand by the user, h_i is a measure of the element size (the longest edge is chosen in this case), $\parallel \nabla_i \sigma \parallel$ is the magnitude of the σ gradient computed for element-i and Nel is the number of elements in the mesh. The accurate choice of γ mostly depends on the user's experience and was set equal to 0.1 for both simulations. This is a classical procedure to tag the cells that need to be refined, commonly used in compressible flow problems (Berzins and Speares, 1997; Waltz, 2004; Young and Kwon, 2005). Figure 5.2.2 shows an example of five levels of refinement for regular quadrilateral elements. In this example, four levels of refinement were employed.

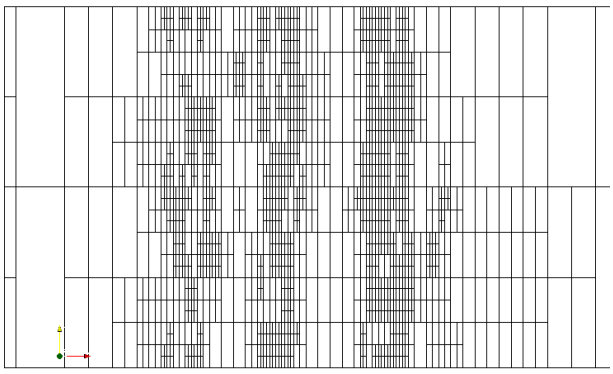

Figure 5.14: Detail of a refined quadrilateral mesh with five levels of refinement.

The initial uniform grid consist in 150 nodes in the longitudinal direction. In order to solve correctly this problem with a uniform mesh, at least 900 nodes are required (Bercovici et al., 2009). In the solution obtained here, the maximum number of points for the stationary state is 415 for the main direction. Stationary state is achieved after 5 seconds. Separation results as equivalent light intensity, analytes and markers distribution, and conductivity perfectly match with those reported experimentally by Khurana and Santiago (2008) and numerically by Bercovici et al. (2009). These results are shown in Fig.5.15.

5.2.3 Two-dimensional electrophoresis: ITP + CZE

In this example a two-dimensional electrophoresis (2DE) experimental assay from the literature is simulated. 2DE separations consist of two independent mechanisms that are employed sequentially (O'Farrell, 1975). Each mechanism provides a selective relative displacement between analytes based on different properties of such analytes. The separation efficiency is estimated as the product of the independent efficiency of each method, provided the methods are uncoupled (orthogonality). Particularly, in this case the two mechanisms employed are ITP and CZE.

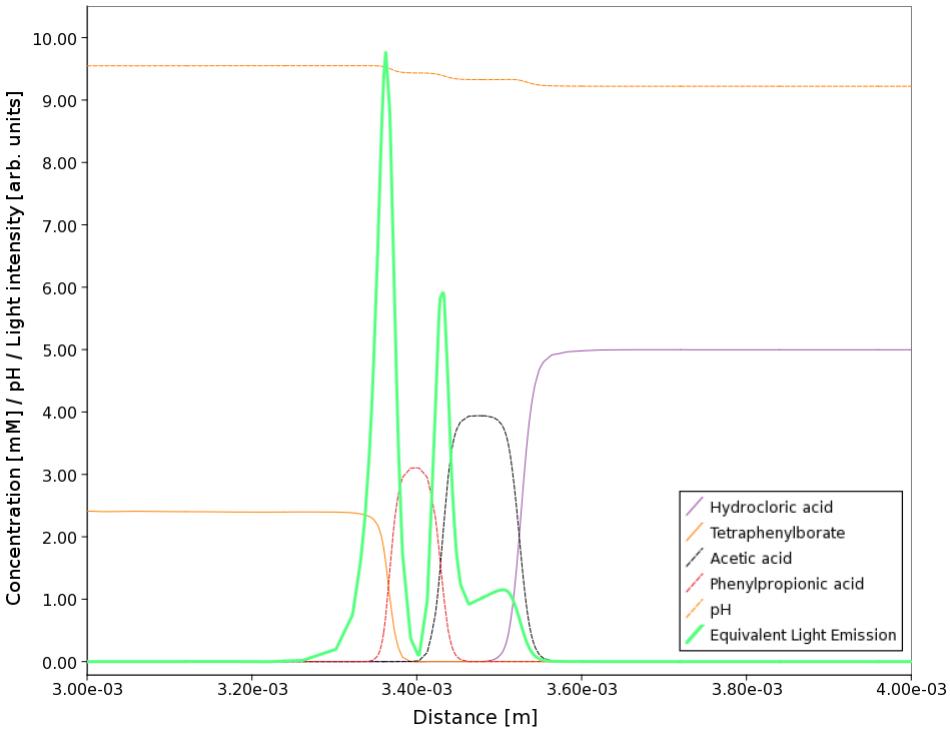

(a) Sample, electrolytes distribution and equivalent light signal.

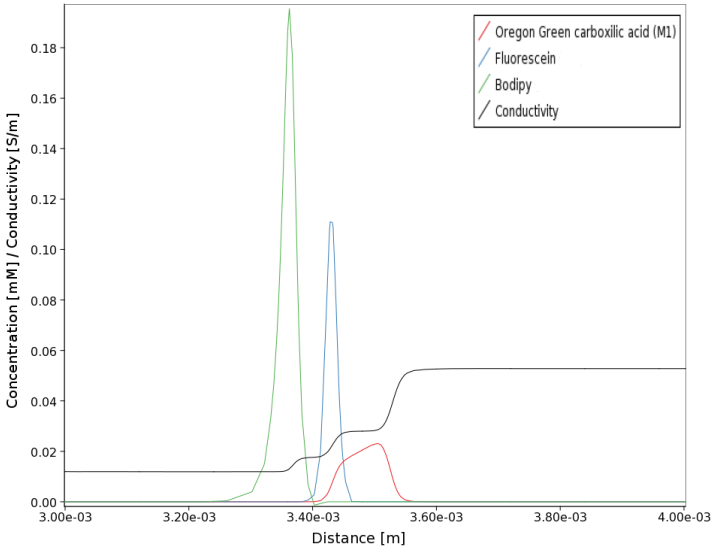

(b) Markers concentration and conductivity.

Figure 5.15: Stationary state results for the capillary ITP.

Simulations are based on a relevant experimental work of Herr et al. (2003), which represents one of the first successful attempts to carry out 2DE in LOC. The chip consists in a cross-shape network ($28 \times 0.2 \times 0.02$ mm^3, for each branch), were in the channel parallel to the x-axis ITP is carried out, and then in an asynchronous process the CZE is developed in the perpendicular channel. Geometry, conductivity, and details about the refined mesh are shown in Fig. 5.16. In this assay three proteins are separated: FITC-Ovoalbumin, FITC-Dextran, and recombinant green fluorescent protein (GFP). Phosphoric acid is used as leading electrolyte and NaOH as terminating electrolyte. In this case, the buffer also contains an ampholyte solution to improve the separation. Due to this fact, the first separation technique is a combination of ITP and IEF with characteristics of both. Physicochemical properties and initial concentration of buffer and sample components are listed in Table 5.6.

In this case, AMR was also used. The function to determine the elements to refine is a weighted combination of conductivity, like in the previous example, and sample concentration, which allows the AMR algorithm to follow the sample plugs, improving numerical stability during separation. In this example, three levels of refinement were used.

After focusing specie, when a particular focused band arrive at the intersection, voltages are switched in order to inject this sample plug into the vertical channel to carry out the CZE. This asynchronous process asserts the orthogonality of the methods employed. Sample distributions at different values of time are shown in Fig. 5.17. There exists uncertainties about the exact acid-base behaviour of analytes because they are not fully provided by the literature, then, values of dissociation points were approximated. Due to this, the experiment lacks on complete reproducibility, and switching voltage times were adapted in order to achieve successful separations. Despite of these facts, separation results match with the experiment (see Fig. 5.18), and also these results agree with the theoretical predictions.

Component	pK_a	pK_b	**Mobility** (m^2/Vs)	**Diffusivity** (m^2/s)	**Initial concentration**
FITC-Ovo	7.01	8.87	$5.50\ 10^{-8}$	$1.421\ 10^{-9}$	0.2 mM
FITC-Dextran	4.0	6.0	$1.08\ 10^{-8}$	$2.58\ 10^{-10}$	0.2 mM
GFP	5.5	7.5	$1.35\ 10^{-8}$	$3.489\ 10^{-10}$	0.2 mM
Phosphoric acid	2.1	7.2	$6.14\ 10^{-8}$	$1.58\ 10^{-9}$	20.0 mM
NaOH	13.7	–	$5.19\ 10^{-8}$	$1.34\ 10^{-9}$	40.0 mM
Ampholyte 1	2.825	3.525	$3.0\ 10^{-8}$	$7.75\ 10^{-10}$	2.0 mM
Ampholyte 2	3.175	3.875	$3.0\ 10^{-8}$	$7.75\ 10^{-10}$	2.0 mM
Ampholyte 3	3.525	4.225	$3.0\ 10^{-8}$	$7.75\ 10^{-10}$	2.0 mM
Ampholyte 4	3.875	4.575	$3.0\ 10^{-8}$	$7.75\ 10^{-10}$	2.0 mM
Ampholyte 5	4.225	4.925	$3.0\ 10^{-8}$	$7.75\ 10^{-10}$	2.0 mM
Ampholyte 6	4.575	5.275	$3.0\ 10^{-8}$	$7.75\ 10^{-10}$	2.0 mM
Ampholyte 7	4.925	5.625	$3.0\ 10^{-8}$	$7.75\ 10^{-10}$	2.0 mM
Ampholyte 8	5.275	5.975	$3.0\ 10^{-8}$	$7.75\ 10^{-10}$	2.0 mM
Ampholyte 9	5.625	6.325	$3.0\ 10^{-8}$	$7.75\ 10^{-10}$	2.0 mM
Ampholyte 10	5.975	6.675	$3.0\ 10^{-8}$	$7.75\ 10^{-10}$	2.0 mM
Ampholyte 11	6.325	7.025	$3.0\ 10^{-8}$	$7.75\ 10^{-10}$	2.0 mM
Ampholyte 12	6.675	7.375	$3.0\ 10^{-8}$	$7.75\ 10^{-10}$	2.0 mM
Ampholyte 13	7.025	7.725	$3.0\ 10^{-8}$	$7.75\ 10^{-10}$	2.0 mM
Ampholyte 14	7.375	8.075	$3.0\ 10^{-8}$	$7.75\ 10^{-10}$	2.0 mM
Ampholyte 15	7.725	8.425	$3.0\ 10^{-8}$	$7.75\ 10^{-10}$	2.0 mM
Ampholyte 16	8.075	8.775	$3.0\ 10^{-8}$	$7.75\ 10^{-10}$	2.0 mM
Ampholyte 17	8.425	9.125	$3.0\ 10^{-8}$	$7.75\ 10^{-10}$	2.0 mM
Ampholyte 18	8.775	9.475	$3.0\ 10^{-8}$	$7.75\ 10^{-10}$	2.0 mM
Ampholyte 19	9.125	9.825	$3.0\ 10^{-8}$	$7.75\ 10^{-10}$	2.0 mM
Ampholyte 20	9.475	10.175	$3.0\ 10^{-8}$	$7.75\ 10^{-10}$	2.0 mM

Table 5.6: Physicochemical properties of buffer constituents and analytes.

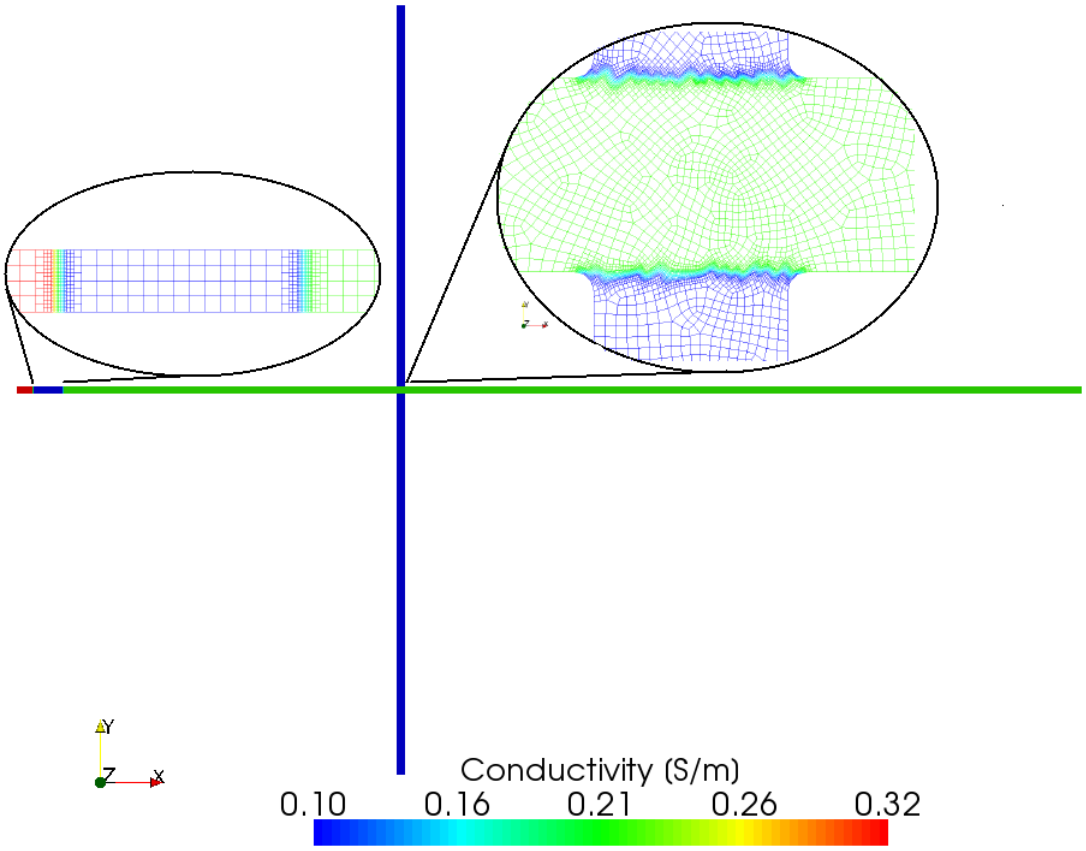

Figure 5.16: Initial conditions for conductivity and mesh refinement details.

5.2.4 Two-dimensional electrophoresis: FFIEF + CZE

In this example another 2DE simulation is presented. In this case, separation mechanisms involved are IEF and CZE. Such mechanisms satisfy orthogonality and have been extensively employed in the analysis of complex protein samples in conventional devices (Tia and Herr, 2009). In this case the IEF is performed as FFIEF. As was described in section 1.3.2, FFIEF is a derivative of FFE, a classical technique in which an electric field is applied perpendicularly to a flowing sample solution, then analytes are separated electrophoretically in a continuous flow (Xu et al., 2005; Kohlheyer et al., 2008; Turgeon and Bowser, 2009). In a FFIEF assay, a pH gradient is generated across the channel in order to focus analytes according to their pI, like in the IEF process, but setting a

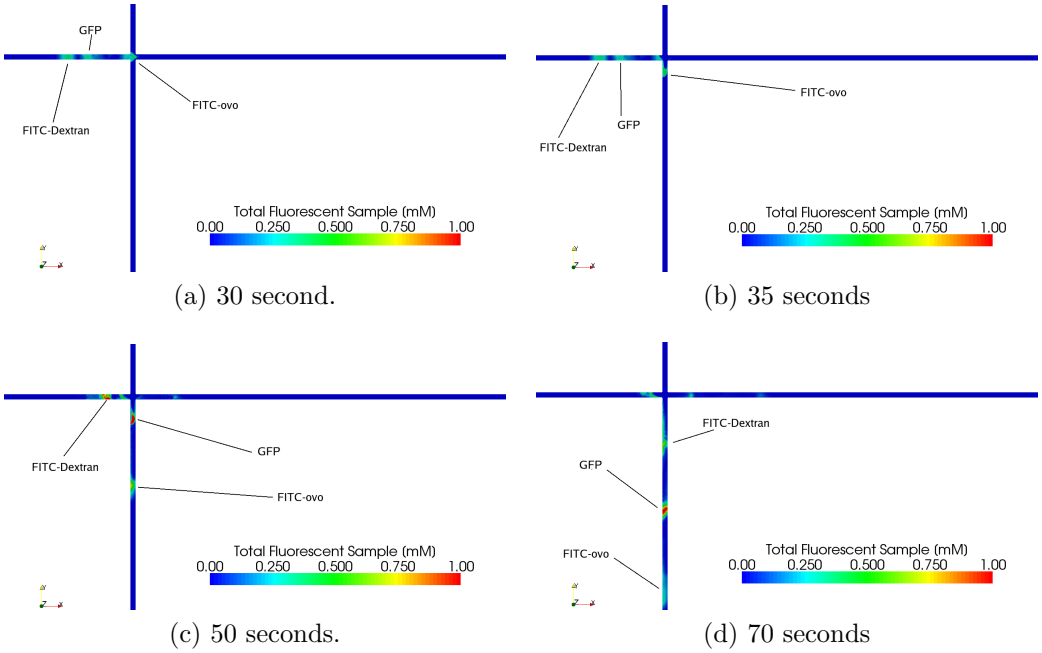

(a) 30 second. (b) 35 seconds

(c) 50 seconds. (d) 70 seconds

Figure 5.17: Total sample concentration at different times.

continuous flow along the channel, like in FFE.

Here, 2DE separation involving continuous FFIEF and CZE is simulated. For this purpose, a microfluidic chip was designed following a FFIEF device recently published (Kohlheyer et al., 2006). The geometry of the problem domain is presented in Fig. 5.19. FFIEF is carried out in the FFIEF channel (10 x 3500 x 10000 μm^3), then samples flow through three secondary channels (10 x 600 x 10000 μm^3), and finally CZE is developed in the CZE channel (10 x 1000 x 50000 μm^3). A main concern in two-dimensional separations is the uncoupling of the processes, as mentioned above. This uncoupling normally requires discontinuous operation in order to avoid sample dispersions, mainly due to the geometry of turns or buffer heterogeneity (Tia and Herr, 2009). In this case we adopt a continuous system, in which the mentioned effects do not influence the separation performance because the number of analytes is very low compared with theoretical peak capacity of the device (Herr et al., 2003). Also values of the electric field and conductivity gradients are sufficiently low to avoid flow instabilities (Posner and Santiago, 2006).

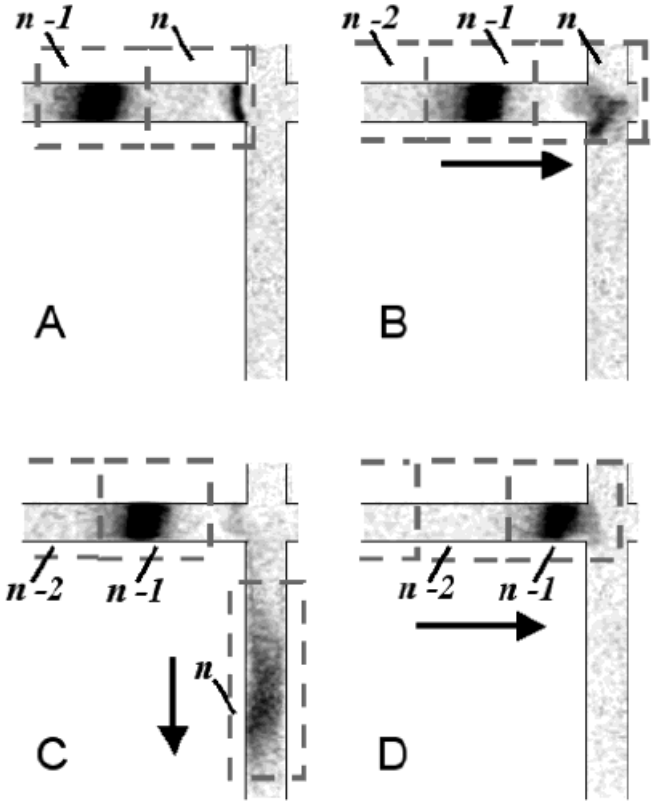

Figure 5.18: CCD images during specie sampling in the original work of Herr et al. (2003).© 2003 ACS publications. Reproduced with permission.

The electric potential at the initial state is shown in Fig. 5.19. The applied electric potentials (Table 5.7) are fixed during the operation to provide the system with: a transverse electric field in the FFIEF channel, an axial electric field in the CZE channel, and EOF in the secondary and CZE channels. The fluid flow problem was solved by using Eqs. 3.18, 3.19 and 3.13, and boundary conditions summarized in Table 5.7. ζ-potential is set to 25 mV. Streamlines and velocity magnitude are shown in Fig. 5.20.

The pH gradient for FFIEF is established by focusing twenty ampholytes between two sheath flows of anolyte and catholyte, at pH 5.0 and 6.21, respectively. Physicochemical properties of buffer components are listed in Table 5.8. Ampholytes 1 to 6 were injected continuously from inlet 1, ampholytes 7 to 14 from inlet 2, and ampholytes 15 to 20 from inlet 3 with a concentration of 1.0 mM. A more concentrated buffer (100 mM) at pH 4 is injected con-

tinuously from inlet 4. When ampholytes reach the CZE channel, they dilute into the buffer preserving pH 4. Stationary conditions are reached after 120 s, where a linear-like pH gradient is formed (Fig. 5.21).

The separation of a mixture of 9 amphoteric compounds was simulated. Physicochemical properties of these analytes (see Table 5.9) were selected considering the mobilities and pIs of human aminoacids. All analytes were injected during 1.0 s from inlet 2 with a concentration of 0.1 mM. Complete separation is achieved after 700 seconds. Analyte distributions during separation processes at different times are shown in Fig. 5.22.

A two-dimensional map of the separation is obtained from the information provided by the four hypothetical detectors shown in Fig. 5.19. Detector number 4 (Fig. 5.23d) acquires the entire output signal, which is sectioned in three parts. These parts are obtained taking into account signals from detectors 1 to 3 (Fig. 5.23a to 5.23c respectively), and assuming that areas under graphics are conserved. The first part of the signal has the same area that Fig. 5.23a and is assigned to the first pH range (5 to 5.4). The other parts of the signal are assigned to second and third pH ranges,respectively (5.4 to 5.8 and 5.8 to 6.2). The resulting plot is shown in Fig.5.24. It is observed that the results of the numerical model can be easily presented in the graphic format that is customarily used in experiments of two-dimensional electrophoresis (Tia and Herr, 2009).

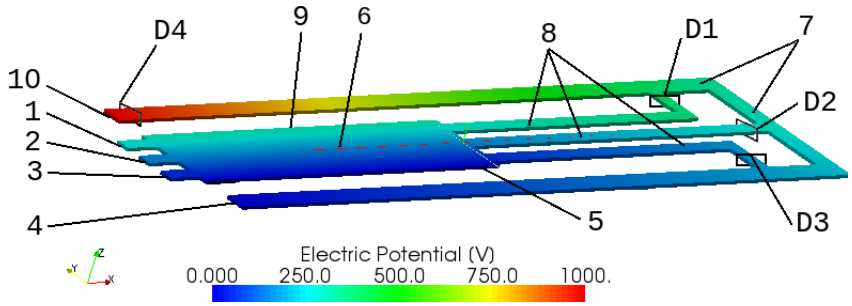

Figure 5.19: Geometry and electric potential distribution for initial state. **1**, inlet 1; **2**, inlet 2; **3**, inlet 3; **4**, inlet 4 (CZE buffer inlet); **5**, basic sheath flow; **6**, FFIEF channel; **7**, CZE channels; **8**, secondary channels; **9**, acidic sheath flow; **10**, outlet. **D1, D2, D3** and **D4**, are the locations for hypothetical detectors.

Boundary section	Boundary condition	Value	Units
basic sheath flow	electric potential	300	V
acidic sheath flow	electric potential	0	V
inlet 4	electric potential	0	V
outlet	electric potential	1000	V
inlet 1 to 4	pressure	0	Pa
inlet 1 to 4	tangent velocity	0	m/s
secondary channels	slip velocity	$-\frac{\epsilon\zeta}{\mu}\nabla\phi$	m/s
CZE channels	slip velocity	$-\frac{\epsilon\zeta}{\mu}\nabla\phi$	m/s
basic sheath flow	normal velocity	0	m/s
acidic sheath flow	normal velocity	0	m/s
outlet	tangent velocity	0	m/s

Table 5.7: Boundary conditions for the electric field and fluid flow problems.

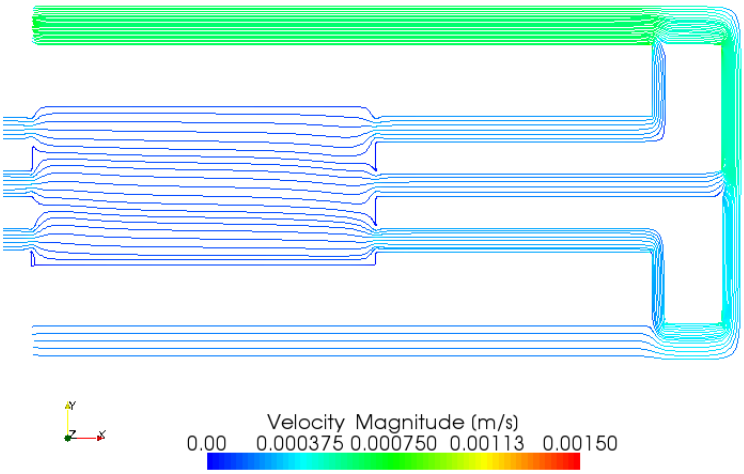

Figure 5.20: Streamlines and velocity magnitude. Geometry is scaled by 2 in the y-axis for better visualization.

Ampholyte	pK_a	pK_b	pI	**Mobility** (m^2/Vs)
1	4.90	5.30	5.10	$3.0\ 10^{-8}$
2	4.95	5.35	5.15	$3.0\ 10^{-8}$
3	5.00	5.40	5.20	$3.0\ 10^{-8}$
4	5.05	5.45	5.25	$3.0\ 10^{-8}$
5	5.10	5.50	5.30	$3.0\ 10^{-8}$
6	5.15	5.55	5.35	$3.0\ 10^{-8}$
7	5.20	5.60	5.40	$3.0\ 10^{-8}$
8	5.25	5.65	5.45	$3.0\ 10^{-8}$
9	5.30	5.70	5.50	$3.0\ 10^{-8}$
10	5.35	5.75	5.55	$3.0\ 10^{-8}$
11	5.40	5.80	5.60	$3.0\ 10^{-8}$
12	5.45	5.85	5.65	$3.0\ 10^{-8}$
13	5.50	5.90	5.70	$3.0\ 10^{-8}$
14	5.55	5.95	5.75	$3.0\ 10^{-8}$
15	5.60	6.00	5.80	$3.0\ 10^{-8}$
16	5.65	6.05	5.85	$3.0\ 10^{-8}$
17	5.70	6.10	5.90	$3.0\ 10^{-8}$
18	5.75	6.15	5.95	$3.0\ 10^{-8}$
19	5.80	6.20	6.00	$3.0\ 10^{-8}$
20	5.85	6.25	6.05	$3.0\ 10^{-8}$

Table 5.8: Physicochemical properties of buffer constituents used in example 5.2.4.

Analyte	pK_a	pK_b	pI	**Mobility** (m^2/Vs)	**Diffusivity** (m^2/s)
1	3.22	6.88	5.09	$2.64\ 10^{-8}$	$6.82\ 10^{-10}$
2	3.65	6.72	5.18	$2.84\ 10^{-8}$	$7.34\ 10^{-10}$
3	3.70	6.80	5.25	$3.84\ 10^{-8}$	$9.92\ 10^{-10}$
4	4.12	7.03	5.57	$2.24\ 10^{-8}$	$5.79\ 10^{-10}$
5	3.96	7.26	5.61	$3.18\ 10^{-8}$	$8.22\ 10^{-10}$
6	4.18	7.26	5.72	$2.45\ 10^{-8}$	$6.83\ 10^{-10}$
7	4.17	7.30	5.73	$2.17\ 10^{-8}$	$5.60\ 10^{-10}$
8	4.32	7.59	5.95	$2.41\ 10^{-8}$	$6.22\ 10^{-10}$
9	4.33	7.58	5.95	$2.24\ 10^{-8}$	$5.79\ 10^{-10}$

Table 5.9: Physicochemical properties of analyte constituents used in example 5.2.4.

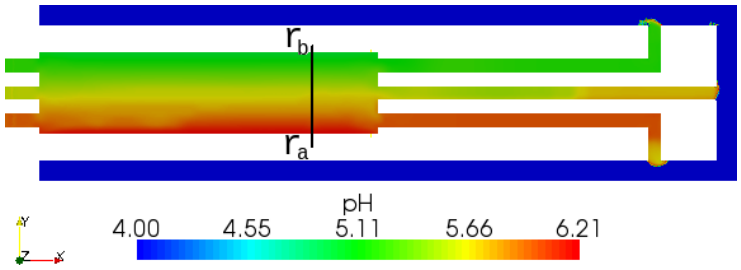

(a) pH in stationary conditions at $z = 5.0$ μm.

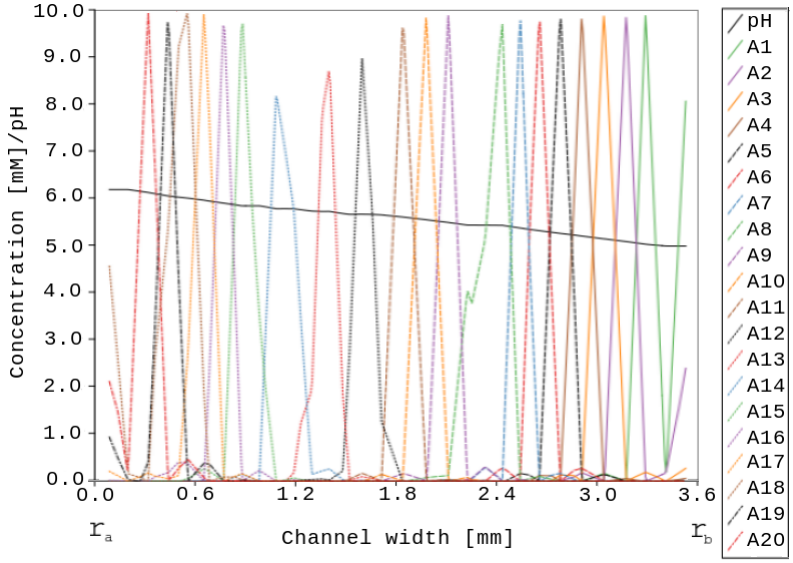

(b) Ampholyte concentration and pH across the line $r_a - r_b$ at $x = 8.0$ mm; z $= 5.0$ μm.

Figure 5.21: pH and ampholyte concentrations in stationary conditions.

Redesign of the device

The device previously presented allows to perform 2DE separations, but it has some improvable aspects. These aspects are related to the time consumption, sample dispersion, and cross-talking. Respect the time consuming, the path of the samples to reach the detector is certainly large (50 mm), and it could be reduced by suppressing the secondary channels. With respect to the sample dispersion, one of the key are the 90° turns, that, in a more optimal design should be avoided. Finally, the fact that the CZE is performed in a single channel allows the possibility of overlapping between FFIEF bands depending on the electrophoretic behaviour of the samples. One important issue would

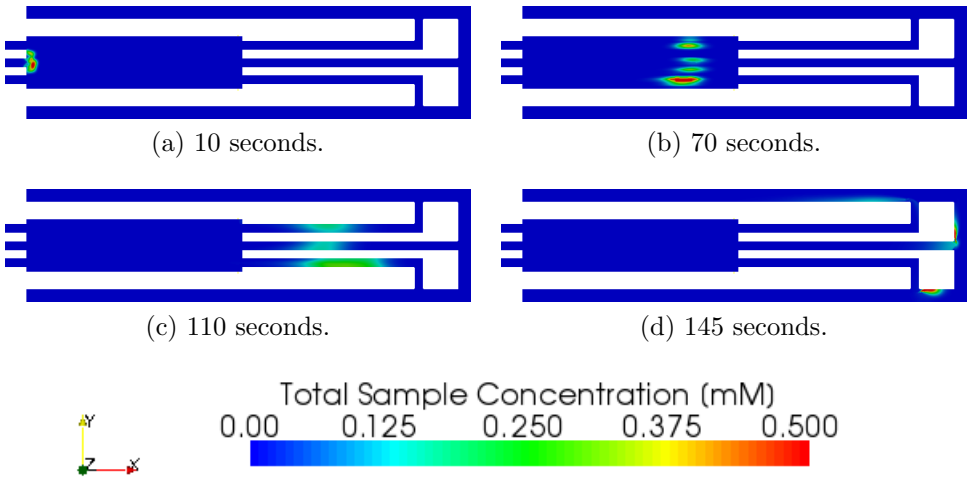

(a) 10 seconds. (b) 70 seconds.

(c) 110 seconds. (d) 145 seconds.

Figure 5.22: Total sample distribution at different times.

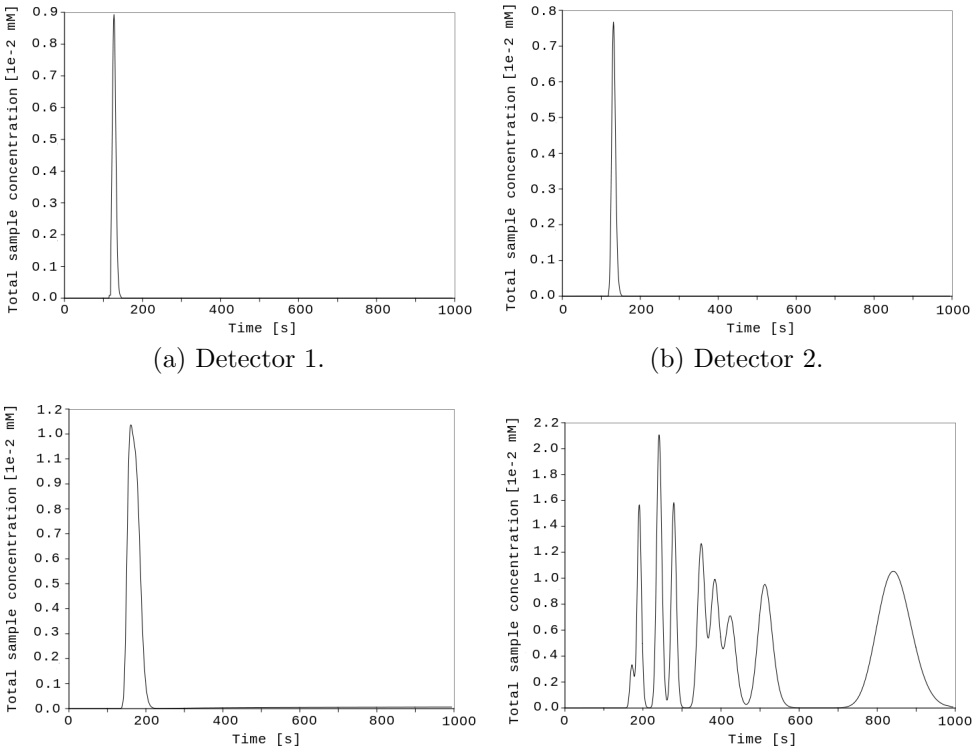

(a) Detector 1. (b) Detector 2.

(c) Detector 3. (d) Detector 4.

Figure 5.23: Detector signals along time that enable to make the two-dimensional map of the separation.

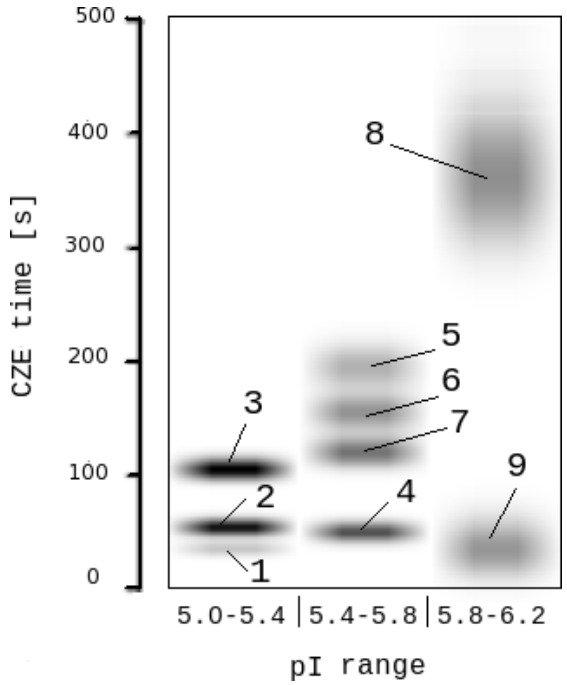

Figure 5.24: Gel-like plot of the two-dimensional separation (IEF+CZE). Numbers 1 to 9 refer to analytes using denominations employed in Table 5.9.

be perform CZE in independent channels with the drawback of implement multiple detection systems.

Taking into account the aspects previously listed, a new design for a 2DE numerical prototype was proposed. The geometry of the new design is presented in Fig. 5.25 with the electric potential distribution. FFIEF is carried out in the FFIEF channel (10 x 3500 x 7000 μm^3), then samples flow through five CZE channels (10 x 1000 x 16000 μm^3) completing the separation.

The applied electric potentials are fixed during the operation to provide the system with: a transverse electric field in the FFIEF channel, an axial electric field in the CZE channel, and EOF in the channels in the right side.

Following a similar operation that in the previous design, the pH gradient for FFIEF is established by focusing twenty ampholytes in a wider range: $4.9 \leqslant pI \leqslant 8.03$, between two sheath flows of anolyte and catholyte, at pH 4.8 and 8.2, respectively. Concentration of ampholytes was 1.0 mM. The resulting linear-like pH gradient is shown in Fig. 5.26. A concentrated buffer (100 mM,

pH 10) is continuously injected from the inlet at the right, and is injected in the CZE channels in order to carry out the CZE at a constant pH.

To test the new design, the separation of a mixture of 10 amphoteric compounds (Table 5.9) was simulated, taking into account a broader range for pI's and mobilities. Sample distributions at different times during the processes are shown in Fig. 5.27. Also, a two-dimensional map of the separation is shown in Fig. 5.28.

Analyte	pK_a	pK_b	pI	**Mobility** (m^2/Vs)	**Diffusivity** (m^2/s)
1	1.97	6.92	4.45	$3.84\ 10^{-8}$	$8.55\ 10^{-10}$
2	2.27	7.37	4.82	$2.24\ 10^{-8}$	$7.87\ 10^{-10}$
3	3.51	7.70	5.61	$2.15\ 10^{-8}$	$6.85\ 10^{-10}$
4	3.80	8.05	5.92	$2.94\ 10^{-8}$	$7.38\ 10^{-10}$
5	4.15	8.30	6.22	$2.56\ 10^{-8}$	$6.98\ 10^{-10}$
6	4.47	8.60	6.53	$2.24\ 10^{-8}$	$8.04\ 10^{-10}$
7	4.74	8.92	6.83	$3.18\ 10^{-8}$	$7.49\ 10^{-10}$
8	5.08	9.92	7.51	$2.84\ 10^{-8}$	$7.35\ 10^{-10}$
9	5.29	9.71	7.49	$3.39\ 10^{-8}$	$8.48\ 10^{-10}$
10	5.57	10.01	7.89	$2.41\ 10^{-8}$	$5.79\ 10^{-10}$

Table 5.10: Physicochemical properties of analyte constituents.

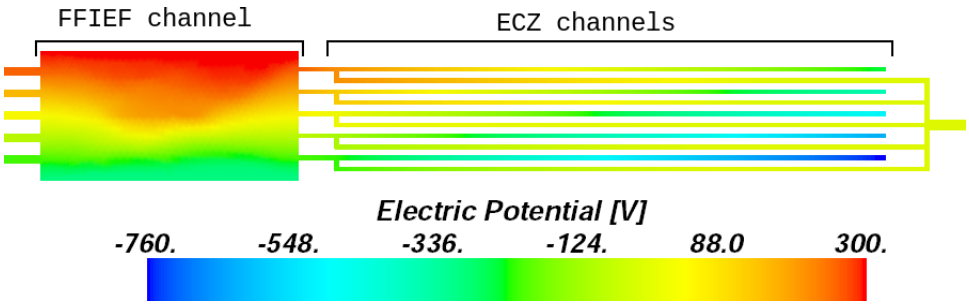

Figure 5.25: Electric potential distribution.

The new design allows to improve some aspects of the previous prototype as the total assay time, that reduces to 180 seconds, and the crosstalking possibility between FFIEF bands notably decreases. Despite of the fact that samples move in a continuous path-line (without important turns) dispersion

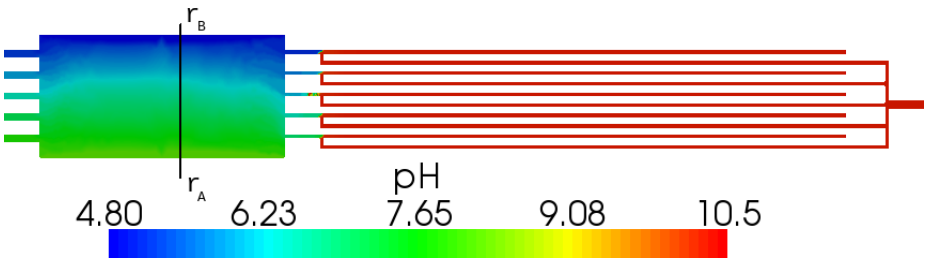

(a)

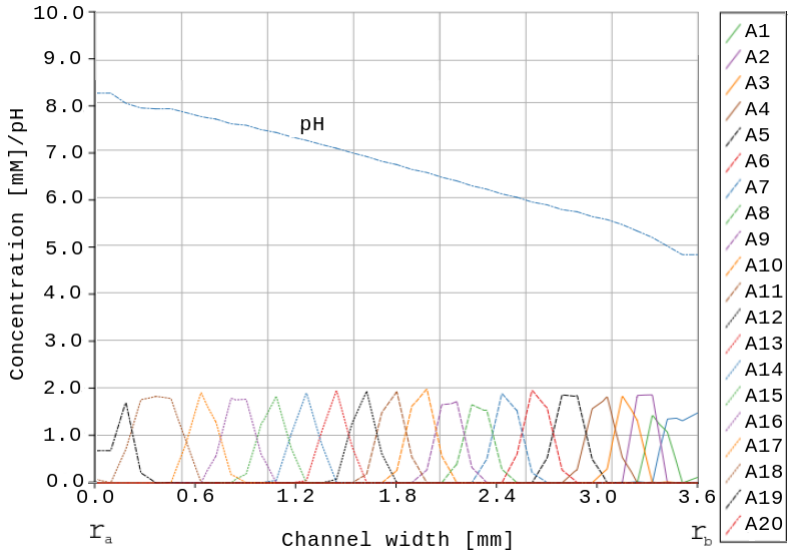

(b)

Figure 5.26: Initial pH in the whole domain and across the FFIEF section.

arises. These dispersions are more important for those specie that are focused near the catholyte and anolyte flows, or when the focusing area shares two streamlines that enters in different CZE channels. In this cases samples move along curved streamlines, and its effects are similar to those shown for turns. These effects can be observed in samples 2, 4, 6 and 10.

5.2.5 Microchip Immunoassay

In this example a on-chip western blotting assay recently published by Tia et al. (2010) is simulated. Western blotting comprises a suite of immunological techniques for the identification of a wide variety of molecules in complex

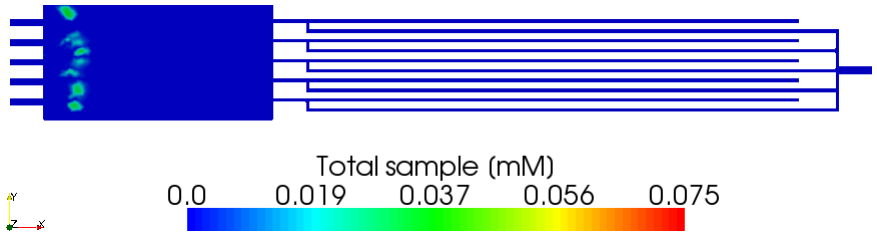

(a) 20 seconds.

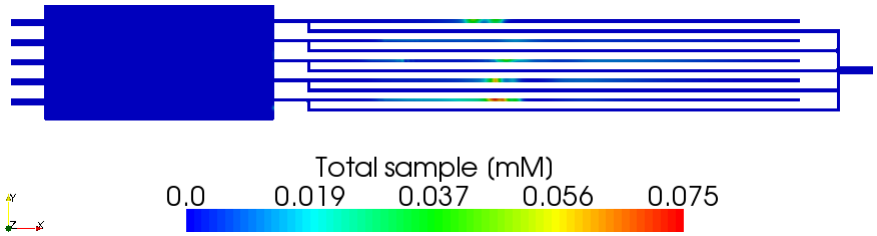

(b) 65 seconds.

Figure 5.27: Total sample distribution at different times.

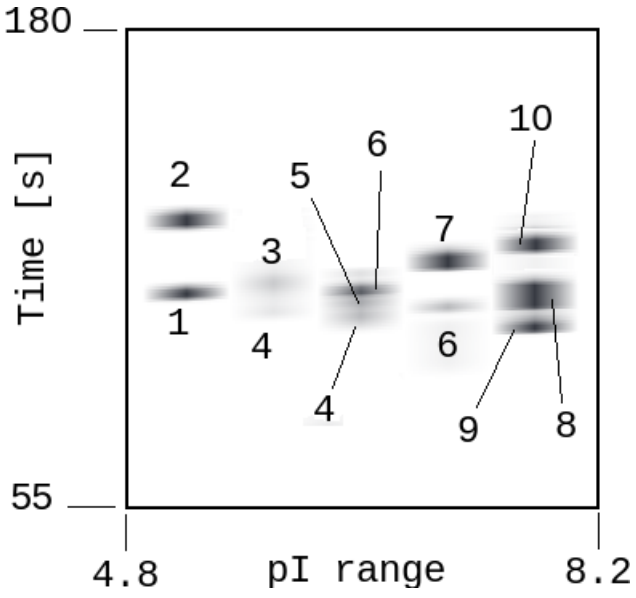

Figure 5.28: Two dimensional map for the separation.

biological backgrounds. The classical bench-top western blotting has some drawbacks as time consumption (hours or days), semi-quantitative detection and low reproducibility. In order to surmount these shortcomings, this on-chip version for western blotting was presented. The chip enables to develop the complete assay (separation, transfer and blotting) in two minutes, and also, improving significantly the reproducibility.

The chip consist in a rectangular chamber ($1600 \times 1000 \times 20\ \mu m^3$) divided in two regions. The first regions corresponds to the separation region, where an initial polyacrilamide gel electrophoretic separation is developed. The second region is divided in bands, which are functionalized with different antibodies. This distribution can be observed in Fig. 5.29.

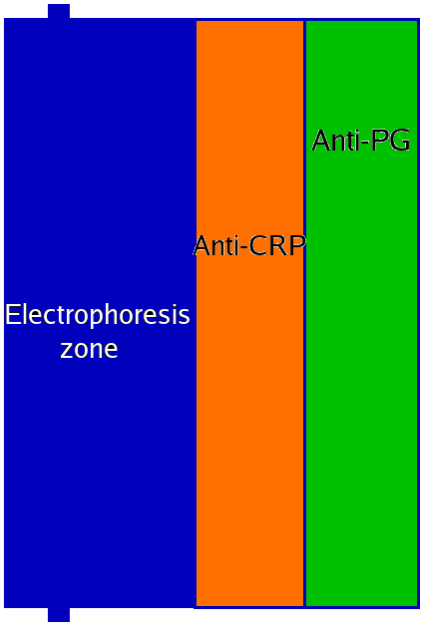

Figure 5.29: Antibody localization in the device.

Particularly, the simulated assay consist in the separation of three fluorescent labeled proteins. These proteins are C-reactive protein (CRP), protein G (PG) and bovine serum albumin (BSA). There are fixed antibodies for the first two proteins, as is indicated in Fig. 5.29, and BSA is added to accomplished the biological sample matrix and verify the specificity of the assay. The assay is performed with a TRIS-glycine buffer. Physicochemical properties used in

this simulation for buffer and analytes are listed in Table 5.11. The capture efficiency was set as 95 %.

Component	*pI*	**Mobility** (m^2/Vs)	**Diffusivity** (m^2/s)	**Initial concentration**
BSA	4.70	3.70 10^{-9}	6.38 10^{-11}	300 mM
PG	4.81	3.34 10^{-9}	8.65 10^{-11}	300 mM
CRP	7.40	2.46 10^{-9}	9.50 10^{-11}	600 mM
TRIS	–	2.95 10^{-8}	4.08 10^{-10}	25 mM
Glycine	6.97	3.74 10^{-8}	6.39 10^{-10}	192 mM

Table 5.11: Physicochemical properties of buffer constituents and analytes.

Samples are injected and separated electrophoretically by applying an electric field of 150 V/m along the electrophoretic region. Results for the separation process are shown in Fig. 5.30. After separation is completed, the transfer process is developed by applying transversely an electric field of 50 V/m. Transfer and capturing processes results are illustrated in Fig. 5.32. From top to bottom, can be seen CRP, captured at the band on the right, PG captured at the region on the middle, and BSA, that leaves the chamber without binding in any zone.

The simulation results agree with the experiments in sample distribution and binding rates as is shown in Fig. 5.31. Experiment times differ from those of simulation due to the uncertainties in the real value of analytes mobilities in a polyacrilamide gel medium at the concentration of gel and pH specified. The bibliographic source to approximate these values is the work of Dunker and Rueckert (1969) in which some relations between molecular weight and mobilities are listed, but the conditions for gel concentration and pH are not matched exactly.

5.2.6 Multienzyme electrokinetically driven assay

In this example an enzymatic electrokinetically driven assay is performed. Simulation is based on the work of Atalay et al. (2009) in which three different sugars are detected using a double-T LOC as is shown in Fig. 5.33.

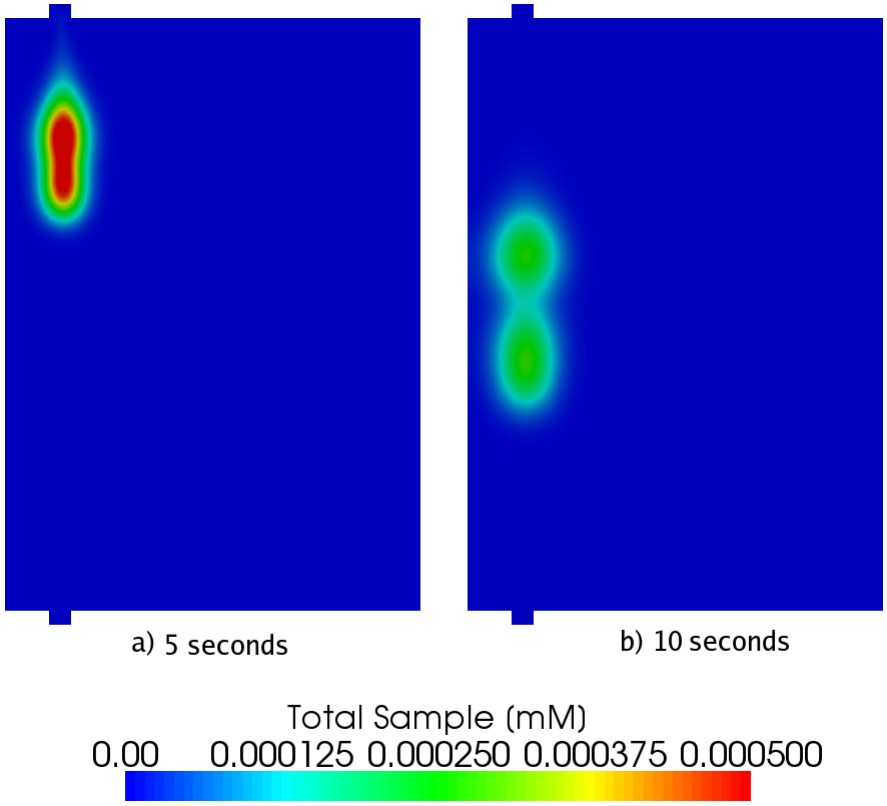

Figure 5.30: Total sample distribution for the electrophoretic separation at 5 and 10 seconds.

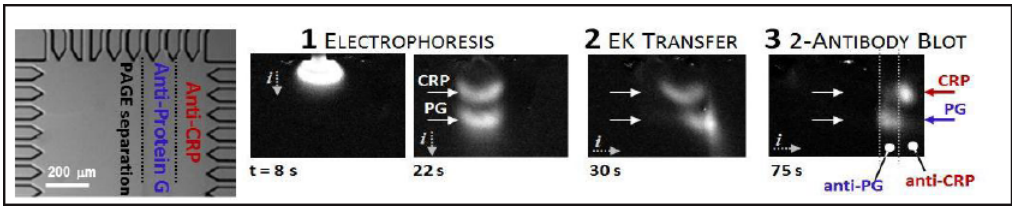

Figure 5.31: CCD images for specie sampling in the original work of Tia et al. (2010).© 2010 CBMS publications. Reproduced with permission.

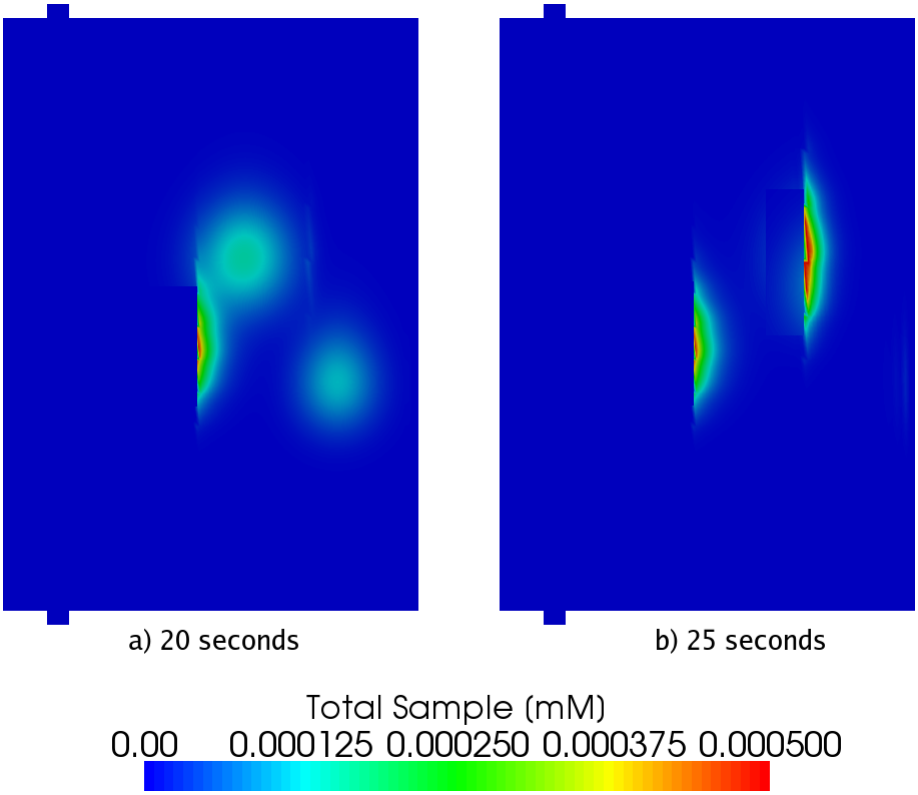

Figure 5.32: Total sample distribution for immune capture at 20 and 25 seconds.

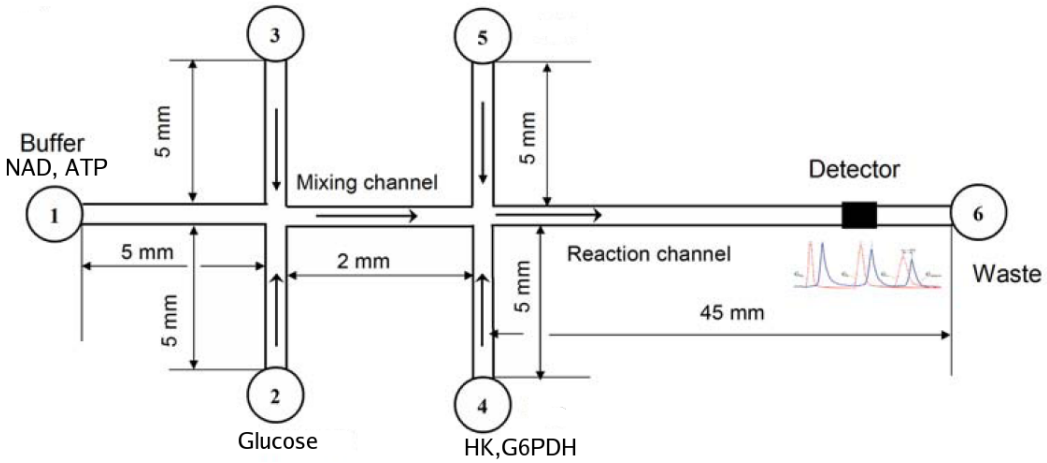

Figure 5.33: Schematic diagram of the simulated LOC. Modified from Atalay et al. (2009).

Detection of sugars is an important task in clinical diagnosis and food industry. Due to the high complexity of sample matrices, enzymatic assays are necessary to improve the specificity of analysis avoiding interference from other matrix component (Vermeir et al., 2007).

Atalay et al. performed an indirect detection of sugars by detecting fluorescent NADH. In this example, only one of the three detection (detection of glucose) is simulated. The use of NADH as indirect marker of the glucose concentration (c_G) is based on the following double enzyme reaction scheme, that involves hexokinase (HK) and glucose-6-phosphate dehydrogenase (G6PDH)

$$\text{D-Glucose} + \text{ATP} \xrightarrow{HK} \text{D-Glucose-6-Phosphate } (G6P) + \text{ADP} \tag{5.2}$$

$$\text{G6P} + \text{NAD}^+ \xrightarrow{G6PDH} \text{D-Gluconate-6-Phosphate} + \text{NADH} + \text{H}^+ \tag{5.3}$$

Following the treatment shown in section 3.2.4, the reaction terms for the mass transport equation (Eq. 3.28), are

$$\begin{aligned} r_G = r_{ATP} = r_1;\ r_{ADP} = -r_1; \\ r_{G6P} = r_2 - r_1; \\ r_{NAD^+} = r_2; r_{NADH} = -r_2 \end{aligned} \tag{5.4}$$

where

$$r_1 = \frac{k_{cat,HK_g}\ c_{HK}\ c_G\ c_{ATP}}{K_{S,G}\ K_{M,HK_g} + K_{M,HK_g}\ c_{ATP} + K_{M,HK_{ATP}}\ c_G + c_G\ c_{ATP}} \tag{5.5}$$

$$r_2 = \frac{k_{cat,G6P}\ c_{G6PDH}\ c_{NAD^+}\ c_{G6P}}{K_{S,G6P}\ K_{M,G6P} + K_{M,G6P}\ c_{NAD^+} + K_{M,NAD^+}\ c_{G6P} + c_{NAD^+}\ c_{G6P}} \tag{5.6}$$

The values of the reaction constants and the diffusion coefficients for the analyte, enzymes and products are listed in Table 5.12. The only charged specie in the considered sample matrix is NAD^+ and its mobility is 1.27 10^{-8} m^2/Vs. Transport of the rest of molecules is produced by advection (driven by EOF)

and diffusion.

Enzyme	**Diffusivity** (m^2/s)	**Substrate**	K_M (μM)	K_S (μM)	K_{cat} (s^{-1})	**Diffusivity** (m^2/s)
HK	$8.0\ 10^{-11}$	Glucose	130	130	15	$6.4\ 10^{-10}$
		ATP	100			$4.4\ 10^{-10}$
G6PDH	$6.5\ 10^{-11}$	G6P	48	890	35	$6.5\ 10^{-10}$
		NAD^+	120			$3.5\ 10^{-10}$

Table 5.12: Reaction constants and diffusion coefficients of analyte, enzymes and products.

The operation of the assay is entirely driven by EOF. In Table 5.13, applied electric potentials and the duration for each analysis step are shown. Times are estimated starting when samples arrive to the principal channel. The ζ-potential considered is -60 mV. Results of the injection process are shown for buffer, substrate and enzymes in Figs. 5.34a, 5.34b and 5.34c, respectively.

Process	**Electric Potential [V]**						**Time**
	1	2	3	4	5	6	(s)
Glucose injection	1237.5	1237.5	1175.0	1125.0	1125.0	0	1.0
Enzyme injection	1230.0	1155.0	1155.0	1175.0	1125.0	0	2.5
Separation	1300.0	1175.0	1175.0	1125.0	1125.0	0	35.0

Table 5.13: Electric potentials applied at the reservoirs and switching time for each process.

After the injection of substrate and enzymes to the main channel, reactions take place and concentrations of intermediate products (as G6P) and final products (as NADH) rise. Samples distribution, such as, substrate, intermediate product, enzyme and final product, are shown at two different times in Figs. 5.35 and 5.36. Concentration profile of NADH along time agree with

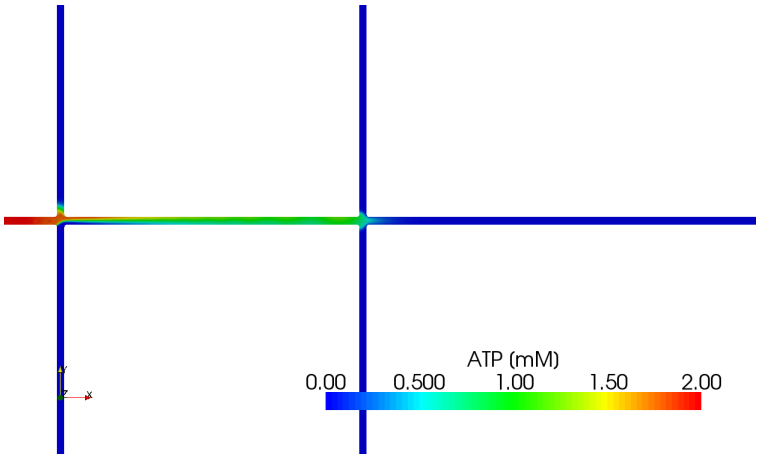

(a) Buffer at 2 seconds.

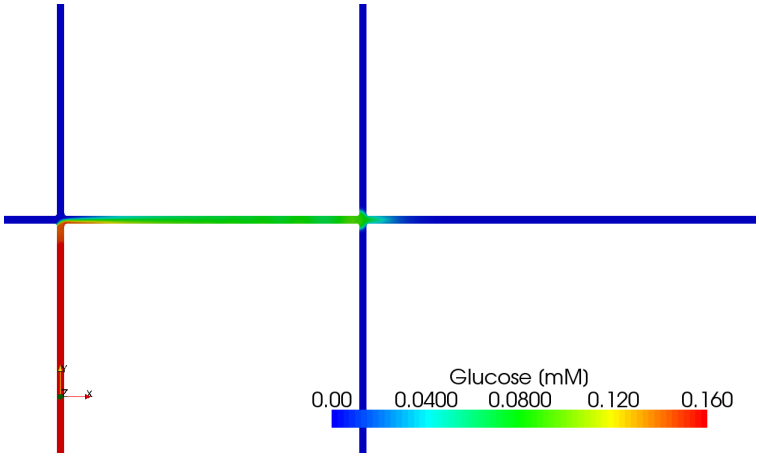

(b) Substrate at 2 seconds.

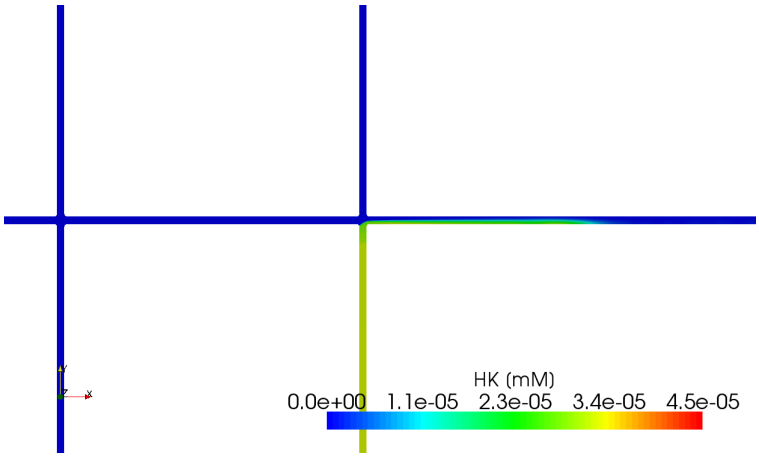

(c) Enzyme at 4 seconds.

Figure 5.34: Concentration profiles after injection process.

the profile reported by Atalay et al. (2009).

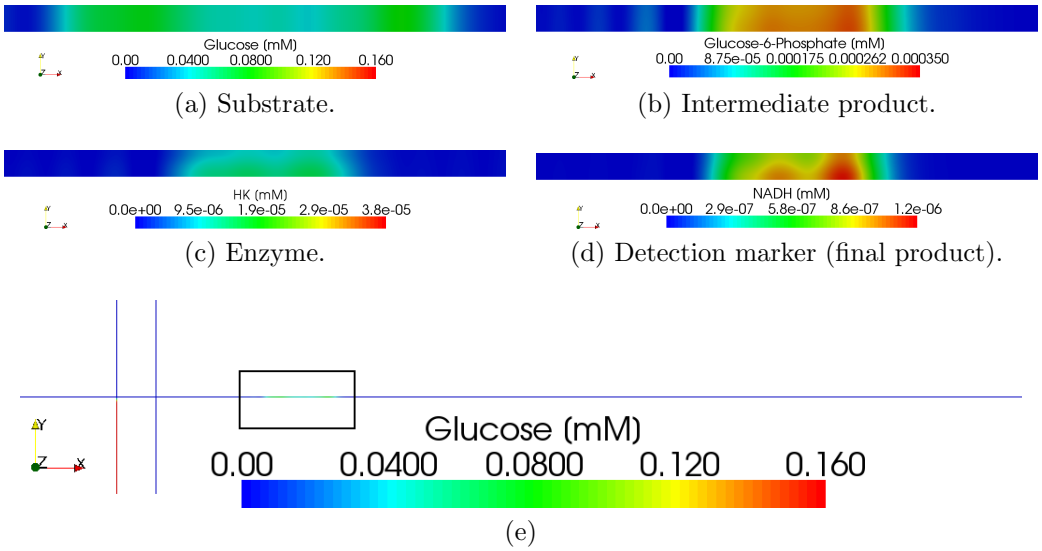

(a) Substrate. (b) Intermediate product. (c) Enzyme. (d) Detection marker (final product). (e)

Figure 5.35: Concentration for different components at $t = 10$ seconds.

5.3 Numerical test: electroosmotic flow in nanochannels

This example explores the applicability of additive Schwarz methods to a model problem of interest in nanoscale fluid dynamics. The interest in solving this problem grounds on testing numerical performance of the method, enabling the measurement of computation times and parallel efficiency.

An aqueous electrolyte solution of a simple fully dissociated symmetrical salt flowing on a nanochannel driven by EOF is considered. The channel has an L-shaped geometry with an horizontal and vertical lengths of 3 μm and a cross-section of 0.4 μm × 1 μm. As the electric double layer thickness (estimated through the Debye length, Eq. 3.9) is around 0.1 μm, the slip velocity approximation (Eq. 3.13) cannot model correctly the flow field. Physicochemical properties for the electrolyte solution are listed in Table 5.14.

Applied electric potential was computed by solving Eq. 3.25 with Dirichlet boundary conditions of 0.5 V at the inlet and 0 V at the outlet, and homoge-

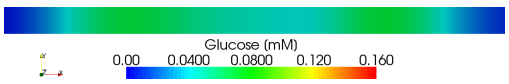

(a) Substrate.

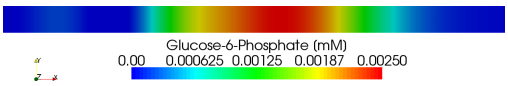

(b) Intermediate product.

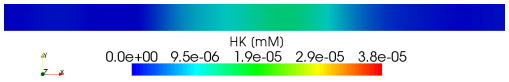

(c) Enzyme.

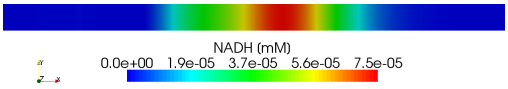

(d) Detection marker (final product).

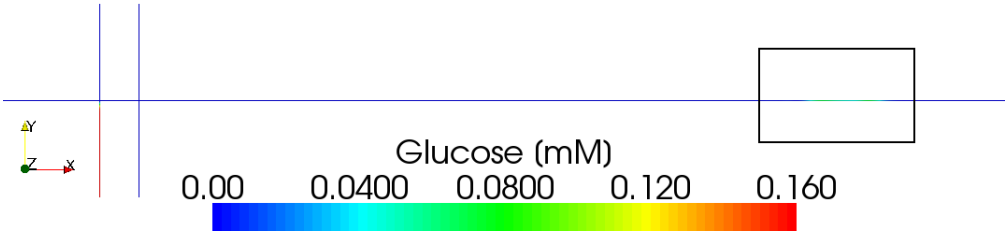

(e)

Figure 5.36: Concentration for different components at $t = 35$ seconds.

Property/Constant	Symbol	Value	Unit
density	ρ	1000	kg/m^3
dynamic viscosity	μ	10^{-3}	kg/m s
ionic valence	z	1	–
electrokinetic potential	ζ	$-4 \cdot 10^{-2}$	V
temperature	T	300	K
gas constant	R	8.31	J/mol K
Faraday constant	F	96485	C/mol
permittivity	ϵ	$80 \times 8.85 \cdot 10^{-12}$	F/m

Table 5.14: Physicochemical properties for the electrolyte solution used in the example 5.3.

neous Neumann boundary conditions at the channel walls. EDL electric potential was computed by solving the Eq. 3.7 with Dirichlet boundary conditions of 20 mV (the electrokinetic potential) at the channel walls and homogeneous Neumann boundary conditions at the channel inlet and outlet. The solution for this potential is shown in figure 5.37b. Electric potentials calculated were added-up in order to determine a total potential. Isolines of the total potential are shown in figure 5.37c.

Finally, Navier-Stokes equations were solved by entering the electrical forces as shown in equation 3.19. No-slip velocity boundary conditions are imposed at channel walls, and homogeneous Dirichlet boundary conditions are employed for pressure at the inlet and outlet. The computed velocity magnitude is shown in figure 5.37d. The L-shaped channel domain was discretized with a tetrahedral mesh with 569791 nodes, 3483613 elements and 20025163 degrees of freedom.

5.3.1 Test results

Although the problem at hand is essentially linear, it was solved as a full nonlinear one employing two iteration of a standard Newton method. In all the cases, the final (outer, nonlinear) residual norm was reduced by a factor of around 10^{-6}.

The linear systems at each nonlinear step were solved with GMRES(300) (i.e. GMRES restarted at 300 iterations) by defining a fixed relative tolerance of 10^{-4} for the reduction of the initial (inner, linear) residual norm.

The additive Schwarz method (ASM) was employed as a left-preconditioner within GMRES iterations. Being the global linear systems of saddle-point nature, they are ill-conditioned. Incomplete factorizations methods cannot be practically employed for the local problems, as this leads to GMRES stagnation (as is frequently experienced when using commercial software). Thus, the local problems were solved by employing full direct methods and aggressive subdomain sub-partitioning at each processor. The sub-partitioning was performed on the adjacency graph obtained from the local, *diagonal* part of the global sparse matrix with the help of METIS (Karypis and Kumar, 1998)

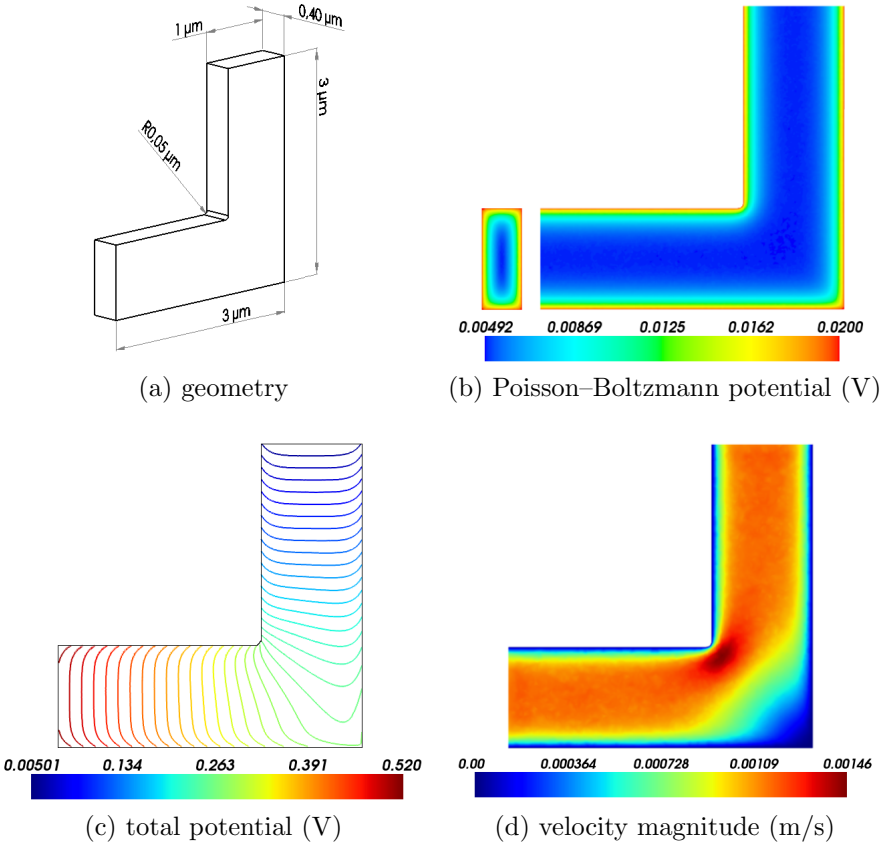

(a) geometry (b) Poisson–Boltzmann potential (V)

(c) total potential (V) (d) velocity magnitude (m/s)

Figure 5.37: Model Problem for ASM.

library.

In all test cases, wall-clock time measurements do not account for the time required for evaluating and assembling residual vectors and Jacobian matrices, but only for the time spent in solving the linear systems. Parallel efficiency was computed by taking as reference the timings of the runs performed on the smaller number of processes, i.e. $E_p = (P_{\min} T_{P_{\min}})/(pT_p)$, where $p = \{P_{\min}, \ldots, P_{\max}\}$ is the set of number of processes employed and T_p is the wall-clock time measurement with p processes.

The problem at hand was solved on 15, 20, 25, 35 and 45 processors. Figures 5.38 shows wall-clock time measurements and parallel efficiency for the additive Schwarz preconditioner with overlap zero. The optimal subdomain size seems to be around 1500 unknowns. Clearly, as the number of processors

increase beyond some limit, the required wall-clock time for obtaining the solution does not decrease but stagnates.

Wall-clock time includes the time for calculation, communication and synchronization processes. When the number of processors increases, calculation time decreases, nevertheless, communication time remains constant and the synchronization time even could increase. This situation, generally explains the stagnation on wall-clock time when the number of processors increases above a certain number. This number is related to the requirements of calculations and communications of each particular problem (Culler et al., 1999).

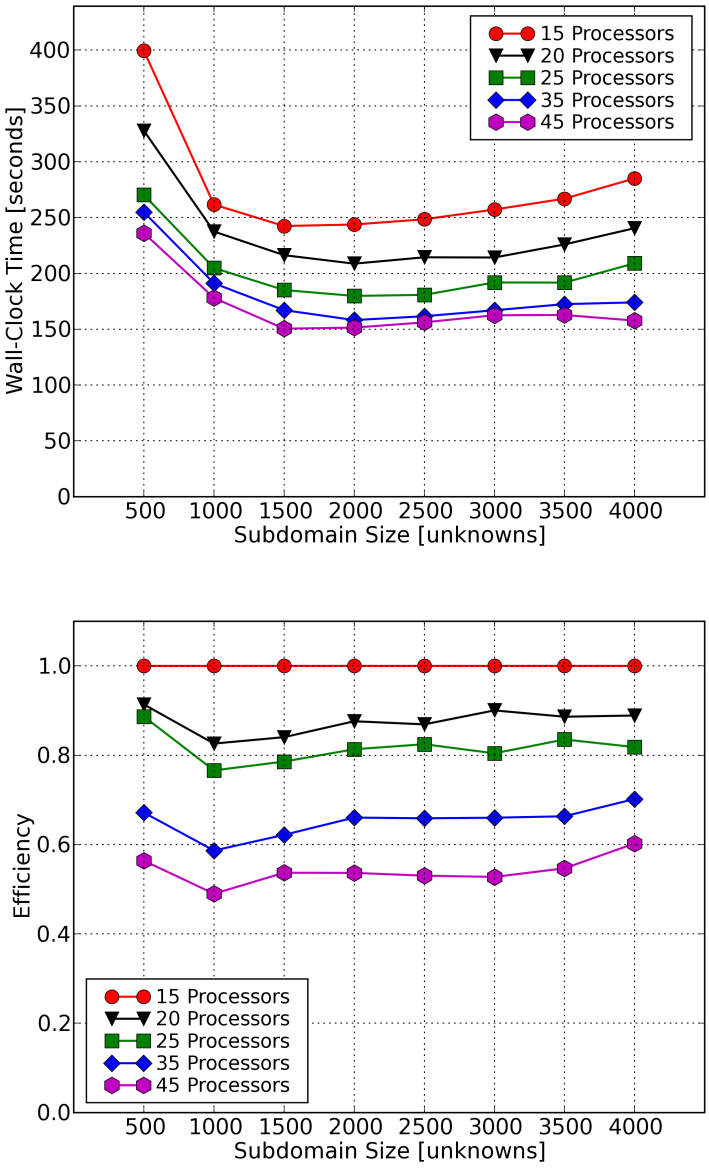

Figure 5.38: Additive Schwarz preconditioning performance.

Chapter 6

Conclusions

6.1 Summary and contributions of the work

Although LOC have been present since last twenty years, computer simulation of analytical techniques in microfabricated devices are more recent. It is clear that numerical models of electrophoretic separations, presented in section 2.1, played a fundamental role in the development and improvement of a wide variety of analytical techniques performed in classical bench-top capillary electrophoresis devices. Similarly, it is expected that computer simulations can contribute to a more successful development of LOC. The main contribution of this thesis is the successful development of a complete set of computational tools aimed to collaborate with design and prototyping processes of LOC.

Throughout this thesis all these contributions were presented and discussed. In chapters 1 and 2 historical facts related to LOC, such as manufacturing, applications, and how numerical simulations have contributed to their development were reviewed.

In chapters 3 and 4, the mathematical and numerical modelling of the phenomena involved in electrophoretic separations carried out in LOC were presented. These phenomena include electric, flow, and concentration fields and a wide variety of reaction kinetics. Discussion of these models and their implementation involves a significant amount of knowledge and expertise about theory and experiments in LOC. FEM results a very suitable tool for simulation

of entire LOC, showing clear advantages over commercial FVM programs (Li, 2004).

Finally, chapter 5 summarize numerical simulations for different analytical processes in LOC. This chapter provides both, validation of the techniques developed, and illustration about the capabilities of such techniques. These capabilities were shown by simulating LOC that are currently in use by the scientific community. The simulations included CZE, ITP, IEF, FFIEF, 2DE, immunoassay and enzymatic based assays. It was demonstrated that capabilities of the method are not only related with the HPC resources employed, that enables to solve large scale problems, but also with the generalized modelling, which allows to deal with a wide range of applications.

Main original contributions of this thesis are related to the modelling and the simulation. In what follows, these contributions are described.

6.1.1 Comprehensive modelling

In this thesis, phenomena involved in analytical processes in LOC were modelled. This modelling includes:

- the Poisson equation an its most used approximations to model the electric field at different length scales, from the EDL to the global applied electric potentials. This modelling includes a novel treatment for the high electric field gradients with no global approximations.

- A complete modelling of the fluid mechanics through the Navier - Stokes equations involving gravitational and electrical body force terms.

- A generalized mass transport equation including general migrative, advective, diffusive and reactive terms.

- An analytical equation to determine the electrokinetic potential of channel walls due to the variations of pH and ionic strength of the electrolyte solution.

- A flexible treatment for different reaction kinetics, including protolysis, acid base reactions, Micaelis - Menten kinetics, and enzymatic reactions for multiple substrates and products.

These characteristic shows that the original integration of these modelling stages performed during this thesis is comprehensive enough to understand and simulate a wide variety of analytical techniques and several particular experimental setups performed in LOC. As was shown in chapter 5, several different techniques were modelled successfully, demonstrating the comprehensiveness of the model, but there are many other analytical applications that can be implemented by using it, such as FFE, MBE and affinity CE, among others.

6.1.2 Simulation of LOC with HPC techniques

The result of the modelling process is a complete set of partial differential equations that models different processes in LOC. When combining these models with HPC techniques, a high performance simulation tool for general electrophoretic processes in LOC is obtained. These HPC techniques involves:

- Generalized algebraic tensor libraries.
- Advanced parallel data managing.
- Advanced domain decomposition techniques for preconditioning.
- High performance, iterative KSP solvers for linear systems.
- Adaptive mesh refinement.
- Parallel data visualization for large domains and high number of degrees of freedom.

The integration between the comprehensive modelling and these techniques, enables to perform a wide variety of complete LOC simulations overcoming the common difficulties encountered such as, the high aspect ratio in lengths involved, the huge number of degrees of freedom, and the coupling between the several physicochemical fields implicated. At present, computational

tools involving all these HPC techniques aimed to LOC simulations has not been reported. When using this combination, different original achievements were made, for example:

- simulations of entire LOC including the reservoirs.
- Two dimensional adaptive mesh refinement for ITP and two dimensional electrophoretic simulations.
- Two dimensional electrophoretic simulations involving continuous operation.

Additionally it is expected that the tool developed can serve to perform many others original simulations of electrophoretic separations in LOC, based on the generality of the model and the computational performance of the simulations.

6.2 Future work

The simulation tools developed, in conjunction with the knowledge and expertise acquired during their implementation, represents a motivating foundation to expand the modelling and simulation to other LOC applications. Nowadays, LOC are migrating into a new stage: after dominating genomic field, and currently developing proteomic applications, next step is cellomic. In this sense, future work will be oriented to the modelling and simulation of manipulation of macromolecules, microorganisms, organelles and cells in LOC.

Moreover, it is required to include new methods for handling, separation and analysis of macromolecules and cells, as dielectrophoresis, acustophoresis, magnetophoresis and others new techniques that are currently being developed by the scientific community.

6.3 Publications

During the work on this thesis the following articles have been published or are going to be published in the following referred journals,

- **Pablo A. Kler, Ezequiel J. López, Lisandro D. Dalcín , Fabio A. Guarnieri and Mario A. Storti**. High performance simulations of electrokinetic flow and transport in microfluidic chips. *Computer Methods in Applied Mechanics and Engineering*, **198(30-32)**:2360 - 2367, 2009.

- **Pablo A. Kler, Claudio L.A. Berli and Fabio A. Guarnieri**. Modelling and high performance simulation of electrophoretic techniques in microfluidic chips. *Microfluidics and Nanofluidics*, **10(1)**:187 - 198, 2010.

- **Lisandro D. Dalcín, Rodrigo R. Paz, Pablo A. Kler and Alejandro Cosimo**. Parallel distributed computing using Python. *Advances in Water Research*, In revision.

Also a work was presented at the 14th International Conference on Miniaturized Systems for Chemistry and Life Sciences, **MicroTas 2010**

- **Pablo A. Kler, Claudio L.A. Berli and Fabio A. Guarnieri**. Numerical prototyping of microfluidic chips for multidimensional electrophoretic separations. *Proceedings of 14th International Conference on Miniaturized Systems for Chemistry and Life Sciences*, 1061 - 1063, 2010.

Additionally, several articles have been submitted and presented in national conferences at Argentina in different topics related with this thesis.

Bibliography

Alauzet, F., Frey, P., George, P., Mohammadi, B.: 3-D transient fixed point mesh adaptation for time-dependent problems: Applications to CFD simulations. Journal of Computational Physics **222**, 592–623 (2007) 101

Amestoy, P.R., Duff, I.S., L'Excellent, J.Y., Koster, J.: A fully asynchronous multifrontal solver using distributed dynamic scheduling. SIAM J. Matrix Anal. A. **23**(1), 15–41 (2001) 73

Anderson, J., Chiu, D., Jackman, R., Cherniavskaya, O., McDonald, J., Wu, H., Whitesides, S., Whitesides, G.: Fabrication of topologically complex three-dimensional microfluidic systems in PDMS by rapid prototyping. Anal. Chem. **72**(14), 3158–3164 (2000) 8

Arnaud, I., Josserand, J., Rossier, J., Girault, H.: Finite element simulation of off-gel buffering. Electrophoresis **23**, 3253–3261 (2002) 36, 55, 56

Atalay, Y., Verboven, P., Vermeir, S., Vergauwe, N., Nicolaï, B., Lammertyn, J.: Modeling and optimization of a multi-enzyme electrokinetically driven multiplexed microchip for simultaneous detection of sugars. Microfluid. Nanofluid. **7**(3), 393–406 (2009) 37, 59, 119, 121, 122, 125

Balay, S., Buschelman, K., Eijkhout, V., Gropp, W.D., Kaushik, D., Knepley, M.G., McInnes, L.C., Smith, B.F., Zhang, H.: PETSc users manual. Tech. Rep. ANL-95/11 - Revision 3.1, Argonne National Laboratory (2010a) 71

Balay, S., Buschelman, K., Gropp, W.D., Kaushik, D., Knepley, M.G., McInnes, L.C., Smith, B.F., Zhang, H.: PETSc Web page (2010b). `http://www.mcs.anl.gov/petsc` 71

Balay, S., Gropp, W.D., McInnes, L.C., Smith, B.F.: Efficient management of parallelism in object oriented numerical software libraries. In: Arge, E., Bruaset, A.M., Langtangen, H.P. (eds.) Modern Software Tools in Scientific Computing, pp. 163–202. Birkhäuser Press (1997) 72

Barbier, V., Tatoulian, M., Li, H., Arefi-Khonsari, F., Ajdari, A., Tabeling, P.: Stable modification of PDMS surface properties by plasma polymerization: Application to the formation of double emulsions in microfluidic systems. Langmuir **22**(12), 5230–5232 (2006) 10

Baroud, C., Okkels, F., Menetrier, L., Tabeling, P.: Reaction-diffusion dynamics: Confrontation between theory and experiment in a microfluidic reactor. Phys. Rev. E **67**(6), 60,104 (2003) 36

Barz, D., Ehrhard, P.: Fully-coupled model for electrokinetic flow and transport in microchannels. PAMM **5**(1), 535–536 (2007) 95

Barz, D.P.: Comprehensive model of electrokinetic flow and migration in microchannels with conductivity gradients. Microfluid. Nanofluid. **7**(2), 249 –265 (2009) 38, 52

Bean, K.: Anisotropic etching of silicon. IEEE T. Electron Dev. **25**(10), 1185–1193 (2005) 6

Becker, H., Gärtner, C.: Polymer microfabrication methods for microfluidic analytical applications. Electrophoresis **21**(1), 12–26 (2000) 7

Becker, H., Locascio, L.: Polymer microfluidic devices. Talanta **56**(2), 267–287 (2002) 7

Bercovici, M., Lele, S.K., Santiago, J.G.: Open source simulation tool for electrophoretic stacking, focusing, and separation. J. Chromatogr. A **1216**, 1008 – 1018 (2009) 27, 28, 100, 102

Berli, C.L.A.: Equivalent circuit modeling of electrokinetically driven analytical microsystems. Microfluid. Nanofluid. **4**(5), 391 – 399 (2008) 31, 49, 52

Berli, C.L.A., Piaggio, M., Deiber, J.: Modeling the zeta potential of silica capillaries in relation to the background electrolyte composition. Electrophoresis **24**, 1587–1595 (2003) 54, 55, 89

Berzins, M., Speares, W.: A 3D Unstructured Mesh Adaption Algorithm for Time Dependent Shock Dominated Problems. Int. Journal for Num. Methods in Fluids **25**, 81–104 (1997) 101

Bharadwaj, R., Santiago, J., Mohammadi, B.: Design and optimization of on-chip capillary electrophoresis. Electrophoresis **23**(16), 2729–2744 (2002) 33

Bianchi, F., Ferrigno, R., Girault, H.: Finite element simulation of an electroosmotic-driven flow division at a T-junction of microscale dimensions. Anal. Chem. **72**(9), 1987–1993 (2000) 33, 35

Bier, M., Palusinski, O., Mosher, R., Saville, D.: Electrophoresis: mathematical modeling and computer simulation. Science **219**(4590), 1281 (1983) 27

Brunet, E., Adjari, A.: Generalized Onsager relations for electrokinetic effects in anisotropic and heterogeneous geometries. Phys. Rev. E **69**(1), 016,306 (2004) 52

Cai, X.C., Keyes, D.E.: Nonlinearly preconditioned inexact newton algorithms. SIAM J. Sci. Comput. **24**(1), 183–200 (2002) 57

Chatterjee, A.: Generalized numerical formulations for multi-physics microfluidics-type applications. J. Micromech. Microeng. **13**, 758–767 (2003) 38, 57, 86, 87

Chau, M., Spiteri, P., Guivarich, R., Boisson, H.: Parallel asynchronous iterations for the solution of a 3d continuous flow electrophoresis problem. Comput. Fluid. **37**(9), 1126–1137 (2008) 38

Chen, C., Cho, C.: Electrokinetically driven flow mixing utilizing chaotic electric fields. Microfluid. Nanofluid. **5**(6), 785–793 (2008) 34

Chen, L., Prest, J., Fielden, P., Goddard, N., Manz, A., Day, P.: Miniaturised isotachophoresis analysis. Lab Chip **6**(4), 474–487 (2006) 19

Chiem, N., Harrison, D.: Microchip systems for immunoassay: an integrated immunoreactor with electrophoretic separation for serum theophylline determination. Clin. Chem. **44**(3), 591 (1998) 23

Craven, T.J., Rees, J.M., Zimmerman, W.B.: On slip velocity boundary conditions for electroosmotic flow near sharp corners. Phys. Fluids **20**(4), 043,603 (2008) 34, 50, 52

Cui, H., Dutta, P., Ivory, C.: Isotachophoresis of proteins in a networked microfluidic chip: Experiment and 2-D simulation. Electrophoresis **28**(7), 1138–1145 (2007) 19, 38

Culbertson, C., Jacobson, S., Ramsey, J.: Dispersion sources for compact geometries on microchips. Anal. Chem. **70**(18), 3781–3789 (1998) 33

Culler, D., Singh, J., Gupta, A.: Parallel computer architecture: a hardware/software approach. Morgan Kaufmann Pub (1999) 129

Dalcín, L.: PETSc for Python (2005-2010). `http://petsc4py.googlecode.com/` 71, 73

Dalcín, L., Paz, R., Storti, M., D'Elia, J.: MPI for Python: Performance improvements and MPI-2 extensions. J. Parallel Distr. Com. **68**(5), 655–662 (2008) 71, 74

Dalcín, L.L.: Techiniques for high-performance distributed computing in computational fluid mechanics. Ph.D. thesis, Facultad de Ingeniería - Universidad Nacional del Litoral (2008) 71, 73

Debusschere, B., Najm, H., Matta, A., Knio, O., Ghanem, R., Le Maître, O.: Protein labeling reactions in electrochemical microchannel flow: numerical simulation and uncertainty propagation. Phys. Fluids **15**, 2238 (2003) 36

Donea, J., Huerta, A.: Finite Element Methods for Flow Probelms. Wiley Online Library (2003) 63, 68, 101

Dose, E., Guiochon, G.: High-resolution modeling of capillary zone electrophoresis and isotachophoresis. Anal. Chem. **63**(11), 1063–1072 (1991) 27

Duffy, D., McDonald, J., Schueller, O., Whitesides, G.: Rapid prototyping of microfluidic systems in poly (dimethylsiloxane). Anal. Chem. **70**(23), 4974–4984 (1998) 2, 8, 10

Dunker, A., Rueckert, R.: Observations on molecular weight determinations on polyacrilamide gel. J Biol. Chem. **244**(18), 5074 – 5080 (1969) 119

Effenhauser, C., Bruin, G., Paulus, A., Ehrat, M.: Integrated capillary electrophoresis on flexible silicone microdevices: analysis of DNA restriction fragments and detection of single DNA molecules on microchips. Anal. Chem. **69**(17), 3451–3457 (1997) 8

Efimenko, K., Wallace, W., Genzer, J.: Surface modification of Sylgard-184 poly (dimethyl siloxane) networks by ultraviolet and ultraviolet/ozone treatment. J. Colloid Interf. Sci. **254**(2), 306–315 (2002) 8

Erickson, D.: Towards numerical prototyping of labs-on-chip: modeling for integrated microfluidic devices. Microfluid. Nanofluid. **1**(4), 301–318 (2005) 30, 95

Erickson, D., Li, D.: Influence of surface heterogeneity on electrokinetically driven microfluidic mixing. Langmuir **18**(5), 1883–1892 (2002) 34, 36

Erickson, D., Li, D.: Integrated microfluidic devices. Anal. Chim. Acta **507**(1), 11–26 (2004) 17, 31

Erickson, D., Li, D., Krull, U.: Modeling of DNA hybridization kinetics for spatially resolved biochips. Anal. Biochem. **317**(2), 186–200 (2003) 37

Ermakov, S., Jacobson, S., Ramsey, J.: Computer simulations of electrokinetic transport in microfabricated channel structures. Anal. Chem. **70**(21), 4494–4504 (1998) 33

Ermakov, S., Jacobson, S., Ramsey, J.: Computer simulations of electrokinetic injection techniques in microfluidic devices. Anal. Chem. **72**(15), 3512–3517 (2000) 33

Falgout, R., Jones, J., Yang, U.: Numerical Solution of Partial Differential Equations on Parallel Computers, vol. 51, chap. The Design and Implementation of hypre, a Library of Parallel High Performance Preconditioners, pp. 267–294. Springer-Verlag (2006) 73, 97

Ford, S.: Fabricating Microfluidic Devices in Polymers for Bioanalytical Applications. Ph.D. thesis, Louisiana State University (2001) 9, 10

Gabriel, E., Fagg, G.E., Bosilca, G., Angskun, T., Dongarra, J.J., Squyres, J.M., Sahay, V., Kambadur, P., Barrett, B., Lumsdaine, A., Castain, R.H., Daniel, D.J., Graham, R.L., Woodall, T.S.: Open MPI: Goals, concept, and design of a next generation MPI implementation. In: Proceedings, 11th European PVM/MPI Users' Group Meeting, pp. 97–104. Budapest, Hungary (2004) 74

Glasgow, I., Batton, J., Aubry, N.: Electroosmotic mixing in microchannels. Lab Chip **4**(6), 558–562 (2004) 34

Graß, B., Hergenröder, R., Neyer, A., Siepe, D.: Determination of selenoamino acids by coupling of isotachophoresis/capillary zone electrophoresis on a PMMA microchip. J. Sep. Sci. **25**(3), 135–140 (2002) 19

Griffiths, S., Nilson, R.: Band spreading in two-dimensional microchannel turns for electrokinetic species transport. Anal. Chem. **72**(21), 5473–5482 (2000) 33

Gropp, W., Huss-Lederman, S., Lumsdaine, A., Lusk, E., Nitzberg, B., Saphir, W., Snir, M.: MPI - The Complete Reference: Volume 2, The MPI-2 Extensions, *Scientific and engineering computation*, vol. 2, The MPI-2 Extensions. 2nd. edn. MIT Press, Cambridge, MA, USA (1998) 73

Gropp, W., Lusk, E., Doss, N., Skjellum, A.: A high-performance, portable implementation of the MPI message passing interface standard. Parallel Computing **22**(6), 789–828 (1996) 74

Găs, B.: Master's thesis, Charles University of Prague (1975) 27

Găs, B., Coufal, P., Jaroš, M., Muzikáš, J., Jelínek, I.: Optimization of background electrolytes for capillary electrophoresis: I. Mathematical and computational model. J. Chromatogr. A **905**(1-2), 269–279 (2001) 26

Gad el Hak, M.: The MEMS handbook. CRC (2006) 4

Hatch, A., Kamholz, A., Hawkins, K., Munson, M., Schilling, E., Weigl, B., Yager, P.: A rapid diffusion immunoassay in a T-sensor. Nature Biotechnology **19**(5), 461–465 (2001) 37, 59

Heckele, M., Schomburg, W.: Review on micro molding of thermoplastic polymers. J. Micromec. Microeng. **14**, R1 (2004) 7

Helmholtz, H.: Studien über electrische Grenzschichten. Annalen der Physik **243**(7), 337–382 (1879) 14, 40

Heroux, M., Bartlett, R., Hoekstra, V.H.R., Hu, J., Kolda, T., Lehoucq, R., Long, K., Pawlowski, R., Phipps, E., Salinger, A., Thornquist, H., Tuminaro, R., Willenbring, J., Williams, A.: An Overview of Trilinos. Tech. Rep. SAND2003-2927, Sandia National Laboratories (2003) 73

Herr, A., Molho, J., Drouvalakis, K., Mikkelsen, J., Utz, P., Santiago, J., Kenny, T.: On-chip coupling of isoelectric focusing and free solution electrophoresis for multidimensional separarions. Anal. Chem **75**, 1180–1187 (2003) xxiv, 90, 104, 107, 108

Herr, A., Molho, J., Santiago, J., Mungal, M., Kenny, T., Garguilo, M.: Electroosmotic capillary flow with nonuniform zeta potential. Anal. Chem **72**, 1053–1057 (2000) 50, 89

Hillborg, H., Ankner, J., Gedde, U., Smith, G., Yasuda, H., Wikström, K.: Crosslinked polydimethylsiloxane exposed to oxygen plasma studied by neutron reflectometry and other surface specific techniques. Polymer **41**(18), 6851–6863 (2000) 8

Hruška, V., Jaros, M., Gaš, B.: Simul 5 - free dynamic simulator of electrophoresis. Electrophoresis **27**, 984–991 (2006) 27

Hu, G., Gao, Y., Li, D.: Modeling micropatterned antigen-antibody binding kinetics in a microfluidic chip. Biosensors and Bioelectronics **22**(7), 1403–1409 (2007) 37

Hunter, R.: Foundations of colloid science. Clarendon Press Oxford (1989) 29

Hunter, R.: Foundations of Colloid Science. second edn. Oxford University Press (2001) 40, 51, 54

Idelsohn, S., Oñate, E.: Finite volumes and finite elements: two good friends. Int. J. Numer. Meth. Eng. **37**(19), 3323–3341 (1994) 63

Jain, M., Nandakumar, K.: Novel index for micromixing characterization and comparative analysis. Biomicrofluidics **4**, 031,101 (2010) 34

Jen, C., Wu, C., Lin, Y., Wu, C.: Design and simulation of the micromixer with chaotic advection in twisted microchannels. Lab Chip **3**(2), 77–81 (2003) 34

Johnson, C.: Numerical solution of partial differential equations by the finite element method, vol. 32. Cambridge university press Cambridge (1987) 62

Jorgenson, J., Lukacs, K.: Zone electrophoresis in open-tubular glass capillaries. Anal. Chem. **53**(8), 1298–1302 (1981) 15

Karniadakis, G., Beşkök, A., Aluru, N.: Microflows and nanoflows: fundamentals and simulation. Springer Verlag (2005) 33

Karypis, G., Kumar, V.: Multilevel k-way partitioning scheme for irregular graphs. J. Parallel Distr. Com. **48**(1), 96–129 (1998) 127

Khurana, T.K., Santiago, J.G.: Preconcentration, separation, and indirect detection of nonfluorescent analytes using fluorescent mobility markers. Anal. Chem. **80**(1), 279–286 (2008) 99, 102

Kirby, B., Hasselbrink, E.: Zeta potential of microfluidic substrates: 1. theory, experimental techniques, and effects on separations. Electrophoresis **25**, 187–202 (2004) 54

Kirby, R., Karniadakis, G., Mikulchenko, O., Mayaram, K.: An integrated simulator for coupled domain problems in MEMS. J. Microelectromech. S. **10**(3), 379–391 (2002) 31

Kirby, R., Warburton, T., Sherwin, S., Beskok, A., Karniadakis, G.: N epsilon Kappa tau alpha r code: Dynamic simulations without remeshing. In: Proceedings of 2nd International Conference on Computational Technologies for Fluid/Thermal/Chemical Systems with Industrial Applications. **397**, 105–116 (1999) 31

Kler, P.: Diseño y fabricación de un sistema de uso en análisis clínicos. Master's thesis, Universidad Nacional de Entre Ríos (2006) 4

Koch, M., Evans, A., Brunnschweiler, A., Evans, A., Brunnschweiler, A.: Microfluidic technology and applications. Research Studies Press Baldock (2000) 3, 4, 12

Kohlheyer, D., Besselink, G.A.J., Schlautmann, S., Schasfoort, R.B.M.: Free-flow zone electrophoresis and isoelectric focusing using a microfabricated glass device with ion permeable membranes. Lab. Chip. **6**, 374 – 380 (2006) 107

Kohlheyer, D., Eijkel, J., Schlautmann, S., van den Berg, A., Schasfoort, R.: Microfluidic high-resolution free-flow isoelectric focusing. Anal. Chem. **79**(21), 8190–8198 (2007) 20, 21

Kohlheyer, D., Eijkel, J.C.T., van den Berg, A., Schasfoort, R.B.M.: Miniaturizing free-flow electrophoresis a critical review. Electrophoresis **29**(5), 977 – 993 (2008) 106

Korvink, J., Paul, O.: MEMS: a practical guide to design, analysis, and applications. Springer (2006) 5

Kovacs, G., Maluf, N., Petersen, K.: Bulk micromachining of silicon. Proceedings of the IEEE **86**(8), 1536–1551 (2002) 5

Landers, J.P.: Handbook of capillary and microchip electrophoresis and associated microtechniques. third edn. CRC Press (2007) 12

Lee, L., Berger, S., Pruitt, L., Liepmann, D.: Key elements of a transparent teflon® microfluidic system. In: Micro total analysis systems' 98: proceedings of the [Mu] TAS'98 Workshop, held in Banff, Canada, 13-16 October 1998, p. 245. Kluwer Academic Publishers (1998) 9

Li, D.: Electrokinetics in Microfluidics. Elsevier Academic Press (2004) 30, 33, 49, 132

Löhner, R., Baum, J.: Adaptive h-refinement on 3-D unstructured grids for transient problems. Int. Journal for Num. Methods in Fluids **14**, 1407–1419 (1992) 101

Lu, H., Gaudet, S., Schmidt, M., Jensen, K.: A microfabricated device for subcellular organelle sorting. Anal. Chem. **76**(19), 5705–5712 (2004) 18

Luo, X., Beskok, A., Karniadakis, G.: Modeling electrokinetic flows by the smoothed profile method. J. Computa. Phys. **229**(10), 3828–3847 (2010) 33

MacInnes, J., Du, X., Allen, R.: Prediction of electrokinetic and pressure flow in a microchannel T-junction. Phys. Fluids **15**(7), 1992–2005 (2003) 37, 49

MacInnes, J.M.: Computation of reacting electrokinetic flow in microchannel geometries. Chem. Eng. Sci. **57**(21), 4539 – 4558 (2002) 36, 52

Madou, M.: Fundamentals of microfabrication: the science of miniaturization. CRC (2002) 3, 4, 5, 11

Maluf, N., Williams, K.: Introduction to microelectromechanical systems engineering. Artech House Publishers (2004) 5

Manz, A., Graber, N., Widmer, H.: Miniaturized total chemical analysis systems: A novel concept for chemical sensing. Sensor. Actuat. B **1**, 244–248 (1990a) 2, 29

Manz, A., Miyahara, Y., Miura, J., Watanabe, Y., Miyagi, H., Sato, K.: Design of an open-tubular column liquid chromatograph using silicon chip technology. Sensors and Actuators B: Chemical **1**(1-6), 249 – 255 (1990b) 2

Marangoni, A.: Enzyme kinetics: a modern approach. John Wiley and Sons (2003) 58

Miranda, J., Oliveira, H., Teixeira, J., Vicente, A., Correia, J., Minas, G.: Numerical study of micromixing combining alternate flow and obstacles. International Communications in Heat and Mass Transfer **37**(6), 581–586 (2010) 34

Molho, J., Herr, A., Mosier, B., Santiago, J., Kenny, T., Brennen, R., Gordon, G., Mohammadi, B.: Optimization of turn geometries for microchip electrophoresis. Anal. Chem **73**(6), 1350–1360 (2001) 33

Moore, G.: Theory of isotachophoresis development of concentration boundaries. Journal of Chromatography A **106**(1), 1–16 (1975) 27

Mosher, R., Gebauer, P., Thormann, W.: Computer simulation and experimental validation of the electrophoretic behavior of proteins:: III. Use of titration data predicted by the protein's amino acid composition. Journal of Chromatography A **638**(2), 155–164 (1993) 27

Mosher, R., Saville, D., Thormann, W.: The dynamics of electrophoresis. VCH Weinheim (1992) 27

Mosher, R., Zhang, C., Caslavska, J., Thormann, W.: Dynamic simulator for capillary electrophoresis with in situ calculation of electroosmosis. J. Chromatogr. A **716**(1-2), 17–26 (1995) 28

MPICH2 Team: MPICH2: A portable implementation of MPI (2003-2010). `http://www-unix.mcs.anl.gov/mpi/mpich2/` 74

Newman, C., McGuffin, V.: Stochastic simulation of reactive separations in capillary electrophoresis. Electrophoresis **26**(3), 537–547 (2005) 27

Obermaier, C., Jankowski, V., Schmutzler, C., Bauer, J., Wildgruber, R., Infanger, M., Köhrle, J., Krause, E., Weber, G., Grimm, D.: Free-flow isoelectric focusing of proteins remaining in cell fragments following sonication of thyroid carcinoma cells. Electrophoresis **26**(11), 2109–2116 (2005) 20

Oddy, M., Santiago, J., Mikkelsen, J.: Electrokinetic instability micromixing. Anal. Chem. **73**(24), 5822–5832 (2001) 34

O'Farrell, P.H.: High resolution two-dimensional electrophoresis of proteins. J. Biol. Chem. **250**(10), 4007–4021 (1975) 21, 102

Oliphant, T.: NumPy: Numerical Python (2005–2010). `http://numpy.scipy.org/` 74

Oosterbroek, R., van den Berg, A.: Lab-on-a-Chip; Miniaturized Systems for (BIO) Chemical Analysis and Synthesis. Elsevier BV (2003) 3

Open MPI Team: Open MPI: Open source high performance computing (2004–2010). `http://www.open-mpi.org/` 74

Overbeek, J.: In: HR Kruyt, Editor, Colloid Science Vol. 1 (1952) 40

Palusinski, O., Allgyer, T., Mosher, R., Bier, D., et al.: Mathematical modeling and computer simulation of isoelectric focusing with electrochemically defined ampholytes. Biophysical Chemistry **13**(3), 193–202 (1981) 26

Palusinski, O., Graham, A., Mosher, R., Bier, M., Saville, D.: Theory of electrophoretic separations. part ii: Construction of a numerical scheme and its applications. AICHE J. **32**(2), 215–223 (1986) 86, 87, 88

Patankar, N., Hu, H.: Numerical simulation of electroosmotic flow. Anal. Chem. **70**(9), 1870–1881 (1998) 31

Paz, R., Storti, M., Castro, H., Dalcin, L.: Using hybrid parallel programming techniques for the computation, assembly and solution stages in finite element codes. Latin Am. Appl. Res. (2010). In press. 77

Peng, Y., Pallandre, A., Tran, N.T., Taverna, M.: Recent innovations in protein separation on microchips by electrophoretic methods. Electrophoresis **29**(1), 157–178 (2008) 15

Posner, J.D., Santiago, J.G.: Convective instability of electrokinetic flows in a cross-shaped microchannel. J. Fluid Mech. **555**(-1), 1–42 (2006) 34, 50, 107

Prest, J., Baldock, S., Fielden, P., Goddard, N., Brown, B.: Analysis of chloride, bromide and iodide using miniaturised isotachophoresis on a planar polymer chip. The Analyst **130**(10), 1375–1382 (2005) 19

Probstein, R.: Physicochemical hydrodynamics: an introduction. Butterworths (1989) 29

Probstein, R.: Physicochemical Hydrodynamics. An Introduction. second edn. Wiley-Interscience (2003) 13, 42, 43, 45, 48, 49, 53, 54

Pumera, M.: Microchip-based electrochromatography: designs and applications. Talanta **66**(4), 1048–1062 (2005) 22

Qiao, R., Aluru, N.: A compact model for electroosmotic flows in microfluidic devices. J. Micromech. Microeng. **12**, 625 (2002) 31, 32

Radi, P., Schumacher, E.: Numerical simulation of electrophoresis: The complete solution for three isotachophoretic systems. Electrophoresis **6**(5), 195–200 (1985) 27

Ramachandran, P.: Mayavi data visualizer (2001-2010). `http://www.mayavi.sourceforge.net/` 82

Reijenga, J., Martens, J., Everaerts, F.: Training software for electrophoresis. Electrophoresis **16**(1), 2008–2015 (1995) 26

Ren, C., Li, D.: Effects of spatial gradients of electrical conductivity on chip-based sample injection processes. Anal. Chim. Acta **518**(1-2), 59–68 (2004) 34

Renaud, P., Van Lintel, H., Heuschkel, M., Guérin, L., Harrison, D.: Photopolymer microchannel technologies and applications. In: Micro total analysis systems' 98: proceedings of the [Mu] TAS'98 Workshop, held in Banff, Canada, 13-16 October 1998, p. 17. Kluwer Academic Publishers (1998) 8

Reuss, F.: Mem. Soc. Imperiale Naturalistes de Moscow **2**, 327 (1809) 13, 46

Reyes, D., Iossifidis, D., Auroux, P., Manz, A.: Micro total analysis systems. 1. Introduction, theory, and technology. Anal. Chem. **74**(12), 2623–2636 (2002) 3, 46

Ríos Rodriguez, G., Storti, M., Nigro, N.: An h-adaptive unstructured mesh refinement strategy for unsteady problems. Latin American Applied Research **39**, 137–143 (2009) 101

Roberts, G., Rhodes, P., Snyder, R.: Dispersion effects in capillary zone electrophoresis. J. Chromatogr. A **480**, 35–67 (1989) 27

Roberts, M., Rossier, J., Bercier, P., Girault, H.: UV laser machined polymer substrates for the development of microdiagnostic systems. Anal. Chem. **69**(11), 2035–2042 (1997) 10

Rossier, J., Gokulrangan, G., Girault, H., Svojanovsky, S., Wilson, G.: Characterization of protein adsorption and immunosorption kinetics in photoablated polymer microchannels. Langmuir **16**(22), 8489–8494 (2000) 9

van Rossum, G.: Python programming language (1990–2010a). `http://www.python.org/` 74, 82

van Rossum, G.: Python reference manual (2010b). `http://docs.python.org/ref/ref.html` 74

Sandia, N.L., CSimSoft: Paraview: Large data visualiztion (2000-2010). `http://www.paraview.org/` 82

Santiago, J.: Electroosmotic flows in microchannels with finite inertial and pressure forces. Analytical Chemistry **73**(10), 2353–2365 (2001) 50

Saville, D., Palusinski, O.: Theory of electrophoretic separations. part i: Formulation of a mathematical model. AICHE J. **32**(2), 207–214 (1986) 28

Schoch, R., Han, J., Renaud, P.: Transport phenomena in nanofluidics. Reviews of Modern Physics **80**(3), 839–883 (2008) 40, 64

Shaw, D., Williams, R.: Introduction to Colloid and Surface Chemistry. Butterworths (1968) 13, 45

Shim, J., Dutta, P., Ivory, C.: Modeling and simulation of IEF in 2-D microgeometries. Electrophoresis **28**, 572–586 (2007) 29, 57, 86, 91, 93

Shimao, K.: Mathematical approach to zone boundary of isotachophoresis system. Electrophoresis **7**(3), 121–128 (1986) 26

Skurtys, O., Aguilera, J.: Applications of microfluidic devices in food engineering. Food Biophysics **3**(1), 1–15 (2008) 24

Smoluchowski, M.: Handbuch der Elektrizität und des Magnetismus: in fünf Bänden (1918) 46

Smoluchowsky, M.: Bull. Int. Acad. Sci. Cracovie **2**, 184 (1903). Page 14

Snir, M., Otto, S., Huss-Lederman, S., Walker, D., Dongarra, J.: MPI - The Complete Reference: Volume 1, The MPI Core, *Scientific and engineering computation*, vol. 1, The MPI Core. 2nd. edn. MIT Press, Cambridge, MA, USA (1998) 73

Sonzogni, V.E., Yommi, A.M., Nigro, N.M., Storti, M.A.: A parallel finite element program on a Beowulf cluster. Adv. Eng. Softw. **33**(7–10), 427–443 (2002) 71

Sounart, T., Baygents, J.: Electrically-driven fluid motion in channels with streamwise gradients of the electrical conductivity. Colloid. Surface. A **195**(1-3), 59–75 (2001) 34

Sounart, T.L., Baygents, J.C.: Lubrication theory for electro-osmotic flow in a non-uniform electrolyte. J. Fluid. Mech. **576**(-1), 139–172 (2007) 29, 34, 52

Stern, O.: The theory of the electric double layer. Z. Electrochem. **30**, 508 (1924) 40

Storti, M.A.: Aquiles cluster at CIMEC (2005-2010). `http://www.cimec.org.ar/aquiles` 85

Storti, M.A., Nigro, N., Paz, R.: PETSc-FEM: A general purpose, parallel, multi-physics FEM program (1999-2010). `http://www.cimec.org.ar/petscfem` 68, 71

Storti, M.A., Nigro, N.M., Paz, R.R., Dalcín, L.D.: Strong coupling strategy for fluid-structure interaction problems in supersonic regime via fixed point iteration. J. Sound Vib. **320**(4-5), 859 – 877 (2009) 57

Strickler, A., Kaplan, A., Vigh, E.: Continuous microfractionation of particle mixtures by electrophoresis. Microchem. J. **10**(1-4), 529–544 (1966) 20

Svensson, H.: Isoelectric fractionation, analysis, and characterization of ampholytes in natural pH gradients. I. The differential equation of solute concentrations at steady state and its solution for simple cases. Acta Chem. Scand. **15**, 325 – 341 (1961) 93

Tabeling, P.: Introduction to Microfluidics. Oxford University Press, USA (2005) 33

Terry, S.C., Jerman, J.H., Angell, J.B.: A gas chromatographic air analyzer fabricated on a silicon wafer. IEEE Tran. Electron Devices **26**, 1880 (1979) 1, 2, 3

Tezduyar, T., Mittal, S., Ray, S., Shih, R.: Incompressible flow computations with stabilized bilinear and linear equal order interpolation velocity pressure elements. Comput. Method. Appl. M. **95**, 221–242 (1992) 68

Tezduyar, T., Osawa, Y.: Finite element stabilization parameters computed from element matrices and vectors. Comput. Method. Appl. M. **190**(3-4), 411–430 (2000) 68, 69

Tezduyar, T., Senga, M.: Determination of the shock-capturing parameters in supg formulation of compressible flows. Computational Mechanics WCCM IV, Beijing, China **2004** (2004) 69

Thormann, W., Caslavska, J., Breadmore, M., Mosher, R.: Dynamic computer simulations of electrophoresis: Three decades of active research. Electrophoresis **30**(S1), S16–S26 (2009) 26

Thormann, W., Caslavska, J., Mosher, R.: Modeling of electroosmotic and electrophoretic mobilization in capillary and microchip isoelectric focusing. J. Chromatogr. A **1155**(2), 154 – 163 (2007) 89, 90

Thormann, W., Huang, T., Pawliszyn, J., Mosher, R.: High-resolution computer simulation of the dynamics of isoelectric focusing of proteins. Electrophoresis **25**(2), 324–337 (2004) 28, 29

Tia, S., He, M., Kim, D., Herr, A.: On-chip multi-analyte native western blotting in two minutes. In Proceedings of 14th International Conference on Miniaturized Systems for Chemistry and Life Sciences pp. 731–733 (2010) xxv, 116, 120

Tia, S., Herr, A.: On-chip technologies for multidimensional separations. Lab Chip **9**, 2524–2536 (2009) 22, 106, 107, 109

Tian, W.C., Finehout, E.: Microfluidics for Biological Applications. first edn. Springer (2008) 15

Tian, W.C., Finehout, E.: Materials and microfabrication processes for microfluidic devices. In: Microfluidics for Biological Applications, pp. 35–92. Springer US (2009) 4

Tsai, C., Chen, H., Wang, Y., Lin, C., Fu, L.: Capabilities and limitations of 2-dimensional and 3-dimensional numerical methods in modeling the fluid flow in sudden expansion microchannels. Microfluidics and Nanofluidics **3**(1), 13–18 (2007) 50

Tsai, W.B., Hsieh, C.J., Chieng, C.C.: Parallel computation of electroosmotic flow in L-shaped microchannels. 6th World Congress of Structural and Multiisciplinary Optimization pp. 4971–4980 (2005) 38

Turgeon, R.T., Bowser, M.T.: Micro free-flow electrophoresis: theory and applications. Anal. Bioanal. Chem. **394**(1), 187 – 198 (2009) 20, 106

Vermeir, S., Nicola
"ı, B., Jans, K., Maes, G., Lammertyn, J.: High-throughput microplate enzymatic assays for fast sugar and acid quantification in apple and tomato. J. Agric. Food Chem **55**(9), 3240–3248 (2007) 122

Vilkner, T., Janasek, D., Manz, A.: Micro total analysis systems. Recent developments. Anal. Chem. **76**(12), 3373–3386 (2004) 23

Waltz, J.: Parallel Adaptive Refinement for Unsteady Flow Calculations on 3-D Unstructured Grids. Int. J. Numer. Meth. Fluids **46**, 37–57 (2004) 101

Wang, D., Fan, J., Siao, C., Berno, A., Young, P., Sapolsky, R., Ghandour, G., Perkins, N., Winchester, E., Spencer, J., et al.: Large-scale identification, mapping, and genotyping of single-nucleotide polymorphisms in the human genome. Science **280**(5366), 1077 (1998) 24

Wang, H., Iovenitti, P., Harvey, E., Masood, S.: Numerical investigation of mixing in microchannels with patterned grooves. J. Micromech. Microeng. **13**, 801 (2003) 34

Whitesides, G.: The origins and the future of microfluidics. Nature **442**(7101), 368–373 (2006) 2

Whitesides, G., Stroock, A.: Flexible methods for microfluidics. Physics Today **54**, 42 (2001) 46, 47

Wild, D.: The immunoassay handbook. Elsevier Science Ltd (2005) 58

Woolley, A., Mathies, R.: Ultra-high-speed DNA fragment separations using microfabricated capillary array electrophoresis chips. PNAS **91**(24), 11,348 (1994) 17

Wu, D., Qin, J., Lin, B.: Electrophoretic separations on microfluidic chips. J. Chromatogr. A **1184**(1-2), 542 – 559 (2008) 15

Wu, X., Newman, S., Pawliszyn, J.: Miniaturization of capillary isoelectric focusing. Electrophoresis **22**(18), 3968–3971 (2001) 18

Wu, Z., Li, D.: Micromixing using induced-charge electrokinetic flow. Electrochimica Acta **53**(19), 5827–5835 (2008) 35

Xu, N., Lin, Y., Hofstadler, S., Matson, D., Call, C., Smith, R.: A microfabricated dialysis device for sample cleanup in electrospray ionization mass spectrometry. Anal. Chem. **70**(17), 3553–3556 (1998) 9

Xu, Y., Zhang, C.X., Janasek, D., Manz, A.: Sub-second isoelectric focusing in free flow using a microfluidic device. Lab Chip **3**, 224 – 227 (2005) 20, 106

Xuan, X., Li, D.: Analysis of electrokinetic flow in microfluidic networks. J. Micromech. Microeng. **14**, 290 (2004) 31

Yager, P., Edwards, T., Fu, E., Helton, K., Nelson, K., Tam, M., Weigl, B.: Microfluidic diagnostic technologies for global public health. Nature **442**(7101), 412–418 (2006) xxx

Yalow, R., Berson, S.: Immunoassay of endogenous plasma insulin in man. J. Clin. Invest. **39**(7), 1157 (1960) 23

Yang, R., Fu, L., Lin, Y.: Electroosmotic flow in microchannels. Journal of colloid and interface science **239**(1), 98–105 (2001) 50

Yang, R., Tseng, T., Chang, C.: End effects on electro-osmotic flows in microchannels. J. Micromech. Microeng. **15**, 254 (2005) 33, 50, 95

Young, M., Kwon, O.: A Parallel Unstructured Dynamic Mesh Adaption Algorithm for 3-D Unsteady Flows. International Journal for Numerical Methods in Fluids **48**, 671–690 (2005) 101

Yu, J., Chou, Y., Yang, R.: High-resolution modeling of isotachophoresis and zone electrophoresis. Electrophoresis **29**(5), 1048–1057 (2008) 28

Zhang, Y., Wong, T., Yang, C., Ooi, K.: Dynamic aspects of electroosmotic flow. Microfluid. Nanofluid. **2**(3), 205–214 (2006) 35

Zhu, J., Xuan, X.: Particle electrophoresis and dielectrophoresis in curved microchannels. J. Colloid Interf. Sci. **340**(2), 285–290 (2009) 33

Zienkiewicz, O., Morgan, K.: Finite elements and approximation. Wiley New York (1983) 62